UNIVERSIDADE FEDERAL DO PARANÁ

MÉROLYN CAMILA NAVES DE LIMA RODRIGUES

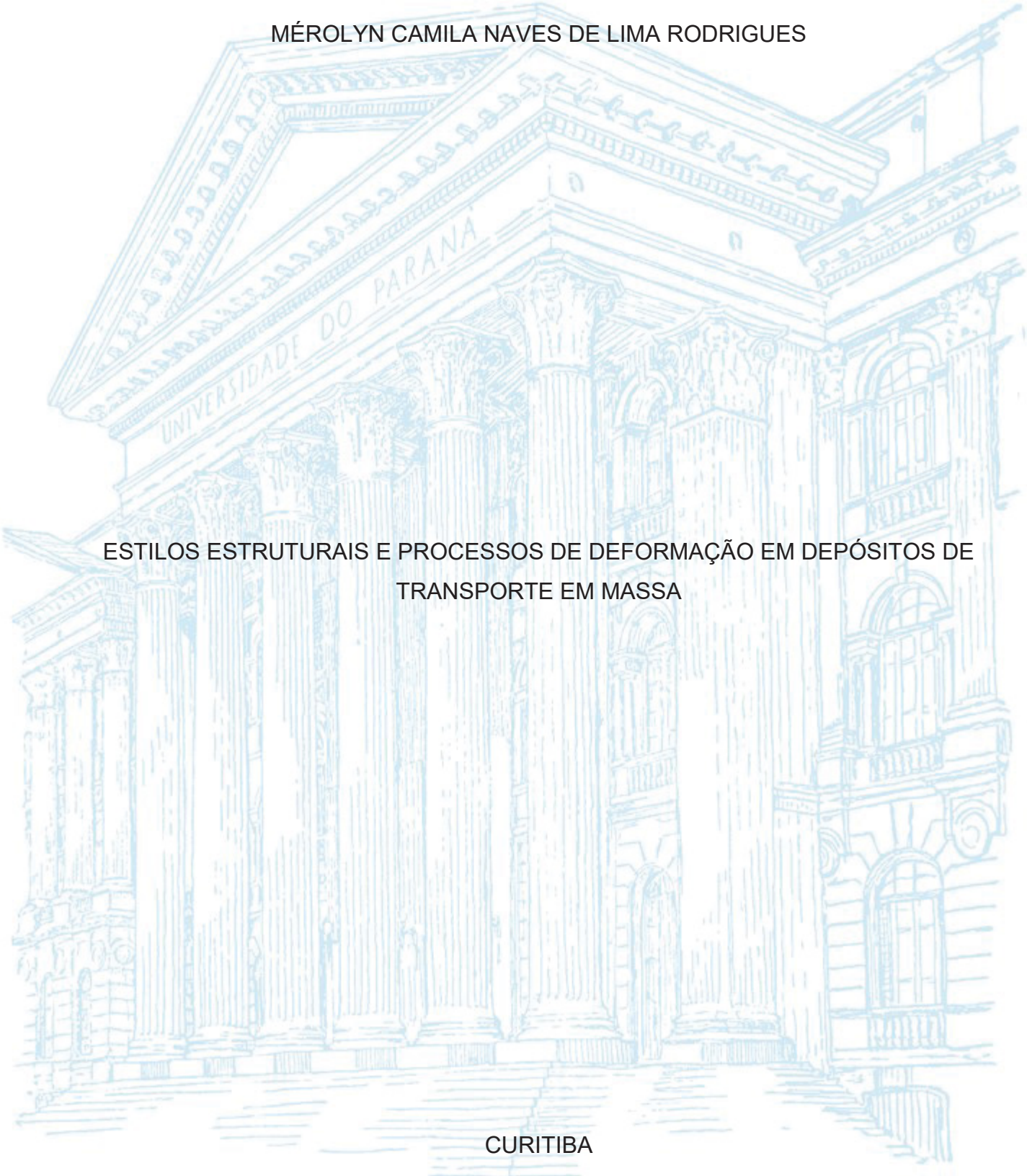

ESTILOS ESTRUTURAIS E PROCESSOS DE DEFORMAÇÃO EM DEPÓSITOS DE TRANSPORTE EM MASSA

CURITIBA

2019

MÉROLYN CAMILA NAVES DE LIMA RODRIGUES

ESTILOS ESTRUTURAIS E PROCESSOS DE DEFORMAÇÃO EM DEPÓSITOS DE TRANSPORTE EM MASSA

Tese apresentada como requisito parcial à obtenção do grau de Doutor, pelo Programa de Pós-Graduação em Geologia, na área de concentração Geologia Exploratória, Departamento de Geologia, Setor de Ciências da Terra, Universidade Federal do Paraná.

Orientadora: Profa. Dra. Barbara Trzaskos

Coorientador: Prof. Dr. Fernando Farias Vesely

CURITIBA

2019

Catalogação na Fonte: Sistema de Bibliotecas, UFPR
Biblioteca de Ciência e Tecnologia

R696e

Rodrigues, Mérolyn Camila Naves de Lima
Estilos estruturais e processos de deformação em depósitos de transporte em massa [recurso eletrônico] / Mérolyn Camila Naves de Lima Rodrigues. – Curitiba, 2019.

Tese - Universidade Federal do Paraná, Setor de Ciências da Terra, Programa de Pós-Graduação em Geologia, 2019.

Orientador: Barbara Trzaskos – Coorientador: Fernando Farias Vesely.

1. Geologia submarina. 2. Paraná, Rio, Bacia. 3. Bacias (Geologia). 4. Grupo Itararé. I. Universidade Federal do Paraná. II. Trzaskos, Barbara. III. Vesely, Fernando Farias. IV .Título.

CDD: 551.460808162

Bibliotecário: Elias Barbosa da Silva CRB-9/1894

MINISTÉRIO DA EDUCAÇÃO
SETOR SETOR DE CIENCIAS DA TERRA
UNIVERSIDADE FEDERAL DO PARANÁ
PRÓ-REITORIA DE PESQUISA E PÓS-GRADUAÇÃO
PROGRAMA DE PÓS-GRADUAÇÃO GEOLOGIA - 40001016028P5

TERMO DE APROVAÇÃO

Os membros da Banca Examinadora designada pelo Colegiado do Programa de Pós-Graduação em GEOLOGIA da Universidade Federal do Paraná foram convocados para realizar a arguição da tese de Doutorado de **MEROLYN CAMILA NAVES DE LIMA RODRIGUES** intitulada: **ESTILOS ESTRUTURAIS E PROCESSOS DE DEFORMAÇÃO EM DEPÓSITOS DE TRANSPORTE EM MASSA**, após terem inquirido a aluna e realizado a avaliação do trabalho, são de parecer pela sua APROVAÇÃO no rito de defesa.

A outorga do título de doutor está sujeita à homologação pelo colegiado, ao atendimento de todas as indicações e correções solicitadas pela banca e ao pleno atendimento das demandas regimentais do Programa de Pós-Graduação.

CURITIBA, 29 de Março de 2019.

BARBARA TRZASKOS
Presidente da Banca Examinadora

SIMONE CERQUEIRA PEREIRA CRUZ
Avaliador Externo (UFBA)

CLAUS FALLGATTER
Avaliador Externo (UFPE)

CARLOS MAURICIO MONNERAT DE OLIVEIRA
Avaliador Externo (PETROBRAS)

EDUARDO SALAMUNI
Avaliador Interno (UFPR)

AGRADECIMENTOS

À Professora Dra. Barbara Trzaskos pela orientação, contribuições, discussões esclarecedoras, confiança e demais auxílios intelectuais e financeiros.

Ao Professor Dr. Fernando Farias Vesely pelo auxílio na orientação, contribuições e discussões esclarecedoras.

Ao Professor Dr. G. Ian Alsop pelo auxílio na orientação, contribuições, discussões esclarecedoras e pela disposição em me receber na University of Aberdeen, Reino Unido.

Aos relatores da qualificação Dr. Carlos Mauricio Monnerat de Oliveira (Petrobras) e Professor Dr. Eduardo Salamuni (UFPR) pelas correções e sugestões que enriqueceram o manuscrito.

Aos membros da banca examinadora Dr. Simone Cerqueira Pereira Cruz Dr. Carlos Mauricio Monnerat de Oliveira (Petrobras), Professor Dr. Eduardo Salamuni (UFPR) e Dr. Claus Fallgatter (UFPE) pelas correções e sugestões que enriqueceram o manuscrito.

À CAPES pela concessão de bolsa de doutorado.

À UFPR pela disponibilização de seus laboratórios e infraestrutura.

Ao curso de pós-graduação em Geologia da UFPR pelo suporte acadêmico.

Ao LABAP (Laboratório de Análise de Bacias) pela infraestrutura para a realização dos trabalhos de campo e escritório.

A todos meus companheiros de LABAP, pós-graduação, amigos da graduação e não geólogos que de alguma forma me ajudaram. Em especial aqueles que me auxiliaram em campo e em discussões da pesquisa: Thammy Ellin Mottin, Danielle Cristine Buzatto Schemiko Pereira, Leonardo Mairink Barão, Renato Leandro, Maysa Folmann, Joana Caroline de Freitas Rosin.

A minha família pelo apoio, compreensão e ajuda. Em especial a minha mãe, minha irmã Mélani e ao meu namorado Alfeu.

Externo aqui meus agradecimentos àqueles que contribuíram de uma forma ou de outra durante a elaboração da tese, se esqueço de alguém nos agradecimentos é porque a memória me trai, mas em meu coração sou grato a todos.

RESUMO

Depósitos de transporte em massa (*mass-transport deposits* - MTDs) correspondem a fluxos gravitacionais caracterizados por complexo registro estrutural e compõem parcela importante do registro geológico marinho profundo moderno e antigo. O entendimento destes depósitos é importante para uma melhor compreensão das características paleogeográficas de uma bacia. O Grupo Itararé, unidade permocarbonífera da Bacia do Paraná, possui significante recorrência desses depósitos em seu registro estratigráfico. Os MTDs do Grupo Itararé consistem principalmente de lamitos arenosos/cascalhosos (diamictitos) e grandes blocos de arenitos e ritmitos ressedimentados. Esses depósitos apresentam grande variedade de estruturas deformacionais. Para o estudo foram selecionados MTDs em todos os três intervalos de tempo principais do Grupo Itararé, que correspondem mais ou menos com as formações Lagoa Azul, Campo Mourão e Taciba. Os MTDs estudados mostram estruturas distensionais, compressionais, outras estruturas indicativas de cisalhamento, clastos intrabacinais e matriz (resultante da mistura de sedimentos remobilizados). A partir da relação entre a quantidade de matrix (gerada por deformação) e assembleia de estruturas identificadas em cada MTD foram caracterizadas três fácies deformacionais (DF-1, DF2 e DF-3) que representam diferentes graus de desagregação e mistura dos sedimentos. As fácies deformacionais podem ser correlacionadas, de modo geral, a movimentos em massa, como deslizamento (*slide*), escorregamento (*slump*) e fluxo de detritos (*debris flow*). As relações deformacionais observadas em cada fácies deformacional sugerem que os processos deformacionais durante o fluxo em massa auxiliam a desagregação e mistura que leva à homogenização dos sedimentos remobilizados. Falhamentos, boudinagem e outros processos de cisalhamento são importantes processos de desagregação das camadas, blocos e sedimentos em todas as fácies deformacionais. Enquanto que cisalhamento na escala de laminações, cisalhamento nas bordas dos blocos e fluidização dos sedimentos auxiliam no processo de mistura. Diversos estudos consideram que as estruturas geradas por fluxos em massa permitem definir a orientação do talude. Neste estudo verificou-se a aplicabilidade da análise de diferentes estruturas na definição de paleotaludes a partir de dados de MTDs com exposição limitada. Para a definição de paleotaludes foram selecionadas estruturas como dobras, clastos orientados, estrias e sulcos em bordas de blocos, falhas, injetito e boudins. A maioria das estruturas mostraram potencial para uso na definição de paleotaludes. O estudo verificou ainda uma boa correlação entre paleotaludes indicados por MTDs próximos e em mesmo nível estratigráfico. A comparação entre os resultados de paleotaludes com dados estratigráficos, como paleocorrentes e mapa de isópacas, indicam implicações para a paleogeografia da bacia em cada intervalo de tempo do Grupo Itararé. Além disso, corroboram e complementam alguns aspectos sobre a evolução da deposição do Grupo Itararé, propostas na literatura.

Palavras-chaves: fluxos gravitacionais em massa; deformação penecontemporânea; Grupo Itararé

ABSTRACT

Mass-transport deposits are the result of gravity-induced mass flows, characterized by complex structural record and compose an important portion of ancient and modern deep marine geological record. The comprehension of these deposits is important for the comprehension of paleogeographic characteristics of a basin. The Itararé Group, permocarboniferous unit of Paraná Basin, have significant reccurrence of MTDs in its stratigraphic record. MTDs of Itararé Group consist of diamictites and large blocks of sandstone and rhythmite. These deposits also show wide variety of deformational structures, however, there are a lack of studies of structural characterization and analysis of kinematic indicators. For the present study, MTDs were selected in all main three intervals of Itararé Group, which correspond more or less to Lagoa Azul, Campo Mourão and Taciba formation. The studied MTDs show strucures associated to extension, compression and shearing, and other deformational products as sedimentary clasts and matrix. From the relationship between amount of matrix and structural assemblage identified in each MTD were describe three deformational facies (DF-1, DF-2 e DF-3) that display different degrees of disaggregation and mixing of sediments. These facies can be corrolated more or less to some mass movements, as slides, slumps and debris flows. The deformational relationships identified in each DF suggest that deformation processes during mass flows help the disaggregation and mixing that leads to the homogenization of remobilized sediments. Faulting, boudinage and other shearing processes are important processes of layer, sedimentary blocks and sediments disaggregation in all deformational facies. While lamination-scale shearing, shearing at margens of sedimentary blocks and sediments fluidization help the process of mixing. Several studies consider that structures generated by mass flows allow the paleoslope definition. In this study, we verified the applicability of the analysis of different structures in the definition of the orientation of paleoslope from data collected in MTDs with limited exposure. For the definition of paleoslope were selected data from structures as folds, faults, boudins, injectites, oriented clasts, bedding, banded matrix and grooves/stretch marks at margens of sedimentary blocks. Most structures display potential use for paleoslope definition. We verified agreement between paleoflows of MTDs in same regions and time interval. The comparinson between MTDs paleoflows and stratigraphic data, such as paleocurrents of associated deposits and isopach map, indicates implication for the paleogeography of the basin in each time interval of Itararé Group. Besides, they corroborate and complement some aspects about the depositional evolution of Itararé Group proposed in the literature.

Keywords: gravity-induced mass flows; penecontemporaneous deformation; Itararé Group

LISTA DE FIGURAS

LISTA DE TABELAS

LISTA DE SIGLAS E ABREVIAÇÕES

AIM – Axial plane intersection method

c.i. – confidence interval

c.v. – classification value

CPRM – Serviço Geológico do Brasil

DAM – Downslope average method

DF-1 – Deformational facies 1

DF-2 – Deformational facies 2

DF-3 – Deformational facies 3

F.C. – Final classification

FFD – Fold facing direction

FIM – Fault intersection method

IC – Large intrabasinal clast

LNS – Layer normal shear

LPS – Layer parallel shear

MAD – Mean axial-planar dip method

MAD-AP – Mean axial-planar dip method for axial plane

MAM – Mean axis method

MAPS – Mean axial plane strike method

MBSM – Mean bedding strike method

MFOM – Mean fault orientation method

MTC – Mass transport complex

MTD – Mass transport deposit

N – Number of measurements

N.M. – Number of methods

P.o. – Preferential orientation

OL – Outcrop locality

OC – Outcrop locality classification

SAM – Separation arc method

S.D. – Structure Dataset classification

SLM – Slickenline method

T1 – Time interval 1

T2 – Time interval 2

T3 – Time interval 3

SUMÁRIO

1. INTRODUÇÃO À TESE

1.1. INTRODUÇÃO AO TEMA

Movimentos em massa, ou fluxos gravitacionais em massa, representam os principais riscos geológicos subaéreos e subaquosos e podem formar feições de escala quilométrica. Processos de transporte em massa podem ter consequências catastróficas tais como *tsunamis*, avalanches, queda de blocos e deslizamentos (e.g. Martinsen 1994). Compreendem ainda importantes elementos deposicionais em ambientes marinhos (Posamentier & Martinsen 2011).

Depósitos de transporte em massa (MTDs, do termo em inglês *mass-transport deposits*) são formados por fluxos gravitacionais coesivos gerados a partir de processos de ressedimentação (e.g. Martinsen 1994). Tais depósitos compõem parcela importante do registro geológico marinho profundo antigo e moderno (e.g. Posamentier & Walker 2006). Conforme Posamentier & Walker (2006), em alguns ambientes de águas profundas recentes esses depósitos podem constituir mais de 50% da seção estratigráfica, enquanto em alguns registros antigos os processos de transporte em massa deformaram mais de 75% da sucessão estratigráfica (Martinsen 1989, 1994). Portanto, os fluxos gravitacionais que geram esses depósitos são importantes na evolução das margens continentais mundiais modificando e definindo a morfologia submarina ao longo de linhas de costas e taludes e em bacias de águas profundas do mundo (e.g. De Blasio & Elverhøi 2010).

Os depósitos de transporte em massa têm importância em diversos aspectos da vida humana e na geologia de margens continentais (Martinsen 1994, Posamentier & Walker 2006). A crescente atenção aos MTDs deve-se, em grande parte, à exploração de petróleo em ambiente de águas profundas, uma vez que esses depósitos podem condicionar as acumulações de hidrocarbonetos (e.g. Posamentier & Martinsen 2011). Com o intuito de entender o processo de movimento em massa e seus depósitos, muitos estudos têm focado diferentes questões, como a estratigrafia (e.g. Eyles & Eyles 2000, Martinsen et al. 2003), a análise estrutural (e.g Alsop & Marco 2011, 2013, 2017, Ogata et al. 2014, Sobiesiak et al. 2016), a análise de paleotalude (e.g. Woodcock 1979, Strachan & Alsop 2006, Sharman et al 2015), as características morfológicas e geométricas (e.g. De Blasio & Elverhøi 2010) e a relação deposicional com turbiditos (e.g. Nelson et al. 2011, Kneller et al. 2016).

Depósitos de transporte em massa, associados com depósitos de ambiente marinho como turbiditos, têm sido há muito documentados no registro estratigráfico do Grupo Itararé, unidade permo-carbonífera da Bacia do Paraná, assim como a presença de estruturas deformacionais associadas a formação desses depósitos (e.g. Salamuni et al. 1966, Gama Jr. et al. 1992, Eyles et al. 1993, Vesely et al. 2005, Vesely & Assine 2006, Suss et al. 2014). Trabalhos recentes a respeito dos MTDs no Grupo Itararé têm enfatizado os aspectos deposicionais, como fácies e geometria (e.g. Gama Jr. et al. 1992, Suss et al. 2014, Mottin et al. 2018, Schemiko 2018), porém poucos trabalhos buscaram caracterizar as estruturas deformacionais presentes (e.g. Vesely et al. 2005, Carneiro & Costa 2006). Em geral, esses depósitos carecem de registro detalhado e sistemático da geometria de suas estruturas, seus processos de deformação com relação ao processo de fluxo gravitacional e análise de paleotalude, com aplicação dos métodos descritos na literatura. O estudo de MTDs tem ainda papel importante na compreensão do cenário deposicional do Permo-Carbonífero da Bacia do Paraná.

Neste estudo, é trabalhada a hipótese de que a compreensão das estruturas deformacionais observada em MTDs pode auxiliar na definição de paleotaludes, inclusive os MTDs com características de fluxo de detritos, os quais são pouco abordados nos estudos de paleotalude. Outra hipótese abordada considera que a compreensão dos processos de formação das estruturas de MTDs pode auxiliar a determinar como se iniciam e evoluem os fluxos gravitacionais em massa, incluindo sua tendência à homogeneização.

1.2. ORGANIZAÇÃO DA TESE

A tese está organizada em 5 tópicos principais que discorrem acerca da deformação em depósitos de transporte em massa. O primeiro tópico consiste da introdução à tese, em que são apresentados os objetivos, os métodos e a localização da área estudada. O segundo tópico trata de fundamentos teóricos relevantes à esta pesquisa acerca das características gerais depósitos de transporte em massa e métodos para definição de paleotaludes, presentes na literatura.

No terceiro tópico são apresentados e discutidos os resultados acerca das estruturas deformacionais identificadas nos MTDs do Grupo Itararé por meio do artigo intitulado "*Making a homogenite: An outcrop perspective into the evolution of*

deformation within mass-transport deposits", submetido a revista *Marine and Petroleum Geology*. Este artigo discute ainda sobre o papel das estruturas deformacionais na evolução da deformação e no processo de homogeneização em MTDs.

O quarto tópico apresenta e discute os dados estruturais coletados e o uso destes na definição de paleotaludes, bem como indica possíveis implicações para a paleogeografia da Bacia do Paraná durante a deposição do Grupo Itararé, principalmente para a região entre Mafra (SC) e Alfredo Wagner (SC). A avaliação dos conjuntos de dados e resultados da análise das estruturas para definição de paleotaludes foi realizada com base em parâmetros e respectivos valores de classificação apresentados nas tabelas dos Apêndices 1 e 2. Direções de transporte obtidos por cada método aplicado e direção final de transporte para cada localidade estudada são apresentados no Apêndice 3 Este tópico consiste em um artigo intitulado: "*Relationships between mass-transport kinematics and sediment dispersal patterns in paleogeographic reconstruction*", a ser submetido ao *Journal of Structural Geology*. O quinto tópico corresponde as considerações finais da tese, baseadas na integração dos dois artigos gerados. Por fim, o sexto e último tópico apresentas as referências utilizadas na parte teórica deste trabalho.

1.3. OBJETIVOS

O escopo deste estudo é compreender os estilos estruturais e os processos de deformação, mistura e homogeneização associados a fluxos gravitacionais de massa. Além disso, pretende-se avaliar a validade dessas estruturas como indicadores do azimute de mergulho de paleotaludes, auxiliando assim, na interpretação da evolução deposicional da unidade permocarbonífera da Bacia do Paraná.

Para tanto, os objetivos específicos são:

- documentar e classificar as estruturas deformacionais quanto ao estilo estrutural;
- determinar a cinemática, os mecanismos de deformação envolvidos;
- definir os tipos de estruturas e os métodos para definição dos paleotaludes;
- analisar os dados estruturais para definir possíveis paleotaludes.

1.4. ÁREA DE ESTUDO E CONTEXTO GEOLÓGICO

O estudo foi desenvolvido em rochas permocarboníferas da Bacia do Paraná (Grupo Itararé) expostas na borda leste (Fig. 1.1), entre os municípios de Ibaiti (Estado do Paraná) e Alfredo Wagner (Estado de Santa Catarina; Fig. 1.2). Nesta região foram selecionados 18 afloramentos, que incluem pedreiras e cortes de estrada, onde depósitos de transporte em massa foram identificados.

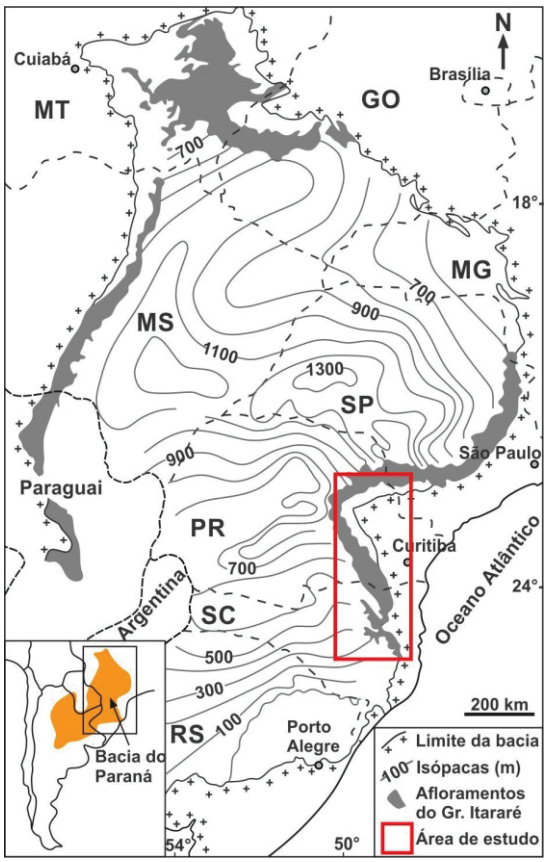

Fig. 1.1: Mapa de isópacas do Grupo Itararé (modificado de França & Potter 1988) com indicação da área de estudos.

A Bacia do Paraná consiste em uma depressão alongada na direção NNE-SSW com cerca de 1.600.000 km² e que abrange partes do Brasil, Argentina, Paraguai e Uruguai. O contorno atual da bacia corresponde a limites erosivos relacionados em parte a tectônica meso-cenozoica do continente (Milani et al. 2007).

Conforme Zalán et al. (1990), trata-se de uma bacia flexural, de interior cratônico e natureza policíclica, desenvolvida no interior do paleocontinente Gondwana pelo resfriamento litosférico de região anormalmente aquecida durante o Ciclo Brasiliano. A hipótese de rifte precursor como mecanismo responsável pela primeira fase de subsidência é a mais aceita por diversos autores (e.g. Zalán et al. 1987, Milani 1997), seguido por longa história de sag. A evolução estratigráfica-

estrutural da bacia foi em grande parte controlada por *trends* NW-SE, NE-SW e subordinadamente E-W, herdados do embasamento heterogêneo, constituído por núcleos cratônicos e faixas móveis aglutinados durante o Ciclo Orogênico Brasiliano (Zalán et al. 1990).

O preenchimento da bacia consiste de rochas sedimentares de origem terrígena, subordinadamente ocorrem níveis isolados de calcários e evaporitos e rochas vulcânicas. Na calha central a bacia chega a apresentar 7.000 m de espessura (Milani et al. 2007). As principais unidades da bacia foram classificadas como sequências deposicionais por Milani (1997), que subdivide a bacia em seis sequências de 2ª ordem ou supersequências limitadas por discordâncias regionais. Essas sequências retratam grandes estágios na evolução tectono-sedimentar da bacia, transcorridos durante intervalos de tempo. São elas: Rio Ivaí (Neo-ordoviciano – Eossiluriano; Grupo Rio Ivaí); Paraná (Neossiluriano – Neodevoniano; Grupo Paraná); Gondwana I (Neocarbonífero – Eotriássico; Formação Aquidauana, grupos Itararé, Guatá e Passa Dois); Gondwana II (Meso-Neotriássico; Formação Santa Maria); Gondwana III (Neojurássico – Eocretáceo Grupo São Bento); Bauru (Eo-Neocretáceo; depósitos continentais suprabasálticos Bauru e Caiuá). A deposição das sequências ocorreu em diferentes ambientes tectônicos, que resultou em diversos episódios de subsidência intercalados com períodos de soerguimento e erosão parcial (Zalán et al. 1990, Soares 1991, Milani 1997, 2004).

O Grupo Itararé consiste em complexa unidade estratigráfica que abrange registro de glaciações do Neopaleozóico. Esse grupo situa-se na base da sequência Gondwana I (Neocarbonífero – Eotriássico) que engloba sucessivamente os grupos Guatá e Passa Dois. Essa sequência consiste em ciclo transgressivo-regressivo de segunda ordem (Vail et al. 1977) e representa a sucessão sedimentar mais espessa da Bacia do Paraná (e.g. Vesely & Assine 2006, Milani et al. 2007). Dados bioestratigráficos indicam deposição do Grupo Itararé entre o Neocarbonífero e o Eopermiano (Daemon & Quadros 1970, Souza et al. 2003).

França & Potter (1988) dividiram o Grupo Itararé, com base em dados de poços, em três ciclos estratigráficos, classificados litoestratigraficamente como formações Lagoa Azul, Campo Mourão e Taciba. Tais formações não mostram distinção litológica, porém mostram sucessões de fácies de afinamento para o topo compostas por espessa unidade basal rica em areia seguida por seção caracterizada por sedimentos finos com diamictitos, arenitos, ritmitos e folhelhos.

A espessura do Grupo Itararé é extremamente variável, podendo ser inferior a 100 m no estado do Rio Grande do Sul até 1.300m no estado de São Paulo, que corresponde a porção centro-norte da bacia (Fig. 1.1.) (Vesely & Assine 2006). As estruturas antigas do embasamento são indicadas como prováveis condicionantes à sedimentação do Grupo Itararé (e.g. Ferreira 1982, França & Potter 1988, Zalán et al. 1990, Eyles et al. 1993). Outras evidências de atividade tectônica distensiva durante a deposição do Grupo Itararé são indicadas pela presença de falhas normais, bruscas variações laterais de fácies e depósitos de escorregamentos de massa (Zalán et al. 1990, Eyles et al. 1993).

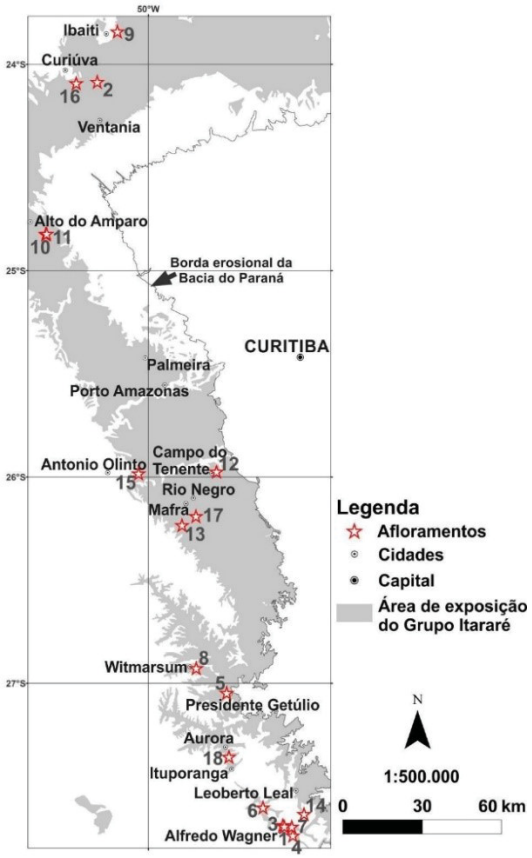

Fig. 1.2: Mapa de localização dos afloramentos em estudo (identificados pelos números de 1 a 18), com indicação da área de exposição do Grupo Itararé na borda leste da bacia entre os estados do Paraná e Santa Catarina (Fonte: CPRM 2004).

Por muitos anos, pesquisadores interpretaram grande parte dos depósitos do Grupo Itararé como resultantes de deposição em ambientes glacio-continentais, incluindo varvitos, tilitos e feições oriundas de deformação glaciotectônica (e.g. Leinz 1937, Almeida 1948, Canuto 1985). Segundo Leinz (1937) os depósitos glaciais permocarboníferos são de caráter continental com pequena parte ligada ao ambiente marinho, distinguida por “pseudo-tilitos”.

Pesquisas posteriores passaram a indicar influência marinha, ao menos na parte superior do Grupo Itararé (e.g. Sanford & Lange 1960, Schneider et al. 1974, França & Potter 1988). Na região de Rio Negro (PR) e Mafra (SC), Salamuni et al. (1966) identificaram pela primeira vez depósitos gerados por correntes de turbidez no Grupo Itararé. Trabalhos paleontológicos também indicam que a sedimentação do Grupo Itararé ocorreu principalmente em ambientes glacio-marinhos (e.g. Maack 1946, Rocha-Campos 1967, França et al. 1996, Quadros 2002).

A sedimentação controlada por fluxos gravitacionais subaquosos é reconhecida em toda sucessão do Grupo Itararé (e.g. Salamuni et al. 1966, Castro 1991, Gama Jr. et al. 1992, Eyles et al. 1993, França et al. 1996, Vesely & Assine 2004, 2006, Arab et al. 2009, d'Avila 2009, Puigdomenech et al., 2014, Suss et al. 2014, Aquino et al. 2016, Carvalho & Vesely 2016, Fallgatter & Paim, 2017, Valdez et al. 2017, Mottin et al. 2018, Vesely et al. 2018). A identificação desses depósitos traz importantes mudanças na interpretação dos ambientes deposicionais. Os depósitos de fluxos gravitacionais do Grupo Itararé compreendem basicamente depósitos turbidíticos espessos e delgados e depósitos de transporte em massa, os quais sugerem deposição em águas relativamente profundas (e.g. d'Avila 2009). Os depósitos de transporte em massa do Grupo Itararé são formados basicamente por lamitos arenosos/cascalhosos (diamictitos), arenitos, ritmitos e lamitos ressedimentados, com grande variedade de estruturas deformacionais.

Umas das características de depósitos de transportes em massa é a presença de estruturas deformacionais penecontemporâneas. No Grupo Itararé, diversas pesquisas identificaram estruturas deformacionais penecontemporâneas. Parte foi interpretada como de origem glaciotectônica, principalmente por autores que reconhecem deposição essencialmente glacio-continental em determinados intervalos da unidade (e.g. Martin 1961, Caetano-Chang 1984, Vesely et al. 2015, Aquino et al. 2016, Rosa et al. 2019). Porém, outras pesquisas indicam que apenas parte da deformação penecontemporânea registrada no Grupo Itararé seria resultante de glaciotectônica, outra parte seriam resultante de fluxos gravitacionais (e.g. Rocha Campos 1967, Carneiro & Costa 2003, Canuto 1985).

Vesely et al. (2005) descrevem deformações penecontemporâneas ligadas a escorregamentos, tais como falhas normais, basculamento de camadas, superfícies de deslizamento intraestratais, sobrecarga, diapirismo, dobras e falhas de empurrão. Esses autores discutem que a interpretação da origem glaciotectônica para as feições

de caráter compressivo não seria possível nesses locais, pela inexistência de tilitos autênticos (depósitos glaciogênicos) e superfícies de abrasão glacial associadas às estruturas. Ademais, faltam exposições contínuas que facilitariam o estabelecimento de relações espaciais entre os vários tipos. Os trabalhos mais recentes a respeito de depósitos de transporte em massa do Grupo Itararé mostram a geometria e o modelo deposicional, as relações de contato e potencialidade econômicas desses depósitos (e.g. Suss et al. 2014, Carvalho & Vesely 2017, Valdez et al. 2017, Mottin et al. 2018, Schemiko 2018).

1.5. MÉTODOS

1.5.1. Levantamento bibliográfico

Para o desenvolvimento da pesquisa foram consultados trabalhos sobre diversos assuntos relacionados aos objetivos. A análise bibliográfica contemplou os seguintes temas: 1) Bacia do Paraná; 2) Grupo Itararé; 3) análise estrutural; 4) depósitos de transporte em massa; 5) definição de paleotaludes.

1.5.2. Trabalho de campo

Foram descritos afloramentos de depósitos de transporte em massa, nos quais foi realizada a coleta sistemática de dados estruturais, tais como dobras (eixo, flancos, espessura de flancos e charneira, vergência), falhas (atitude de planos e lineações), *boudins* (eixos e falhas, este último em *boudins* assimétricos) e outros possíveis indicadores cinemáticos, conforme indicação da literatura (e.g. Strachan & Alsop 2006, Alsop & Marco 2012). Também foi realizada a coleta de dados de paleocorrentes de depósitos associados, quando possível. O trabalho de campo incluiu a coleta sistemática de amostras, orientadas sempre que possível, dos diferentes litotipos que compõem os MTDs e suas estruturas deformacionais para análise estrutural.

1.5.3. Definição dos paleotaludes

Para a definição dos paleotaludes foram analisadas diferentes estruturas a partir de métodos indicados na literatura (mais informações em na seção 2.2. Análise estrutural e definição de paleotaludes e na seção 4.4. Methods). Além disso, foram consideradas diferentes feições de cisalhamento que podem indicar a cinemática dos

fluxos gravitacionais, tais como estruturas do tipo par S-C, arrasto em bordas de blocos, estruturas tipo sigma. O trabalho também incluiu a coleta de indicadores direcionais (paleocorrentes) nos estratos associados, quando presentes, com o intuito de auxiliar nas inferências quanto aos paleotaludes deposicionais. Foram utilizados dados de paleocorrentes de depósitos associados, como depósitos flúvio-deltáicos e turbidíticos, próximos dos afloramentos estudados e em níveis estratigráficos similares publicados na literatura ou de estudos de colaboradores, não publicados.

2. FUNDAMENTAÇÃO TEÓRICA

2.1. DEPÓSITOS DE TRANSPORTE EM MASSA

Movimentos em massa são importantes processos geológicos que podem ocorrer em ambiente subaéreo e subaquoso e podem mobilizar pequenas a grandes quantidades de sedimentos e rocha (Martinsen 1994). Para que ocorra movimento em massa é necessário um talude ou gradiente, que pode variar em inclinação de menos de 0,1°, como a frente de deltas modernos (Prior & Colemam 1978), a vertical e superfícies projetadas, onde é suscetível ocorrer queda de blocos.

A classificação de movimentos em massa pode ser realizada com base em diferentes fatores, como processo e reologia, produto, tipo de material mobilizado, entre outros (e.g. Dott 1963, Nardin et al. 1979). Contudo, a classificação mais usada na literatura é baseada na reologia dos movimentos em massa, que foi simplificada por Nemec (1990). Essa classificação divide os movimentos de massa, tanto em ambiente aéreo como subaquoso, em seis categorias: rastejo, deslizamento, escorregamento, fluxo com comportamento plástico ou com comportamento fluido (como fluxo de detritos e correntes de turbidez, respectivamente), e queda de blocos ou detritos (Fig. 2.1).

Peterson (1965) utilizou pela primeira vez o termo Depósito de Transporte em Massa em estudo sobre lamitos seixosos aflorantes na California, os quais foram interpretados como depósitos de fluxo de detritos. Outros termos têm sido empregados na literatura para esses depósitos como, por exemplo, complexos de transporte em massa, complexos de movimento em massa, depósitos gravitacionais em massa, entre outros (Posamentier & Martinsen 2011).

Muitos depósitos de transporte em massa mostram evidências de atuação de diferentes processos, uma vez que pode ocorrer transição contínua entre eles (Fig.

2.1). A principal forma de distinguir os depósitos gerados, por cada tipo de processo, considera a deformação e integridade do acamamento (e.g. Martinsen 1994). Deslizamentos mostram acamamento com pouca ou nenhuma deformação. Escorregamentos mostram acamamento com arquitetura controlada pela deformação, enquanto que no fluxo de detritos o acamamento se perde devido à tendência de mistura do material e a deformação. Os depósitos de fluxos de detritos são, comumente, caracterizados por textura de clastos suportados por matriz (Posamentier & Martinsen 2011), porém, pode ser difícil classificar um depósito conforme o processo de fluxo gravitacional quando parcialmente exposto em campo (Posamentier & Martinsen 2011).

Fig. 2.1: Esquema de classificação de movimentos em massa baseado em reologia (Modificado de Nemec 1990).

Em geral os depósitos de transporte em massa são subdivididos em região distensional, na parte proximal, e região compressional, na parte distal do depósito (e.g. Farrell 1984, Farrell & Eaton 1987, Elliot & Williams 1988, Martinsen 1989, 1994, Martinsen & Bakken 1990, Smith 2000, Debacker et al. 2001, Strachan 2002, 2008, Alsop & Marco 2014, Alsop et al. 2016). As margens laterais são interpretadas como zonas de deformação transcorrente, que tendem a ser paralelas a direção de movimento do fluxo gravitacional (e.g. Farrell 1984, Martinsen 1994, Debacker et al. 2009). A evolução temporal dos MTDs compreende, em geral, cincos estágios:

iniciação, translação, cessação, relaxamento e compactação (Farrell 1984, Strachan 2002, 2008, Alsop & Marco 2011).

Depósitos gerados por correntes de turbidez não são considerados depósitos de transporte em massa, uma vez que o mecanismo principal de suporte dos grãos é um fluxo não-turbulento. Contudo, muitos pesquisadores (e.g. Nemec 1990, Strachan 2008, Posamentier & Martinsen 2011) indicam que o mesmo evento pode gerar os dois tipos de depósitos, sendo ambos parte do processo deposicional contínuo.

Os depósitos de transporte em massa mostram ainda características extremamente variáveis, em relação a geometria, morfologia, tamanhos, composições, estruturas e fácies (e.g. Posamentier & Kolla, 2003, De Blasio & Elverhøi 2010). O complexo registro estrutural dos MTDs resulta da relação complexa entre as instabilidades associadas com o gradiente de taludes, topografia, acamamento sedimentar, mudanças na reologia e padrões de fluxo durante o movimento gravitacional (Jones 1939, Hansen 1971, Woodcock 1979, Farrell 1984, Martinsen 1989, Strachan & Alsop 2006). As instabilidades, capazes de desencadear processos de transporte em massa, podem ser geradas por diversos fatores sedimentares (como incremento do ângulo do talude devido a rápida sedimentação associada com quebra de gradiente de deltas) e tectônicos (como eventos sísmicos) (e.g. Martinsen 1994).

2.2. ANÁLISE ESTRUTURAL E DEFINIÇÃO DE PALEOTALUDE

A hipótese principal da análise de paleotaludes é a relação previsível entre a atitude do talude e a orientação das estruturas de MTDs (Hahn 1913, Jones 1939, Lewis 1971, Woodcock 1979, Farrell 1984, Smith 2000, Strachan & Alsop 2006). Diversos estudos consideram que a análise estrutural cuidadosa e sistemática de todas as estruturas direcionais e a aplicação de diversos métodos de análise permitem não apenas definir o paleotalude e paleogeografia associada, mas também a compreensão dos processos e mecanismos deformacionais (e.g. Strachan & Alsop 2006, Debacker et al. 2009, Alsop & Marco 2011, Posamentier & Martinsen 2011).

Falhas e dobras são as principais estruturas identificadas em MTDs e são consideradas por muitos como as principais estruturas que refletem a orientação do paleotalude (e.g. Woodcock 1976, 1979, Farrell 1984, Maltman 1994a, b, Strachan &

Alsop 2006). No entanto, grande variedade de estruturas tem sido descrita em MTDs, tais como boudins, blocos orientados e feições de cisalhamento.

2.2.1. Dobras

As dobras são uma das principais estruturas descritas em MTDs e a caracterização de sua geometria é importante para a aplicação de métodos de definição de paleotaludes (e.g. Woodcock 1979; Farrell 1984; Strachan & Alsop, 2006, Alsop & Marco 2011, Alsop et al. 2016, 2017). De modo simplificado, as charneiras das dobras são orientadas paralelamente a direção do talude, com plano axial mergulhando em direção ao talude e a vergência da dobra para a bacia (e.g. Woodcock 1979). Com o aumento da deformação, durante a translação, os eixos das dobras podem rotacionar em direção ao talude abaixo e gerar dobras em bainhas (e.g. Farrell & Eaton 1987, 1988, Alsop & Holdsworth 2002, Alsop & Marco 2013) ou, variações na deformação, podem gerar grande variedade de dobras (Alsop & Marco 2013).

Alsop & Marco (2011) indicam que a análise das dobras tem sido realizada com base em conceitos que relacionam a dobra com a direção de cisalhamento, que corresponde em termos gerais, ao modelo de *flow perturbation* aplicado à deformação em rochas metamórficas (e.g. Holdsworth 1990, Alsop & Holdsworth 2004a, 2004b). Variações no movimento ao longo do plano de descolamento resultam em arqueamento na direção ao fluxo das dobras durante a translação em fluxos gravitacionais em massa (e.g. Farrell 1984, Alsop & Holdsworth 2002, 2007, Strachan & Alsop 2006). Variações na velocidade de fluxo, em direção ao mergulho do talude, resultam em *layer-parallel shear* (LPS), que geram dobras com alto ângulo com o transporte (Fig. 2.2A). Este tipo de dobra mostra padrão de vergência unimodal em direção ao mergulho do talude e plano axial com mergulho em direção ao talude (Woodcock 1979). Os planos axiais rotacionam progressivamente durante o transporte talude abaixo, resultando em distribuição estatística em leque perpendicular ao transporte (Alsop & Marco 2011) (Tabela 2.1). Variações de velocidade ao longo da direção do talude resultam em *layer-nomal shear* (LNS, Fig. 2.2B), que formam dobras inicialmente oblíquas ou subparalelas ao transporte (Alsop & Holdsworth 2002, 2007, Strachan & Alsop 2006, Debacker et al. 2009). A rotação durante o cisalhamento progressivo pode gerar dobras em bainha que complicam os

padrões de vergência, dificultando a diferenciação desses tipos de dobras (e.g. Strachan & Alsop 2006, Alsop et al. 2007, Alsop & Carreras 2007).

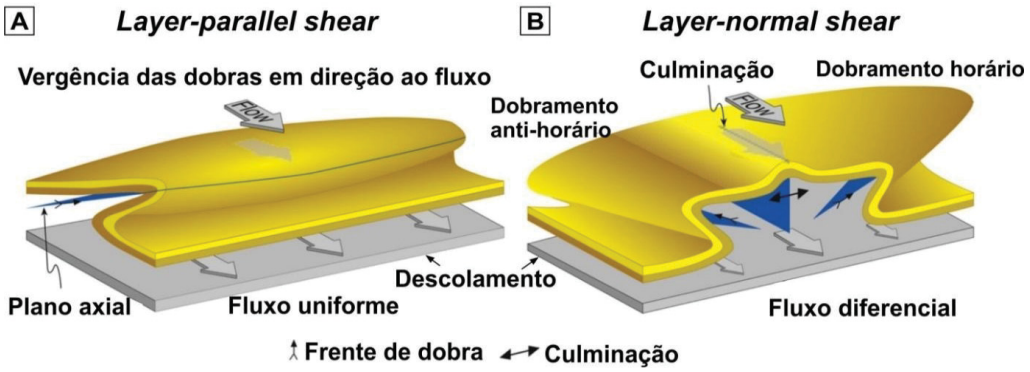

Fig. 2.2: A) Deformação por *layer-parallel shear*. B) Deformação por *layer-normal shear*. Notar vergência e orientação de planos axiais e eixos das dobras (Modificado de Alsop & Marco 2011).

Tabela 2.1: Critérios de diferenciação entre dobras geradas por layer-parallel shear (LPS) e dobras geradas por layer-normal shear (LNS) (Alsop & Marco 2011).

	Layer Parallel Shear (LPS)	**Layer Normal Shear (LNS)**
Orientação do eixo	Transporte normal (direção paralela ao talude)	Transporte sub-paralelo (paralelo mergulho do talude)
Vergência do eixo	Padrão de vergência unimodal (paralelo a direção de mergulho do talude)	Padrão de vergência bimodal (paralelo a direção do talude)
Direção do plano axial	Varia perpendicularmente ao transporte (intersecções paralelas a direção do talude). Mergulho do plano axial com distribuição unimodal, com poucos mergulhando talude abaixo.	Varia em relação a direção de transporte (intersecções paralelas ao mergulho do talude). Mergulho do plano axial com distribuição bimodal, com plano axias mergulhando igualmente para cada lado.
Direção de mergulho do plano axial	Distribuição em leque do mergulho perpendicular ao transporte com intersecções paralelas a direção do talude.	Distribuição em leque do mergulho em relação a direção de transporte, com intersecções paralela ao mergulho do talude.
Direção de frente de dobra	Padrão unimodal de direção de frente em direção ao transporte (*upwards*). Direção de frente paralela ao mergulho do talude.	Padrão bimodal de direção de frente (*upwards*) perpendicular ao trnasporte. Direção de frente paralela a direção de talude.

Os métodos baseados em orientação de dobras são os mais utilizados na literatura. Para a definição de paleotaludes, a partir de dobras, foram considerados dados de eixos, planos axiais, *facing* e a vergência. Os métodos aplicados para eixos de dobras incluem:

- Método de eixo médio (*Mean Axis Method* – MAM, Fig. 2.3A): proposto por Jones (1939, cf. Hahn 1913), baseia-se na ideia de que os eixos das dobras em MTDs são, estatisticamente, paralelos a direção do paleotalude e perpendicular a direção de transporte. Este método fornece duas possíveis direções opostas (direções a 180°) de transporte para o MTD. O sentido de transporte, paralelo a direção de mergulho do paleotalude, é usualmente definido com base na vergência das dobras (que tende a ser na direção talude abaixo), direção de *fold facing* (e.g. Jones 1939, Woodcock 1976), e/ou em dados paleogeográficos regionais. Este método foi revisto por Woodcock (1979), Strachan & Alsop (2006), Alsop & Holdsworth (2007) e Debacker et al. (2009). Conforme observações desses autores, o método é mais apropriado para dados de dobras geradas por *layer-parallel shear* (LPS) e que passaram por pouca ou nenhuma rotação posterior, sendo consideradas dobras cilíndricas ou com eixo levemente curvilíneo. Para dobras geradas por *layer-normal shear* (LNS), que mostram eixos orientados paralelamente ou oblíquas a direção de transporte, não é possível aplicar este método, pois a direção pode ser 90° diferente da direção verdadeira (Woodcock 1979). Para estas dobras deve ser aplicado o método de arco de separação (*Separation Arc Method* - SAM, Hansen 1965; não aplicado no presente estudo) e/ou o método de eixo médio paralelo ao mergulho do talude (*Downslope Average Axis Method* - DAM, Woodcock 1979, detalhado a seguir).
- Método de eixo médio paralelo ao mergulho do talude (*Downslope Average Axis Method* – DAM, Fig. 2.3B): é aplicado as dobras formadas por *layer-normal shear* ou formadas por *layer-parallel shear* que passaram por deformação e rotação do eixo (dobras não cilíndricas ou dobras-em-bainha), ou seja, que tem orientação média dos eixos paralela a obliqua à direção de transporte do MTD (Woodcock 1979).
- Método de mergulho médio de plano axial – para eixos (*Mean Axial-planar Dip Method* - MAD): sugerido por Alsop & Marcos (2012, baseado em método usado por Strachan 2002), utiliza os eixos das dobras juntamente com o ângulo de mergulho de planos axiais associados. O cisalhamento e rotação de dobras, inicialmente com plano axial vertical, durante a deformação progressiva, resulta em distribuição estatística em leque dos planos axiais com relação a direção do paleotalude e com mergulho principal em direção oposta ao mergulho do paleotalude (e.g. Woodcock 1979), que é consistente com *layer-parallel shear* (Alsop & Holdsworth 2004a, Strachan & Alsop 2006, Alsop & Carreras 2007, Lesemann et al. 2010).

Considerando isso, os planos axiais com ângulos de mergulho maiores podem representar dobras que passaram por pouca rotação durante o cisalhamento horizontal e, assim, os eixos associados a esses planos axiais tem orientação mais próxima da orientação original. Para restringir o uso de eixos de dobras, que passaram por pouca rotação durante a deformação progressiva, os autores indicam o uso de eixo associados aos planos axiais com ângulo tipicamente maior que 45° com relação a camadas não-deformadas. Para sistemas dominados por LPS os eixos associados a esses planos axiais devem mostrar orientação normal à direção de transporte. Para sistemas dominados por LNS, associado com cisalhamento diferencial, os eixos associados a esses planos axiais se desenvolvem subparalelo à direção de transporte e associados à diminuição do ângulo entre flancos (e.g. Alsop & Holdsworth 2007, Debacker et al. 2009). Sendo assim, é necessário diferenciar se a formação das dobras foi dominada por LPS ou LNS.

- Método arco de separação (*Separation Arc Method* – SAM; Fig. 2.3A e B): sugerido por Hansen (1971), este método é baseado na observação de que as dobras podem mostrar grande variação de orientação de eixos com relação à direção do paleotalude. Neste método considera-se que a direção de fluxo corresponde ao bisector do ângulo agudo entre os grupos de dobras que mostram assimetria ou vergência oposta. Um problema deste método é que o mesmo depende da orientação do membro final das dobras para definir o arco de separação, que por sua vez dependerá da amostragem (Woodcock 1979). Este método não pode ser aplicado em algumas situações, como: (1) sobreposição dos dados de dobras com vergência oposta, não permitindo assim a definição do arco de separação; ou (2) identificação de apenas um sentido se vergência das dobras ou assimetria grosseira aparente das dobras que não permite definição do arco de separação (Alsop and Marco 2012).

Os métodos para análise de dobras a partir de dados dos planos axiais incluem:

- Método de direção média de plano axial (*Mean Axial Plane Strike Method* – MAPS, Fig. 2.3C): considera a direção média dos planos axiais para determinar a direção de transporte. Para sistemas dominados por LNS considera-se que os planos axiais serão normais a direção do paleotalude e paralelos a direção de mergulho do paleotalude, enquanto que em sistemas dominados por LPS a direção dos planos axiais será paralela a direção do paleotalude e normal a direção de mergulho do mesmo. Segundo Alsop & Marco (2012) a deformação progressiva altera pouco a direção dos planos axiais tanto em contexto de LPS quanto LNS, sendo que a rotação

afetará mais o mergulho dos planos axiais. Assim como MAM, este método fornece duas direções opostas para o transporte e o sentido pode ser definido pela vergência das dobras associadas a direção de mergulho dos planos axiais, que tende a ser oposta a direção de transporte dos MTDs, ou pelo contexto paleogeográfico (e.g. Alsop & Marcos 2012, Alsop et al. 2016).

- Método de intersecção de planos axiais (*Axial Planar Method* - AIM, Fig. 2.3C): método desenvolvido inicialmente por Alsop & Holdsworth (2002, 2004a, b) para dobras em zonas de cisalhamento de nível crustal médio do tipo *flow perturbation folds* e, posteriormente aplicada por Strachan & Alsop (2006) e Debacker et al. (2009) para MTDs. Este método utiliza a orientação estatística de planos axiais de dobras para definir a direção e sentido de transporte do MTD. Em sistemas dominados por LNS os planos axiais tendem a ser subparalelos a direção de transporte, com distribuição estatística em leque e direção de intersecção dos planos axiais paralelos a direção de transporte do MTD. Em sistemas dominados por LPS os planos axiais tendem a mostrar altos ângulos com relação à direção de transporte e distribuição estatística em leque, com a maioria dos dados mergulhando em direção ao talude acima e poucos mergulhando na direção do transporte, resultantes de rotação. Neste caso, a direção de intersecção dos planos axiais será paralela a direção do paleotalude e normal a direção de transporte do MTD. Para este método os planos axiais podem ser analisados identificando planos axiais associados a dobras S e Z, sendo que a direção de transporte corresponde a direção média de intersecção entre planos axiais de dobras S e planos axiais de dobras Z.

- Método de mergulho médio de planos axiais – para planos axiais (*Mean Axial-Planar Dip Method to Axial Planes* - MAD-AP): método baseado no método MAD proposto por Alsop & Marco (2012). Este método se diferencia do MAD, por utilizar dados de direção de mergulho do plano axial, no lugar de dados de eixos, juntamente com o ângulo de mergulho do plano axial. A deformação progressiva altera pouco a direção dos planos axiais tanto em contexto de LPS quanto LNS modificando mais o ângulo de mergulho dos planos axiais, e por vezes a direção de mergulho (Alsop & Marco 2012). Ao restringir a análise aos planos axiais com ângulo de mergulho maior que 45° (com relação às camadas não deformadas) a direção média de mergulho será mais próxima a orientação original. Considerando que para dobras de sistemas dominadas por LPS o mergulho principal dos planos axiais mostra direção oposta ao mergulho do paleotalude (e.g. Woodcock 1979). O método permite obter não apenas

a direção (que será paralela a direção de mergulho médio dos planos axiais), mas também o sentido de transporte (que será oposto à direção média do paleotalude obtido pelo método). Já para dobras de sistemas dominados por LNS a direção de mergulho tende a ser obliqua (com mergulhos para dois lados opostos) a normal, com direção média de mergulho tendendo a ser normal a direção de transporte. Portanto, para essas dobras o método permite apenas definir a direção de transporte do MTD, que será normal a direção média de mergulho e paralela a direção média dos planos axiais.

Outro método aplicado a dados de dobras é o de direção de frente de dobra (*Fold Facing Directions* - FFD) proposto por Holdsworth (1988) para estudo de dobras sedimentares e tectônicas, e aplicada por Alsop & Marco (2011, 2012, entre outros) a dobras de MTDs. A frente de dobra é definida como a direção em que rochas mais novas são encontradas, e que é normal ao eixo e ao longo do plano axial. A direção de frente é um dado linear que fornece a notação direcional (norte, sul, entre outras), assim como a vergência, porém fornece também componente ascendente ou descendente para a dobra. Dados de direção de frente são, portanto, representados como pontos em estereograma. As linhas de frentes descendentes (*downward-facing lines*) são plotadas diretamente como pontos, pois intersectam o hemisfério inferior do estereograma, enquanto as linhas de frente ascendentes (*upward-facing lines*) intersectam o hemisfério superior e são projetadas verticalmente e plotadas no hemisfério inferior. Como as dobras de MTDs mostram tipicamente direção de frente ascendente com sentido segundo a direção de transporte, a identificação da direção de frente de dobra pode auxiliar na compreensão da deformação, uma vez que dobras com frente descendentes são atípicas podem representar áreas de redobramento (Woodcock 1976).

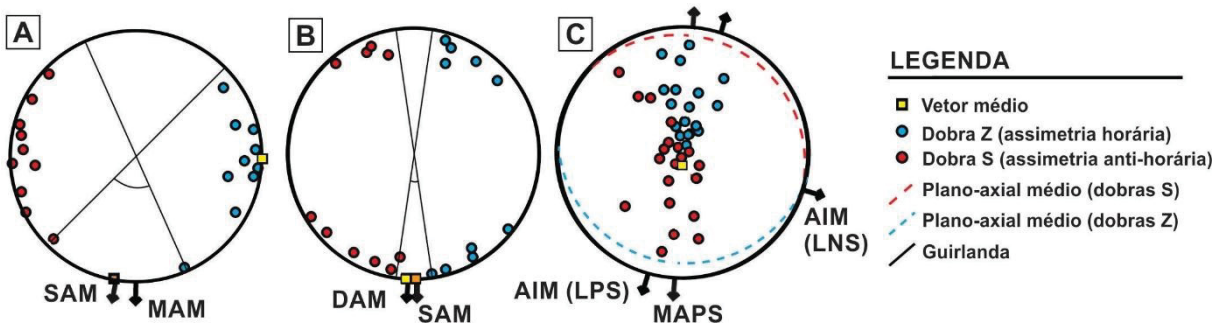

Fig. 2.3: Ilustração representando métodos de definição de paleotalude com base em dados de dobras. A) e B) Eixos de dobras, respectivo vetor médio e setas que indicam

a direções transporte para MTD obtidos de métodos, como MAM e DAM. C) Polos de planos axiais de dobras, respectivo vetor médio e setas que indicam a direções transporte para MTD obtidos de métodos como AIM, APM e MAPS (modificado de Sharman et al. 2015).

2.2.2. Falhas

Planos de falha constituem outro importante tipo de estrutura observados em MTDs, cujo uso na definição de paleotaludes tem sido crescente. O principal método para utilizado para a análise de falhas é o método de orientação média (*Mean Fault Orientation Method* - MFOM). Este método presume que a direção de transporte do MTD é subparalela a direção média de mergulho da falha, com sentido *updip* para falhas inversas *downdip* para falhas normais. O método considera que não há significante componente oblíquo ou transcorrente nas falhas (Farrell 1984, Martinsen & Bakken 1990, Debacker et al. 2009, Sharman et al. 2015). Isso porque o grau de obliquidade ou transcorrência do movimento das falhas é difícil de determinar, uma vez que indicadores cinemáticos, como estrias, não são comumente observados em falhas de MTDs. Contudo, a possibilidade de ocorrer falhas com direção subparela a paralela a direção de fluxo não deve ser ignorada. Alsop & Marco (2011) identificaram falhas normais com direção subparalela a direção do fluxo. Portanto, é necessário verificar a orientação das falhas em relação a outras estruturas e indicadores de fluxos, sempre que viável.

As falhas podem ainda ser analisadas através do método de intersecção de falha (*Fault Intersection Method* - FIM). Este método, proposto por Debacker et al. (2009), considera que a intersecção de falhas de MTDs mostra, idealmente, orientação perpendicular a direção de transporte. No entanto, quando somente falhas inversas ou normais são identificadas, ou ainda quando não se tem certeza se as falhas normais e inversas foram formadas no MTD ao longo de talude similar deve-se analisar a intersecção dos dois tipos de falhas separadamente.

Apesar de estrias não serem comuns ou serem de difícil identificação em falhas de MTDs, por vezes é possível identificá-las ao longo de falhas que apresentam material argiloso. A identificação de *steps* ao longo das falhas também costuma ser difícil, porém devem ser procurados, pois permitem a identificação da cinemática da falha. Ainda que seja possível identificar apenas estrias, é proposto neste estudo o

uso de estrias como indicadores de direção de fluxo, e que direção média das estrias é paralela a direção de transporte do MTD.

2.2.3. Acamamento

Conforme Jones (1939), é esperado em MTDs que o acamamento mostre orientação preferencial com relação ao paleotalude, semelhante as dobras. Considerando isso, Sharman et al. (2015) propuseram o método de direção média de acamamento (*Mean Bedding Strike Method* - MBSM). Este método considera que orientações individuais do acamamento variem consideravelmente, a direção de transporte dos MTDs pode ser relacionada a direção média do acamamento. Para a aplicação do método é necessário medir aleatoriamente um número suficiente de acamamento dentro do MTD. A direção média do acamamento será subparalela a paralela à direção do paleotalude e oblíqua a normal à direção de transporte do MTD. Contudo, este método deve ser menos preciso em MTD com acamamento levemente inclinado e/ou dobras curvilíneas, e aplicado com atenção em áreas com significante deformação tectônica.

O deslizamento ao longo de planos de estratificação ou acamamento, principalmente, de camadas ou laminações argilosas geram superfícies de descolamento/cisalhamento em MTDs e podem formar estrias intraestratais ao longo desses planos. Considerando isso, é proposto neste estudo que a direção média de estrias intraestratais seja paralela à direção de transporte do MTD, e, portanto, pode ser utilizado como indicador de transporte. Contudo, deve-se ter atenção para possíveis mudanças locais na orientação das estrias devido à presença, por exemplo, de blocos em contato com a camada.

O conceito do método de direção média de acamamento (*Mean Bedding Strike Method* - MBSM) também foi aplicado a bandamento composicional/granulométrico presente na matriz de alguns MTDs descritos como diamictitos, que também podem mostrar orientação preferencial.

2.2.4. Boudins

A orientação de *boudins*, simétricos e/ou assimétricos, também pode ser utilizada para definir a orientação do paleotalude. Para isso é necessário identificar se a boudinagem está associada apenas à distensão paralela à direção de transporte de MTD, que geraria *boudins* simétricos ou assimétricos (Fig. 2.4A e B), ou associada

também à distensão secundária perpendicular à direção de transporte, que formaria *boudins* simétricos transversais ao sentido de fluxo (Fig. 2.4C) (modelo proposto por Festa et al. 2013). Essa distinção é possível analisando os *boudins* em mais de uma direção e orientação com relação a outros indicadores cinemáticos.

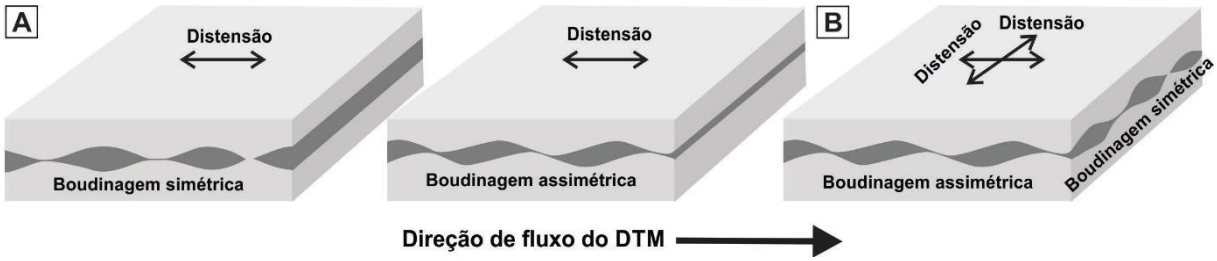

Fig. 2.4: Distensão paralela ao transporte do MTD com formação de boudins simétricos ou assimétricos. B) Distensão paralela e perpendicular ao transporte do MTD com formação de boudins assimétricos e assimétricos, respectivamente (baseado em Festa et al. 2016).

Identificada a orientação geral dos *boudins* dentro do MTD é possível definir a direção de transporte do MTD através de dados de eixos, seja de *boudins* simétricos ou assimétricos, e dados de falhas e cinemática de *boudins* assimétricos. Para eixos de *boudins* simétricos ou assimétricos associados à direção principal de distensão dentro de MTDs pode-se utilizar o método de eixo médio (*Mean Axis Method* – MAM, Jones 1939). O método considera a direção dos eixos paralela à direção do paleotalude e normal à direção de mergulho do paleotalude (Fig. 2.4A e B). Para eixos de *boudins* simétricos associados à distensão secundária dentro de MTDs e normal à direção de transporte (Fig. 2.4C) sugere-se a aplicação de método similar ao método de eixo médio paralelo ao mergulho do talude (*Downslope Average Axis Method* – DAM, Woodcock 1979). Por este método, a orientação média dos eixos é paralela à direção de transporte e mergulho do paleotalude.

Boudins assimétricos resultam de distensão e cisalhamento e são associados, geralmente, à distensão principal dentro dos MTDs, paralela à direção de transporte e cisalhamento (Festa et al. 2013; Fig. 2.4B). Portanto, a cinemática de *boudins* assimétricos pode ser utilizada para definir a cinemática do fluxo gravitacional que gerou o MTD (e.g. Ogata et al. 2014, Festa et al. 2013). Além disso, espera-se que as falhas de *boudins* assimétricos tenham orientação preferencial que possam ser relacionadas à direção de transporte do MTD. Considerando isso, as falhas de *boudins* assimétricos (tipo dominó ou *shearband*) podem ser analisadas através do

método similar ao de orientação média de falhas (*Mean Fault Orientation Method* – MFOM, e.g. Debacker et al. 2009). Este método presume que a direção de transporte do MTD é subparalela à direção média de mergulho da falha, com sentido oposto para falhas de *boudins* dominó (falhas antitéticas ao cisalhamento) e com mesmo sentido para falhas de *shearband* boudins (falhas sintéticas ao cisalhamento). Para falhas de *boudins* espera-se que não haja significante componente obliquo ou transcorrente. Outro método que pode ser aplicado as falhas de *boudins* analisa a intersecção de falhas (*Fault Intersection Method* - FIM, Debacker et al. 2009) considerada perpendicular a direção de transporte.

2.2.5. Outras estruturas e indicadores cinemáticos

Métodos que utilizam dados de blocos e clastos também foram selecionados. Segundo Bull et al. (2009), objetos com eixo mais longo (X) que outro (Y) transportados por longas distâncias tem seu eixo maior orientado paralelamente a direção de transporte do MTD. Com base nisso, Sobiesiak et al. (2016) sugerem que a orientação do eixo maior de blocos pode ser usada como indicador de direção de transporte (Fig. 2.5). No presente estudo este método foi aplicado a blocos e clastos alongados. Os blocos podem mostrar ainda sulcos e estrias causadas por atrito em suas bordas e a orientação dessas estruturas também é usada como indicador de direção de transporte (conforme Ogata et al. 2014).

Outras feições indicativas de cisalhamento, tais como estruturas tipo “par S/C”, arrasto na borda de blocos, entre outros, também são utilizadas para definir o sentido de transporte do MTD quando presentes.

Para MTDs que apresentam injetitos de areia, com orientação preferencial, foi analisada a relação a fim de verificar se os injetitos foram formados no mesmo processo que gerou o MTD. Em casos de relação direta entre MTDs e injeções de areia a orientação média dos mesmos foi comparada a direção das demais estruturas do depósito, determinando assim a relação espacial. Conforme a relação espacial foi definida se a direção média de injeção tende a ser paralela ou normal a direção de fluxo. O vetor de direção de fluxo obtido com os dados de injetitos foi somado aos demais vetores obtidos através de outras estruturas para definir o paleofluxo do MTD.

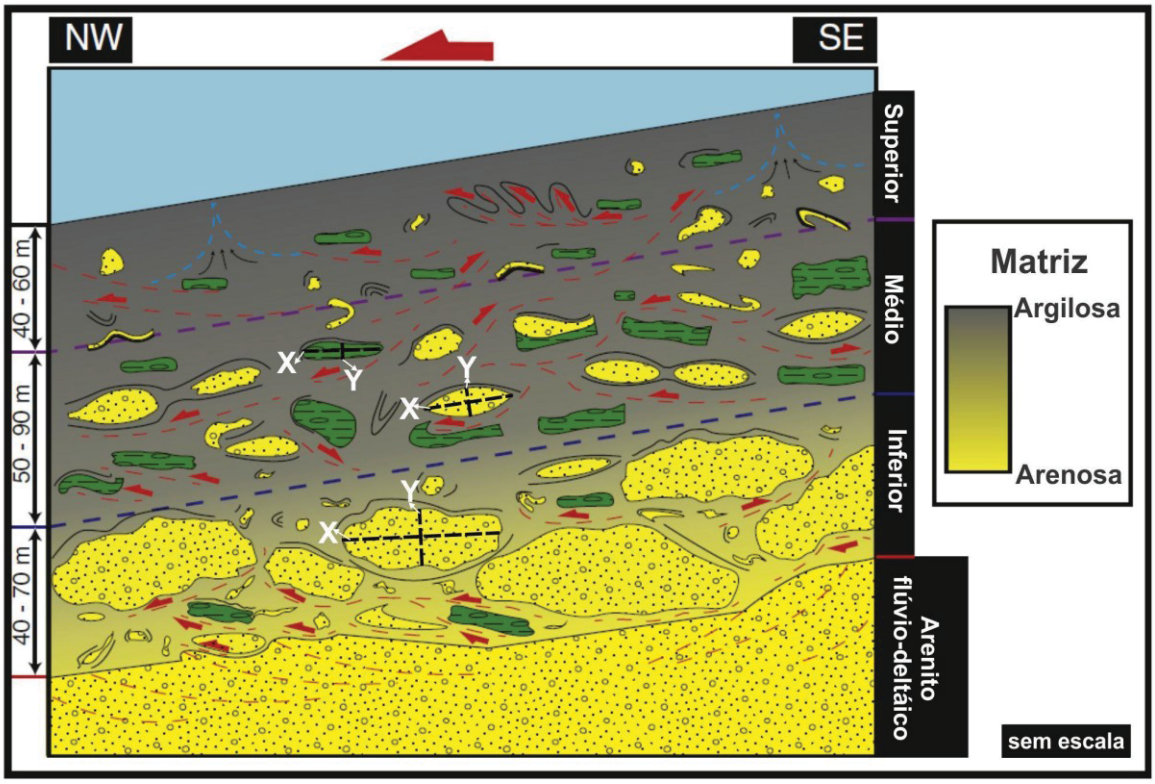

Fig. 2.5: Desenho esquemático da orientação de blocos em MTD exposto na região do Cerro Bola, Bacia de Paganzo, NW da Argentina (modificado de Sobiesiak et al 2016). Notar identificação de eixo maior (X) e menor (Y) dos blocos.

2.2.6. Definição da direção média de transporte

Para definir o paleotalude para cada MTD em estudo foram, primeiramente, identificadas as estruturas que permitem a definição da direção e sentido de transporte através de estereogramas, além de indicadores cinemáticos para definir o sentido de transporte. A partir das características de cada estrutura foram selecionados os métodos apropriados para definição de paleotalude. Foi também verificada a ocorrência de modificações por deformações tardias que podem dificultar a análise. Cada método aplicado permitiu obter um vetor, com ou sem indicação de sentido dependendo do método. A partir dos vetores obtidos para cada afloramento foi definido o vetor médio que corresponde a direção de transporte (Fig. 2.6). Enquanto que o sentido de transporte foi definido com base nos indicadores cinemáticos do MTD juntamente com indicadores paleogeográficos regionais. A direção de mergulho do paleotalude será paralela a direção do fluxo gravitacional que gerou o MTD.

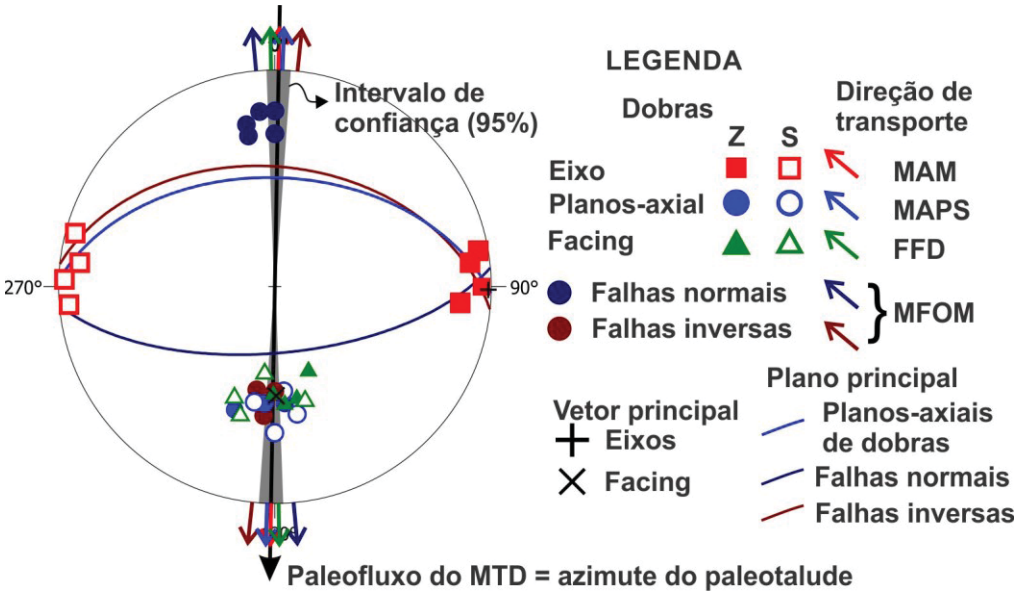

Fig. 2.6: Ilustração hipotética que exemplifica a definição da direção final de transporte de MTD a partir de diferentes métodos aplicados a dados de falhas (normais e inversas) e dobras de um mesmo MTD. A direção final de transporte combinada com a cinemática indicada pelas estruturas permite definir o sentido de fluxo do MTD e, portanto o azimute do paleotalude. O intervalo de confiança (95%) é fornecido por softwares de análise estrutural (mais informação ver seção 4.4. Methods).

3. RESULTADOS – PARTE I: MAKING A HOMOGENITE: AN OUTCROP PERSPECTIVE INTO THE EVOLUTION OF DEFORMATION WITHIN MASS-TRANSPORT DEPOSITS

Mérolyn Camila Naves de Lima Rodrigues[a,*], Barbara Trzaskos[a], G. Ian Alsop[b], Fernando Farias Vesely[a],

[a] Programa de Pós-Graduação em Geologia, Departamento de Geologia, Universidade Federal do Paraná, Caixa Postal 19001, CEP 81531-980 Curitiba, PR, Brazil

[b] Dept. of Geology and Petroleum Geology, University of Aberdeen, Aberdeen, AB24 3UE, Scotland, UK

3.1. ABSTRACT

Mass-transport deposits (MTDs) may show a variety of deformation aspects, from poorly-deformed layers to highly deformed and homogenized deposits, as a result of the different kinds of mass-transport processes involved in their evolution. Previous studies indicate that the downslope flow transformation of MTDs is characterized by increasing disaggregation, mixing and homogenization of a non- to poorly lithified protolith, which may ultimately generate a homogenite. We here explore the role of deformation processes in the disaggregation and mixing of sediments that tend to lead to sediment homogenization and so may also control the evolution of MTDs. Using the Itararé Group of the Paraná Basin, southern Brazil as our case study, we examine several types of structures in MTDs with varying degrees of mass disaggregation and discuss the role of deformation process in the progressive homogenization of the sediment. Three deformational facies (DF-1, DF-2 and DF-3) were identified and interpreted as recording varying stages of homogenization of sediments (disaggregation and mixing) within the incipient, mature and evolved, flows respectively. These different stages show transitional aspects that indicate a gradual homogenization. The comparison between structural assemblages and the amount of matrix in the three different deformational facies indicates a close relationship between styles of deformation and the homogenization expected for mass flows. The processes that promoted disaggregation include boudinage, faulting, layer-parallel shearing and

marginal deformation of intrabasinal clasts, while mixing processes that generate matrix include shearing and liquefaction/ fluidization of sediments.
Keywords: submarine mass-flows; syn-sedimentary deformation; sedimentary matrix; Itararé Group; Paraná Basin

3.2. INTRODUCTION

Submarine landslides are important processes of redistribution of sediment to deep-water environments (Martinsen, 1994; Posamentier and Martinsen, 2011; Moscardelli et al., 2006). The resulting deposits, termed mass-transport deposits (MTDs), are generated by flows exhibiting variable rheology, including creeps, slides, slumps, and debris flows (Dott, 1963; Jenner et al., 2007; Nardin, 1979; Nemec, 1990), which are characterized by different deformational aspects (e.g., Martinsen, 1994; Posamentier and Martinsen, 2011). These mass-transport processes form a continuum in which one type of flow may evolve into another (Dasgupta, 2003; Dott, 1963; Nemec, 1990) through downslope flow transformation (Strachan, 2008). This continuum tends to be characterized by increasing disaggregation, mixing and homogenization of a non- to poorly lithified protolith (e.g. Nemec, 1990; Martinsen, 1994; Eyles and Eyles, 2000; Mutti et al., 2006).

Many studies focussing on different aspects of MTDs have been presented recently, including stratigraphy (e.g. Eyles and Eyles, 2000; Martinsen et al., 2003; Berton and Vesely, 2016), kinematics and definition of paleoslopes (e.g. Sharman et al., 2015; Alsop et al., 2016; ; Alsop et al., 2017; and references therein), structural analysis (e.g. Alsop and Marco, 2011, 2013; Jablonská et al. 2016, 2018; Ogata et al., 2014c; Sobiesiak et al., 2016), morphological and geometric aspects (e.g. Alves and Cartwright, 2010; Alves, 2015; Bryn et al., 2005; De Blasio and Elverhøi, 2011), relationship with turbidites (e.g., Alves and Cartwright, 2010; Armitage et al., 2009; Fallgatter et al., 2017; Kneller et al., 2016; Nelson et al., 2011), and flow behaviour (e.g. López-Gamundí, 1993; Strachan, 2008; Fallgatter et al., 2017). On the other hand, the deformation processes through which undeformed layers evolve into highly deformed and homogenized deposits are relatively poorly understood and require further investigation, as suggested by Strachan (2008).

Homogenite is the final product of deformation and homogenization of sediments remobilized by a mass flow event. The homogenite is composed of matrix

and, when present, extrabasinal rigid clasts. The matrix is the result of complete disaggregation of loose to poorly-consolidated sediments (Ogata et al., 2012a; Pini et al., 2012) and its composition is dependent on the protolith, and also additional material incorporated from erosion and entrainment of the substrate (e.g., Ogata et al., 2012a, 2014c; Sobiesiak et al., 2018). Talling et al. (2012) discuss a deposit-based classification for submarine sediment density flows in terms of sediment support mechanisms, flow state and flow rheology. However, two issues that remain poorly explored are: i) the use of deformation structures in mass flow events as indicators of flow rheology, and; ii) the influence of deformation processes on the disaggregation and mixing of the sediments, which leads to a final homogenization.

The aim of this study is to examine structural styles in MTDs with varying degrees of mass disaggregation, and also to discuss the role of deformation process in the progressive homogenization of the MTD protolith. The study was performed in exposed Carboniferous to Early Permian strata of the Itararé Group (Paraná Basin, southern Brazil; Fig. 3.1), in which MTDs have been reported by previous workers (e.g. Gama Jr. et al., 1992; Suss et al., 2014). Through the description of deformational products (structures, intrabasinal clasts and matrix) specific relationships between the amount of matrix and deformational structures were identified. These relationships show patterns (deformational facies) that are present in stratigraphically constrained MTDs, allowing the role of deformation in the downslope homogenization of MTDs to be examined (Fig. 3.1 and 3.2). The same patterns were observed in other localities where MTDs occur as disconnected exposures, providing additional data on individual deformational facies and helping elucidate the role of deformation processes in MTD evolution. Here, the term homogenization is used to describe the mixing of disaggregated sediments that results in complete destruction of sedimentary structures and layers and the generation of matrix (e.g., Farrell, 1984; Thornton, 1986; Yamamoto and Sawyer, 2012).

3.3. STUDY AREA AND METHODS

The studied MTDs occur at different stratigraphic levels within the ~1.3 km thick Itararé Group, which is a Pennsylvanian to Cisuralian unit developed in the intracratonic Paraná Basin in southeast South America (Fig. 3.1) (e.g. Schneider et al., 1974; Zalán et al., 1990; França and Potter, 1991; Holz et al., 2010). Early studies suggest a shallow marine paleogeography for the Paraná Basin during the

Carboniferous-early Permian interval (e.g., França and Potter, 1991; Santos et al., 1996). However, more recent papers indicate that the Itararé Group's strata accumulated in environments ranging from marginal to relatively deep marine settings during multiple stages of deglaciation associated with the late Paleozoic ice age in southwestern Gondwana (Fallgatter, 2015; Vesely and Assine, 2006; Valdez-Buso et al., 2017). In lithostratigraphic terms, the Itararé Group has been subdivided in three basin-wide intervals (Fig. 1) classified as formations by França and Potter (1991). These three units correspond broadly to the formations previously mapped in outcrop by Schneider et al. (1974) in the southern part of the basin and can be tied to the three palynozones defined by Souza (2006). In this paper, the studied MTDs were positioned in these three wide time intervals, referred to as T1 (Campo do Tenente Fm.), T2 (Mafra Fm.) and T3 (Rio do Sul Fm.) (Fig. 3.1). The occurrence of MTDs in all these time-intervals of the Itararé Group implies that subaqueous landslides were probably recurrent events during basin-fill history (Vesely et al., 2018).

Penecontemporaneous deformational structures were described in the Itararé Group by several authors, who initially, interpreted them mainly as glaciotectonic features associated with glacio-terrestrial deposition (e.g. Leinz, 1937; Almeida, 1948; Canuto, 1985; Martin, 1961; Caetano-Chang, 1984). Subsequent work, however, interpreted most of these structures as being generated by subaqueous mass movements, which is corroborated by their association with turbidites and other types of gravity-flow deposits (e.g. Carneiro and Costa, 2006; Carvalho and Vesely, 2017; d'Ávila, 2009; Eyles et al., 1993; Fallgatter and Paim, 2017; França and Potter, 1991; França et al., 1996; Gama Jr. et al., 1992; Mottin et al., 2018; Rocha Campos, 1967; Salamuni et al., 1966; Sanford and Lange, 1960; Schneider et al. 1974; Suss et al., 2014; Valdez-Buso et al., 2017; Vesely et al., 2005; Vesely and Assine, 2006). These MTDs consist mostly of heterogeneous to homogeneous diamictites (gravely-sandy mudstones), deformed sandstones and mudstones, and large allochthonous blocks (sandstones, rhythmites and mudstones). Recent studies have associated the MTDs with instabilities caused by high sedimentation rates linked with deglaciation (e.g., Carvalho and Vesely, 2017; Fallgatter, 2015; Schemiko, 2018; Suss et al., 2014; Valdez-Buso et al., 2017) or rapid base-level fall due to isostatic rebound (Mottin et al., 2018).

After deposition of the Itararé Group, the Paraná Basin experienced deformation linked to reactivation of ancient basement faults by stresses associated with

convergence at the active margin of the South American Plate, and opening of the Atlantic Ocean (e.g. Zalán et al., 1990; Soares, 1991; Milani, 1997, 2004). However, this post-deposition deformation is, usually, easy to distinguish from mass-transport deformation, because it displays brittle structures that crosscut several layers and deposits and are associated with regional structures (e.g. Rostirolla et al., 2000, 2002, 2003; Trzaskos et al., 2006).

This research was conducted in the eastern belt of the Itararé Group in southern Brazil (Fig. 3.1), where 18 selected outcrops present a wide variety of MTD-related structures, such as folds, faults, boudins, deformed clasts, injectites, and others. MTDs can be generated by one or multiple mass flow events; those deposits generated by one event are termed MTDs, while those formed by multiple events are named MTCs (mass-transport complexes; sensu Ogata et al., 2014b). Mass-transport complexes may also refer to a complex single unit composed of one or more mass-flow events (e.g., Moscardelli et al., 2006). The vast majority of studied localities (13 outcrops) consist of MTDs developed in T3, corresponding to the earliest Permian Rio do Sul Formation (Schneider et al., 1974) and Taciba Formation (França and Potter, 1991). For MTDs of time intervals T-1, T-2 and some MTDs of T-3 (localities 1, 2, 9 and 11; Fig. 3.1) limited exposure and lack of higher resolution stratigraphic control precluded the examination of spatial relationships between different deposits. However, T-3 MTDs in the southern sector of the studied area (Fig. 3.1) are closely spaced, better exposed and are all placed in the upper half of the Rio do Sul Formation, which has been interpreted as a progradational deltaic complex sourced from the east (Schemiko 2018). Stratigraphic surveys in the southern sector of the study area (Schemiko, 2018) show that T3 MTDs in this region are all part of one single mass-transport complex or MTC, thus allowing the spatial relationship between different outcrop localities to be assessed (Figs. 3.1 and 3.2).

MTDs were described in terms of facies composition, bounding relationships with other facies, deformational products, the relative proportion of coherent intrabasinal clasts and matrix, as well as spatial and temporal relationships between different deformational products. These observations were used to further subdivide the deposits into three main deformational facies. In order to better describe some structures, samples were collected and polished slabs produced. In addition to the traditional classification of folds (e.g. Fleuty, 1964; Ramsay, 1967; for more information see Twiss and Moores, 2007; Fossen, 2016), the flow perturbation fold model (e.g.

Holdsworth, 1990; Alsop and Holdsworth, 1993, 2004) was also applied. This model considers that layer-parallel shear folds (LPS) are generated by velocity gradients in the downslope direction and layer-normal shear folds (LNS) are generated by velocity gradients along strike (Alsop and Marco, 2011). Some structures were named based on their geometric similarities with structures typically observed in ductile shear zones in metamorphic rocks (e.g. Ogata et al., 2016), which are a descriptive and non-genetic terminology used in structural geology (e.g. Passchier and Trouw 2005).

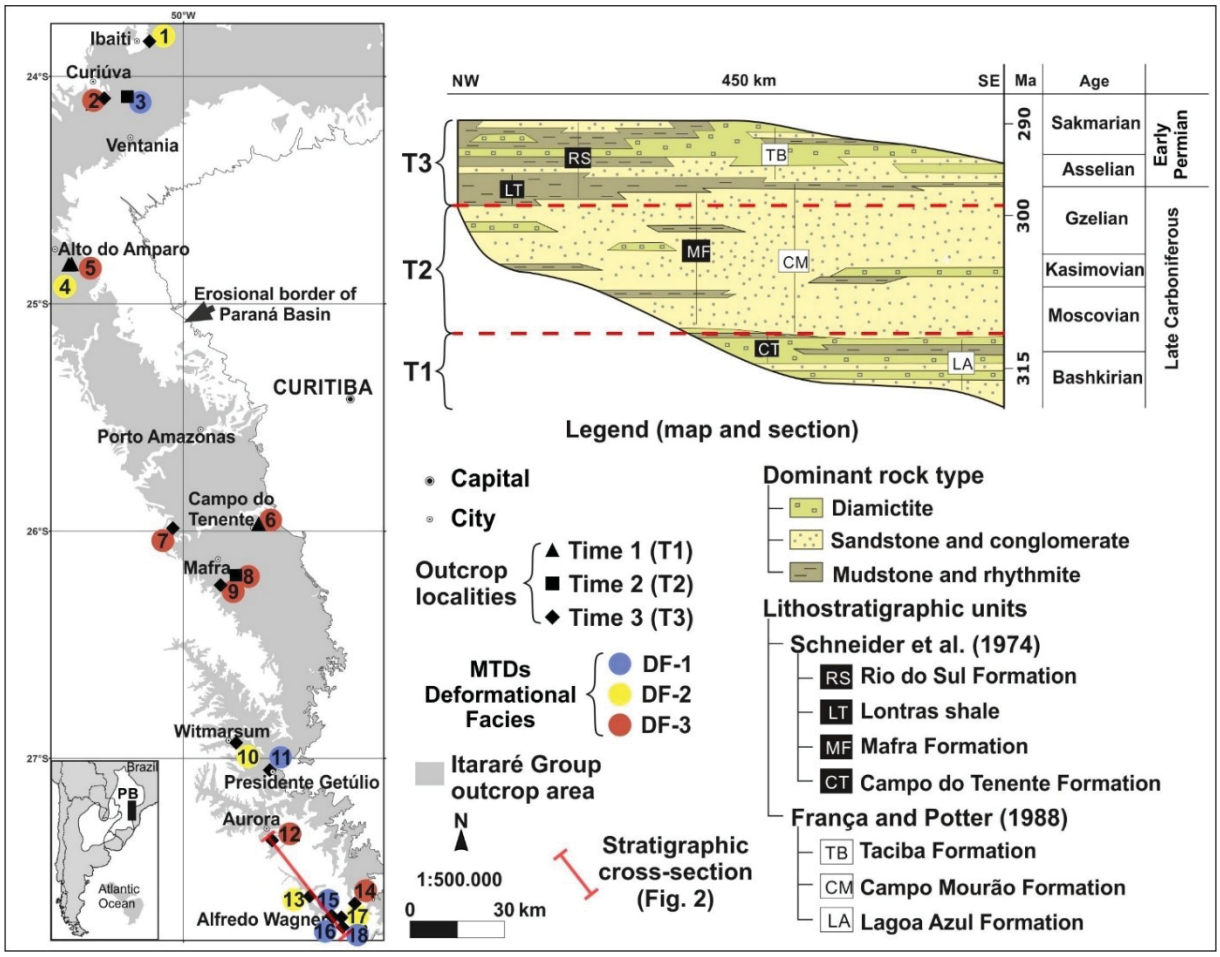

Fig. 3.1: Location map and stratigraphic setting of the study area in the Paraná Basin in Brazil. The geographic location, stratigraphic position and deformational facies of each examined mass-transport deposit (outcrop locality) are indicated by numbers and symbols respectively. The approximate location of the stratigraphic cross-section of Fig. 3.2 is also indicated on the map.

3.4. OBSERVATIONS

3.4.1. General characteristics of studied MTDs

The thickness of the studied MTDs, generally, ranges from about 5 m to 10s of meters, as indicated by vertical profiles from previous studies (e.g., Carvalho and

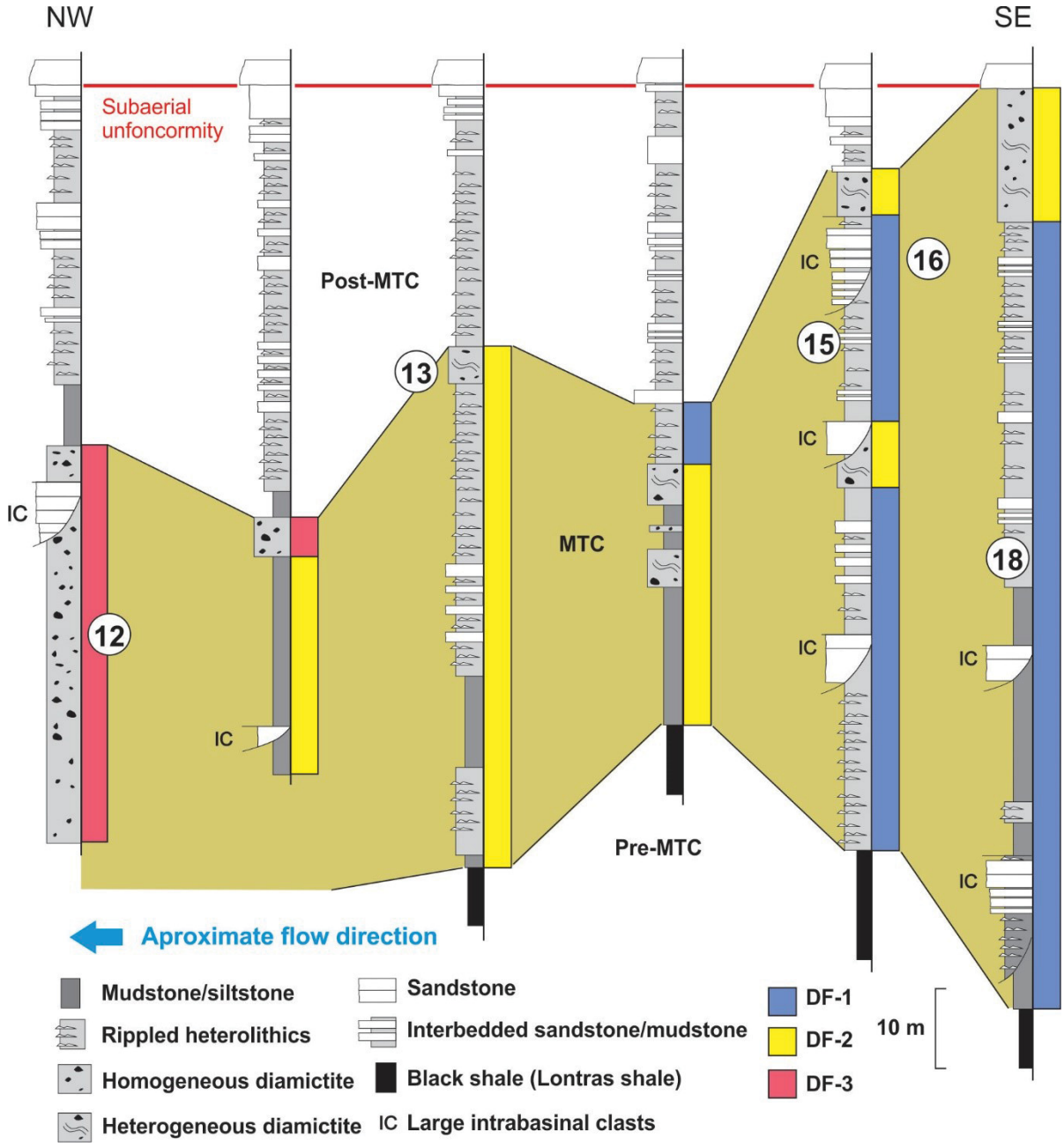

Fig. 3.2: Stratigraphic cross-section (not to horizontal scale) showing the upper Rio do Sul Formation in the southern region of the study area (see Fig. 3.1). Vertical distribution of deformational facies (DF-1, DF-2 and DF-3) and the approximate location of examined localities (encircled numbers) within the MTC interval are indicated.

Vesely, 2017; Mottin et al., 2018; Schemiko, 2018). Typically, the limits and thickness of a single MTD are hard to assess due to limited exposure. When exposed, boundaries between MTD and non-MTD strata are sharp, with the base of MTDs usually being erosive and irregular. The top surfaces of MTDs are generally flat but low amplitude relief has been reported locally, onto which fine-grained facies may be ponded (e.g., Vesely et al., 2018).

In terms of composition, MTDs consist of 1) large intrabasinal clasts (IC) of sandstone and rhythmites (Fig. 3.3A-D), 2) deformed sandstone, rhythmite and shale (Fig. 3.3C and E), and 3) heterogeneous (banded matrix) to homogeneous (massive matrix), sandy-muddy diamictites with dispersed granules to boulders of intrabasinal clasts (sandstones, shale, rhythmites and plant fragments) and extrabasinal clasts (granites and metamorphics), some of which are striated and faceted (Fig. 3.3D and F). Heterogeneous diamictite consists of pebbly-sandy-mudstone containing disrupted fragments of deformed strata in which original bedding is still detectable. All 18 localities show at least one type of deformational structure (such as folds, faults, boudins) and many of them also have allochthonous intrabasinal clasts and poorly-sorted matrix. In most studied localities, both extensional and compressional structural styles are identified in the same exposure and in equivalent proportions.

3.4.2. Deformational products

3.4.2.1. Folds

Folds are cylindrical to gently curvilinear and are classified as gentle (Fig. 3.4A and 3.5A) to tight (Fig. 3.4B) folds, rarely isoclinal, and symmetrical (Fig. 3.4A) or asymmetrical (Fig. 3.4B and C). Symmetrical folds tend to display vertical axial planes with horizontal hinges (upright horizontal folds; Fleuty, 1964), while asymmetrical folds show diverse hinge and axial-plane orientations ranging from inclined to horizontal (recumbent folds; Fleuty, 1964; Fig. 3.5B). The folds were classified as harmonic to disharmonic and, locally, polyclinal. Both sharp (kink band folds; Fig. 3.5D) and rounded fold hinges are observed.

Some folds are associated with faults such as drag folds (Fig. 3.6D) or fault-propagation folds. Other features include intrastratal slickenlines associated with folded shale, symmetric boudins on fold limbs, rootless folds (Fig. 3.4E), parasitic folds (Fig. 3.4F), and monoclinal folds with axially-elongated lithic (Fig. 3.4G) and plant debris. Some folds are associated with upward intrusions from mud-rich rocks below sandstones (mud diapirs, Fig. 3.4H). Folds may show both unimodal orientation patterns (axis, axial-plane and facing) (Fig. 3.5A and C), possibly associated with layer-parallel shear (LPS; Alsop and Marco, 2011), or bimodal directions (axis, axial-plane and/or facing, kink band folds) (Fig. 3.5B and D), possibly linked to layer-normal shear (LNS; Alsop and Marco, 2011).

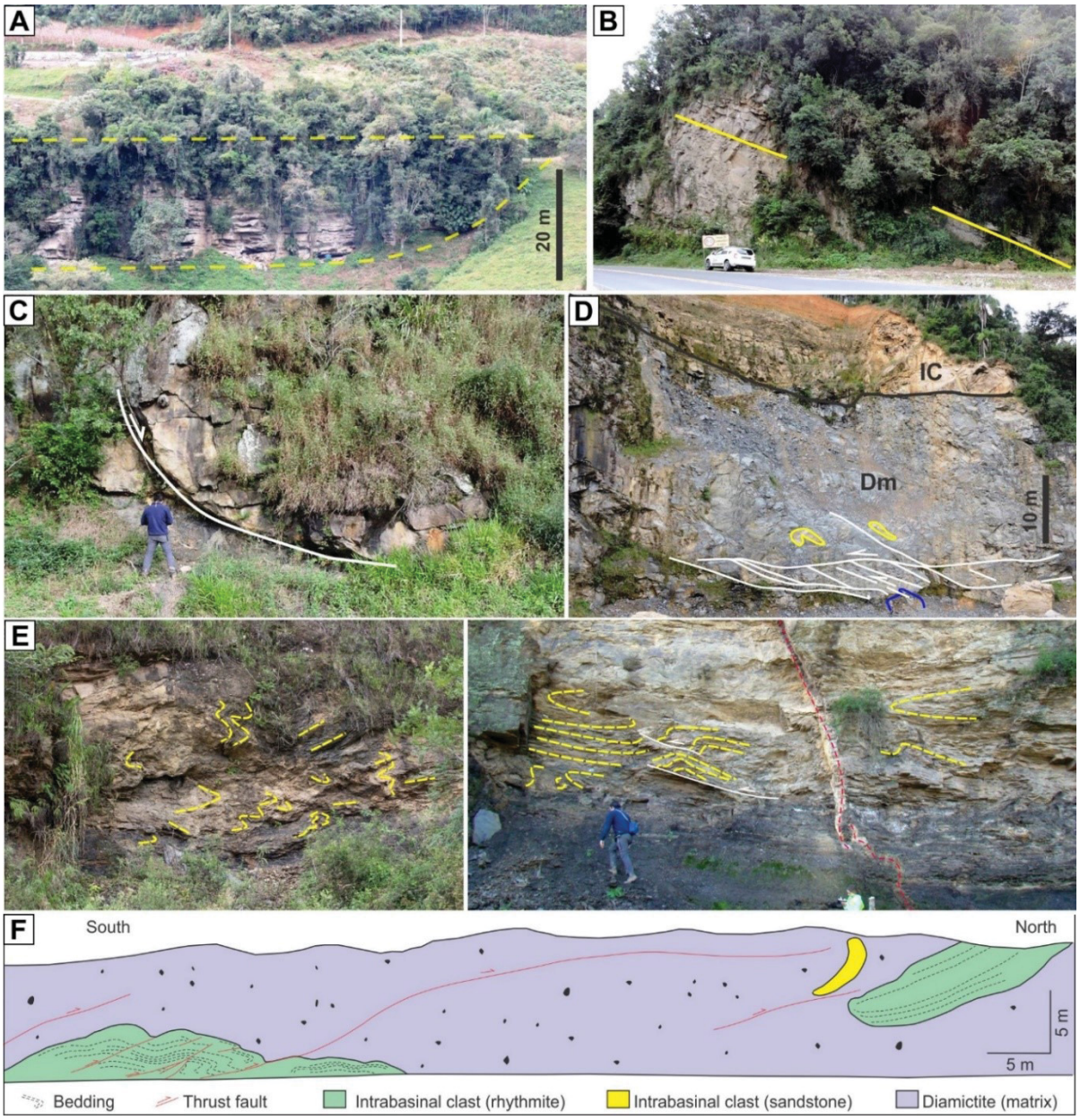

Fig. 3.3: Outcrop expression of MTDs and intrabasinal clasts. A) Partial cliff exposure of a large allochthonous sandstone block (approximate limits highlighted by dashed line; near locality 16). B) Tilted (rotated) bedding in sandstone block of locality 16 (note the apparent lack of internal deformation). C) Listric fault in a sandstone block in locality 17. D) Large intrabasinal clast (IC) resting on internally deformed diamictite (Dm) in locality 12. Deformation within the diamictites included reverse shear zones of continuous clay smear (highlighted by white lines; for detail see Fig. 3.6D) and deformed sandstone clasts (highlighted by yellow line; for detail see Fig. 3.4E) and rhythmites clasts (highlighted by blue lines; for detail see Fig. 3.6D). E) Interval of rhythmite and sandstones deformed in locality 13, including folds (some highlighted by yellow dashed lines), reverse faults (white lines) and injectites (red dashed lines). F) Sketch showing a partial view of MTD exposure in Vila Ruthes quarry (locality 9). Note that contrary to previous examples, the intrabasinal clasts are internally deformed and disrupted.

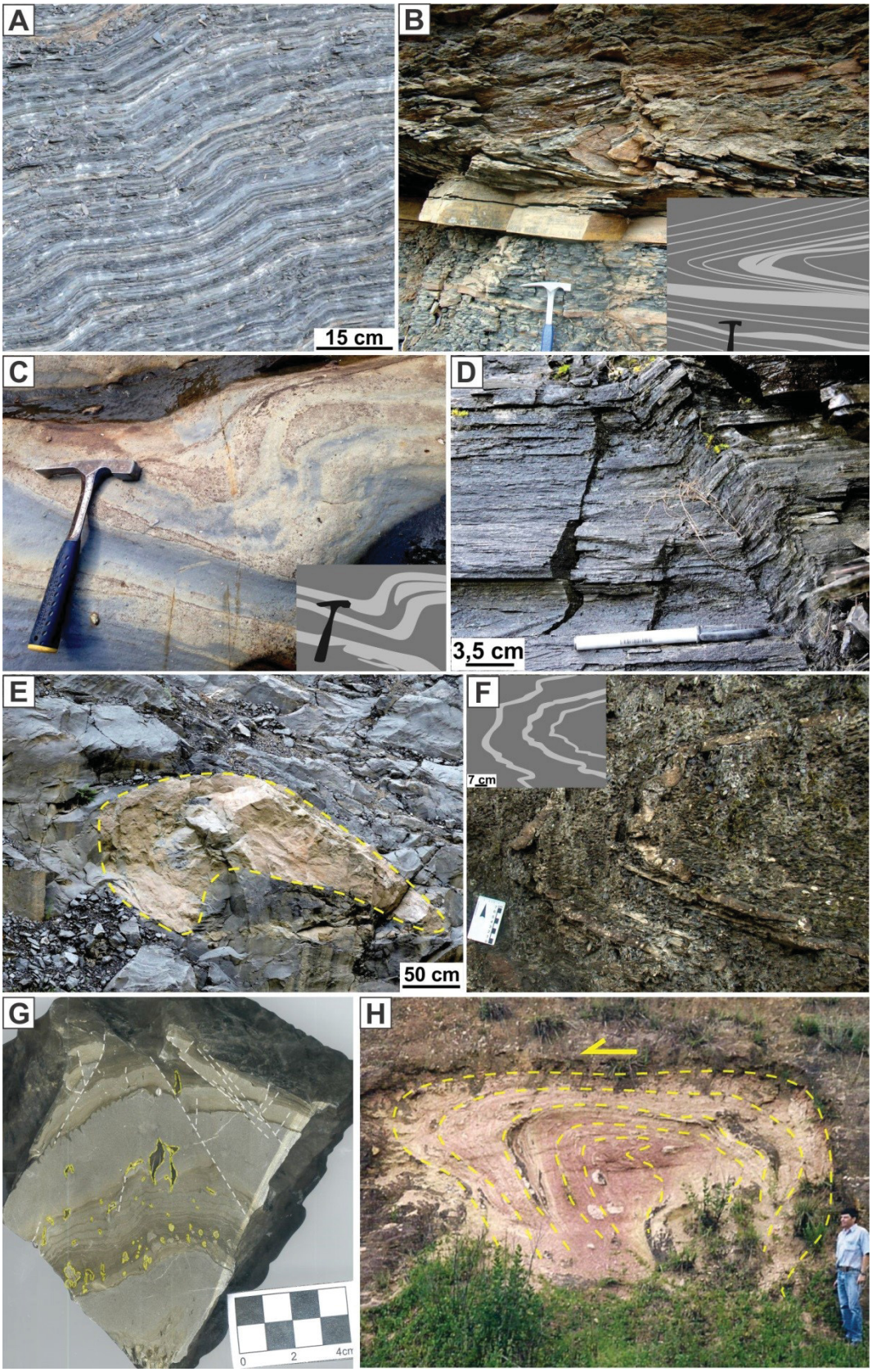

Fig. 3.4: Different types of folds observed in MTDs. A) Gentle and symmetrical folds (locality 18). B) Closed and asymmetrical fold (locality 11). C) Asymmetrical fold (locality 1). D) Kink-band fold (locality 15). E) Rootless folds (highlighted by yellow dashed lines; locality 12). F) Parasitic folds (locality 11). G) Elongated intraclasts

(highlighted by yellow dashed lines) orientated parallel to the axial surface in the fold hinge (locality 9). H) Fold with preferential vergence (indicated by yellow arrow) generated by mud diapirism in which fold geometry follows the diapir shape (locality 2).

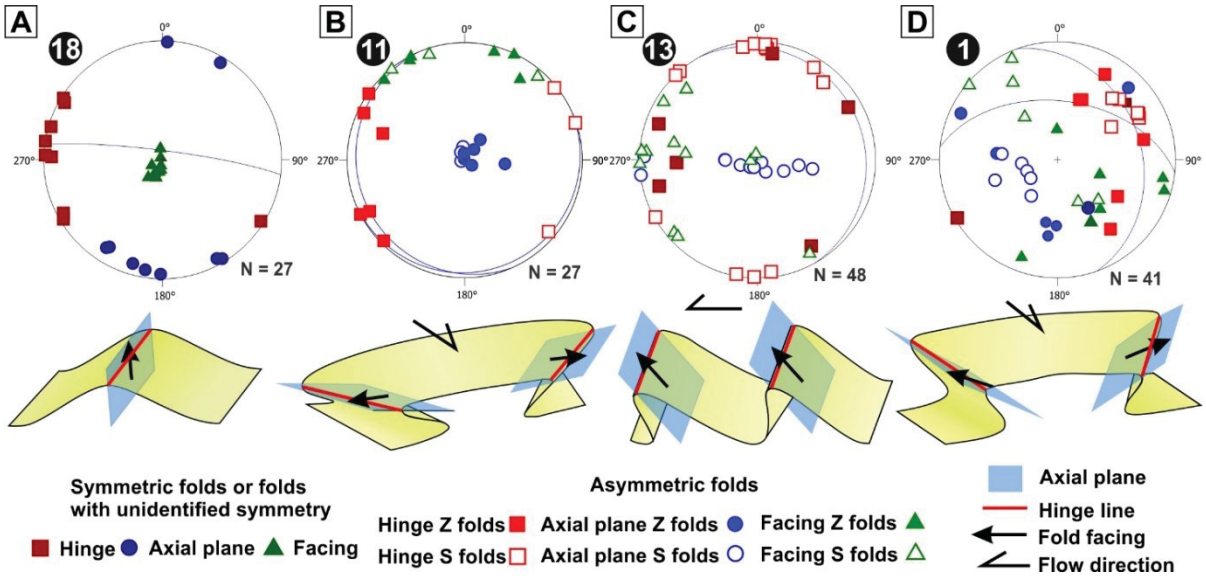

Fig. 3.5: Stereographic data and schematic cartoons for folds: A) Symmetric folds with unimodal pattern (LPS; locality 18). B) Recumbent folds with bimodal pattern of fold axes (LNS; locality 11). C) Asymmetric folds with unimodal pattern and rotation of some fold hinges and facing (LPS; locality 13). D) Folds with bimodal pattern of axial plane and fold facing (LNS; locality 1). Schematic fold illustrations adapted from Alsop and Marco (2011).

3.4.2.2. Faults

Faults range in length from a few cm to several m, and form individual planes or clusters (fault zones) with planar (Fig. 3.6A and B), wavy or anastomosed geometry (Fig. 3.6C and D). They include reverse (Fig. 3.6A, C, D and 7A) and normal faults (Fig. 3.6B, 3.7B and C). Faults may be synthetic or antithetic to the flow direction, as defined by kinematic indicators such as fold vergence and asymmetric boudins. In some localities, faulting resulted in significant bed tilting (about 10° or more; Fig. 3.6A), while in other localities, faults are associated with fault-propagation folds and drag folds (Fig. 3.6D).

Some faults are marked by microfaulting with mm-thick concentrations of clay and/or sand which we classify as continuous or discontinuous clay/sand smear (Fig. 3.6C, E, F and G). The term clay is used here with respect to the grain size of sediments. Continuous clay smears are found in diamictites with silty to sandy-muddy matrix and may exhibit decollement surfaces with slickensides (Fig. 3.4F). They show similar features to deformation bands generated in sediments with more than 40% of

clay described, for instance, by Fisher and Knipe (2001). Discontinuous clay smear occurs in rhythmites and are similar to the structures discussed by Kristensen et al. (2013), which are generated when muddy laminations are dragged by faulting (Fig. 3.4G). Sand smears are associated with clay smears and result from sand dragging (Fig. 3.4G). Continuous clay smear can form mm- to m-thick clusters, and locally faults with cm-thick sheared muddy cores were observed. In thin-bedded rhythmites, faulting may generate shear zones whose geometry is similar to SC structures (Fig. 3.4H). In these shear zones ‘S surfaces’ consist of bedding that is deflected according to the sense of shear along ‘C surfaces’. The ‘C surfaces’ display clay smear and sometimes they also show detachment surfaces with slickensides.

3.4.2.3. Boudins

Boudins are classified as symmetric (Fig. 3.8A and B) or asymmetric boudins (Fig. 3.8C). Symmetric boudins of variable dimensions (cm to m) were observed in massive or stratified sandstone beds hosted in mudstone (Fig. 3.8A) or diamictite (Fig. 3.8B). Some occur along the limbs of recumbent folds that tend to show thickened hinges. The mudstone host layers may or may not preserve lamination (Fig. 3.8A). Symmetric boudins display elongated and convex-lens shapes with rounded and no inter-boudin surface, and the local presence of necking, allowing their classification as drawn boudins according to Goscombe et al. (2004).

Asymmetric boudins occur in heterogeneous diamictite as mudstone layers hosted by sandstone (Fig. 3.8C). They show rounded, rhomboid, sigmoid or lenticular shapes with tapered wings. The inter-boudin surface is straight to slightly curved and is associated with shear bands that comprise clay smears. Boudin blocks show backward rotation resulting from antithetic displacement with respect to shearing. Some boudin blocks may be compartmentalized into smaller blocks as a result of progressive boudinage (Fig. 3.8C). Symmetric and asymmetric boudins might also display rotation, changes in shape and displacement due to post-boudinage deformation, such as shearing at the margins of boudins blocks and faulting (Fig. 3.8D). This post-boudinage deformation is restricted to the MTD, is sometimes limited to particular intervals or portions within the MTD, and is therefore also interpreted as mass flow deformation.

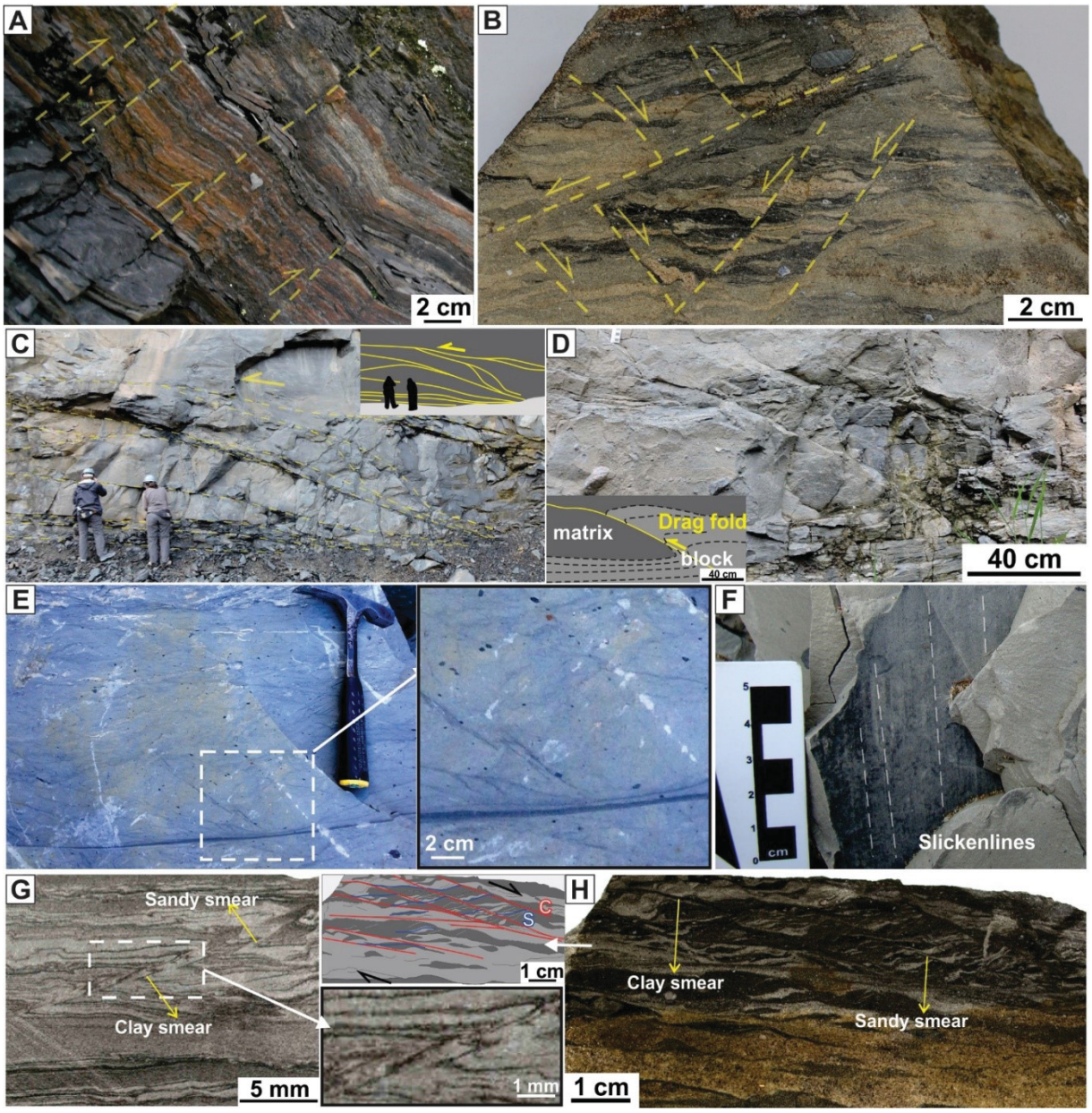

Fig. 3.6: Different types of faults and associated features observed in MTDs. A) Reverse fault zone with planar surfaces (locality 15). B) Normal faults (locality 10). C) Reverse anastomosed faults zone, which are indicated by yellow dashed lines in the inset (locality 12). D) Reverse fault with associated drag fold (locality 12). E) Continuous clay smear in diamictite, which correspond to the dark gray line features (locality 8). F) Displacement surface with slickenlines in continuous clay smear (looking down on the plane; locality 8). G) Discontinuous clay-sand smear. The smearing of sand and clay evidence the faulting (locality 9). H) Clay-sand smear with SC-like features (locality 10).

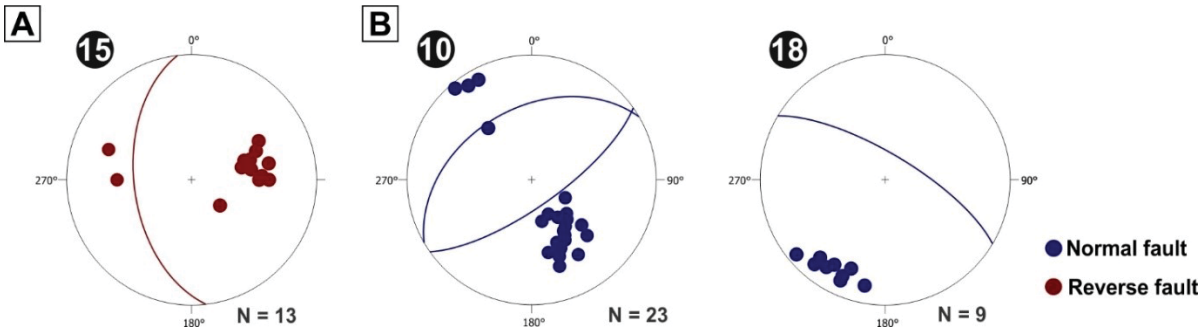

Fig. 3.7: Stereographic data distribution for faults in MTDs: A) Reverse faults (locality 15 example). B) Normal faults (localities 10 and 18 examples).

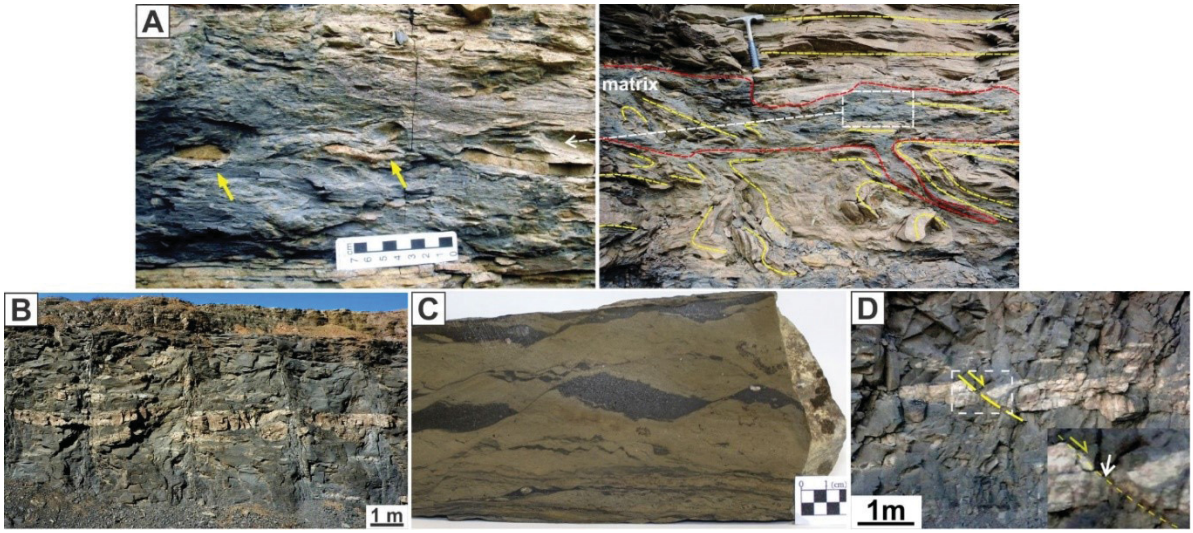

Fig. 3.8: Examples of boudins in MTDs. A) Symmetric boudins (indicated by yellow arrows) in sandy-layers associated with folded rhythmite, in which the muddy layer shows no preserved lamination. This reflects sediment mixing during fluidization thereby generating a muddy matrix (proto-matrix). The fluidization of mud associated with boudinage resulted in the accumulation of muddy matrix in pods (broadly highlighted by red dashed line in the detailed photo; locality 13). B) Symmetric boudins in sandstone hosted in diamictite (locality 6). C) Asymmetric boudins in mudstone layer hosted in sandstone (locality 10). D) Symmetric boudin deformed by post-boudinage normal faulting, but generated during continued mass flow (locality 6). The fault was filled by matrix of the diamictite (indicated by white arrow) during the ongoing deformation.

3.4.2.4. Injectites

Injected sands, occurring as dikes, and more rarely, as sills (Fig. 3.9A) range in thickness from a few mm to dm, and were identified in a variety of host rocks such as diamictite (banded and homogeneous), shale, rhythmite and sandstone. These injectites are more typically composed of very fine to medium sand but gravelly and silty injections were also observed. Sills are tabular and sometimes folded (Fig. 3.9F).

Dikes show regular (Fig. 3.9B) to irregular (Fig. 3.9C and D) borders, tabular (Fig. 3.9B) to anastomosed shapes and may also display an *en echelon* pattern (Fig. 3.9C).

Injectites may contain fragments ripped out from the host rock, or portions of host rock surrounded by the injectite swarms forming breccia (Fig. 3.9D). Sand dikes typically intercept several meters of strata and sets of dikes usually show a consistent orientation, based on the measured injectite planes. More locally, random injectite networks with breccia present features suggestive of sand flows (Fig. 3.9E; e.g., Callot et al., 2008). Locally, injectites are subparallel to continuous clay smears and sometimes occur as the infilling of displacement surfaces (Fig. 3.9B). When identified, the parental unit of injectites consist of deformed layers, deformed relicts of layers or allochthonous clasts. The injectites were observed to cut structures generated during mass flow (Fig. 3.9A and C), or where themselves deformed by mass flow structures, or in some cases both (Fig. 3.9F).

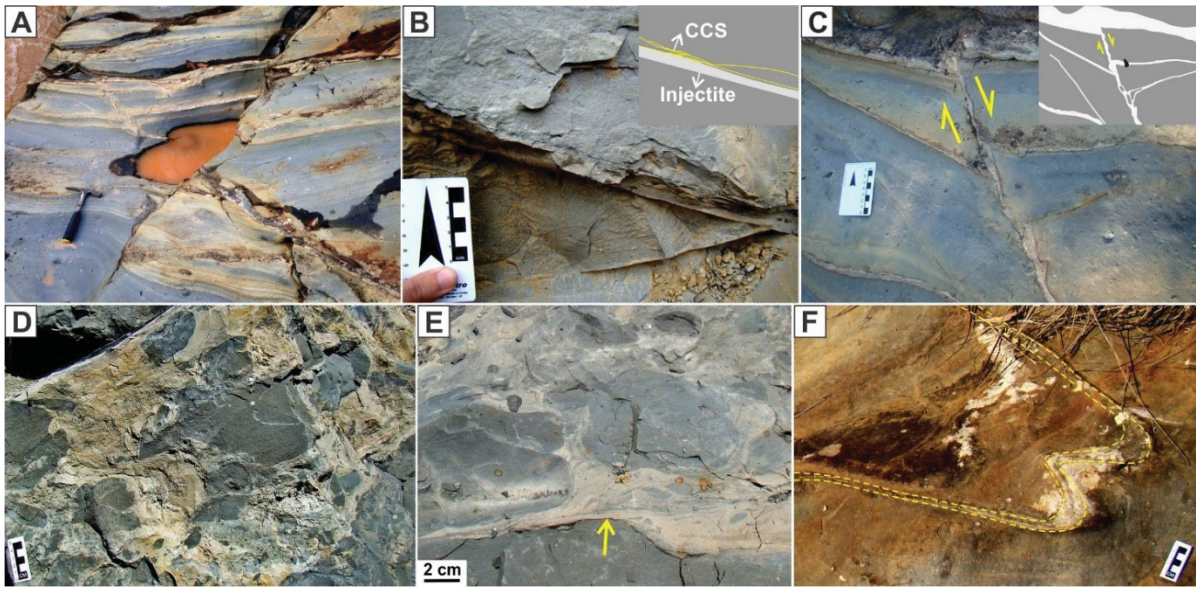

Fig. 3.9: Injectites. A) Sandy injectites in the form of sills and dikes (locality 1). B) Tabular injectite parallel to continuous clay smear (CCS; locality 8). C) Tabular and *en echelon* dikes associated with tabular sills (yellow arrows indicate the kinematics based on the *en echelon* pattern; locality 1). D) Breccia associated with sandy injectite (locality 7). E) Features associated with flow inside sand injections (indicated by yellow arrow; locality 7). F) Folded sandstone sill (highlighted by yellow dashed line; locality 1).

3.4.2.5. Intrabasinal clasts

These consist of coherent fragments of intrabasinal material (more commonly sandstone and rhythmite) that are involved in mass flows. In the examined outcrops,

these clasts typically range from 10-cm-sized cobbles to megablocks up to a few hundreds of meters. They display extremely variable shapes, including elongated, rounded and angular clasts.

Intrabasinal clasts display deformation including preferential orientation of long axes (Fig. 3.10A) and bed tilting, as well as internal deformation such as folds and faults (Fig. 3.10B and C). The borders of the clasts may display shearing resulting in layers of sediment collected from the clast and incorporated into the matrix (Fig. 3.10D). These features are geometrically similar to deformation around porphyroblasts (e.g., Fossen, 2016). Clast borders may also show disintegration and mutual injection between material of the clasts and the surrounding matrix (Fig. 3.10E), assimilation/incorporation by matrix (Fig. 3.10F and G) and grooves and stretch marks (Fig. 3.10H) similar to those described by Ogata et al. (2012a and 2014b, respectively).

3.4.2.6. Other shear-related structures

Besides faults, folds and boudins, other structures that indicate shearing and which often serve as important kinematic indicators were also identified in rhythmites and diamictites (e.g., Ogata et al., 2014c). Shearing of lamination around rigid clasts generates ‘quarter structures’ characterized by contractional and extensional features around granite clasts (Fig. 3.11A), that are similar to quarter structures in mylonitic zones (see Fossen, 2016). Sigma structures (σ) consist of asymmetric sandstone clasts surrounded by a cohesive matrix showing sigma or fish geometry (Fig. 3.11B). These are similar to structures named as pseudo-sigma by Ogata et al. (2016). Intrastratal striated detachment surfaces were observed on mudstone bedding planes (Fig. 3.11C). These structures are characterized by the presence of slickenlines, in multiple lamination planes, and indicate the trend of movement, but lack steps which precludes determining the direction. Irregular fragments resulting from shearing and disruption of bedding (Fig. 3.11D) occur in diamictite with heterogeneous matrix (banded) and are similar to those structures described and interpreted as the product of progressive deformation of bedded sediments by Ogata et al. (2012a). Sheared lamination and fragments are also observed, which give a banded aspect for diamictites (Fig. 3.11E, F and G).

3.4.2.7. Matrix

The studied MTDs may show partial or total mixing of different grain-size components (mud to gravel) which gives rise to a heterogeneous (with relicts of original bedding; Fig. 3.11F and G) to homogeneous (fully mixed) matrix (Fig. 3.11H). This matrix can be described as a poorly-sorted sandy mudstone with dispersed gravel (diamictite). The matrix adjacent to intrabasinal clasts tends to show similar composition with these clasts. This characteristic results from mutual injections between clast and matrix sediment, and deformation at clast borders (Fig. 3.10G, 3.10H and 3.11G). These relationships indicate that the matrix is a result of incorporation (assimilation) of sediment from the clasts. The heterogeneous (banded) matrix is characterized by mm- to dm-thick compositional/textural bands that can be well-defined (Fig. 3.4C and 3.11G) to very subtle (Fig. 3.11F). In the heterogeneous diamictites, it is possibly to observe that these bands were subsequently faulted, folded (Fig. 3.4C) and disrupted (Fig. 3.11G) by deformation processes associated with the mass flow.

3.4.3. Deformational facies

Based on the relative proportion of coherent intrabasinal clasts and matrix, and on the linkage between different structures, the studied MTDs were grouped into three main deformational facies (DF-1 to 3; Fig. 3.12). These facies do not seem to occur preferentially in a time interval as they are found in different stratigraphic levels. The spatial distribution of these facies is well constrained only in the southern area of interval T3 (upper Taciba/Rio do Sul Formation) where larger outcrops are more closed spaced and vertical and horizontal transitions from one facies to another can be better defined than elsewhere (see Fig. 3.2).

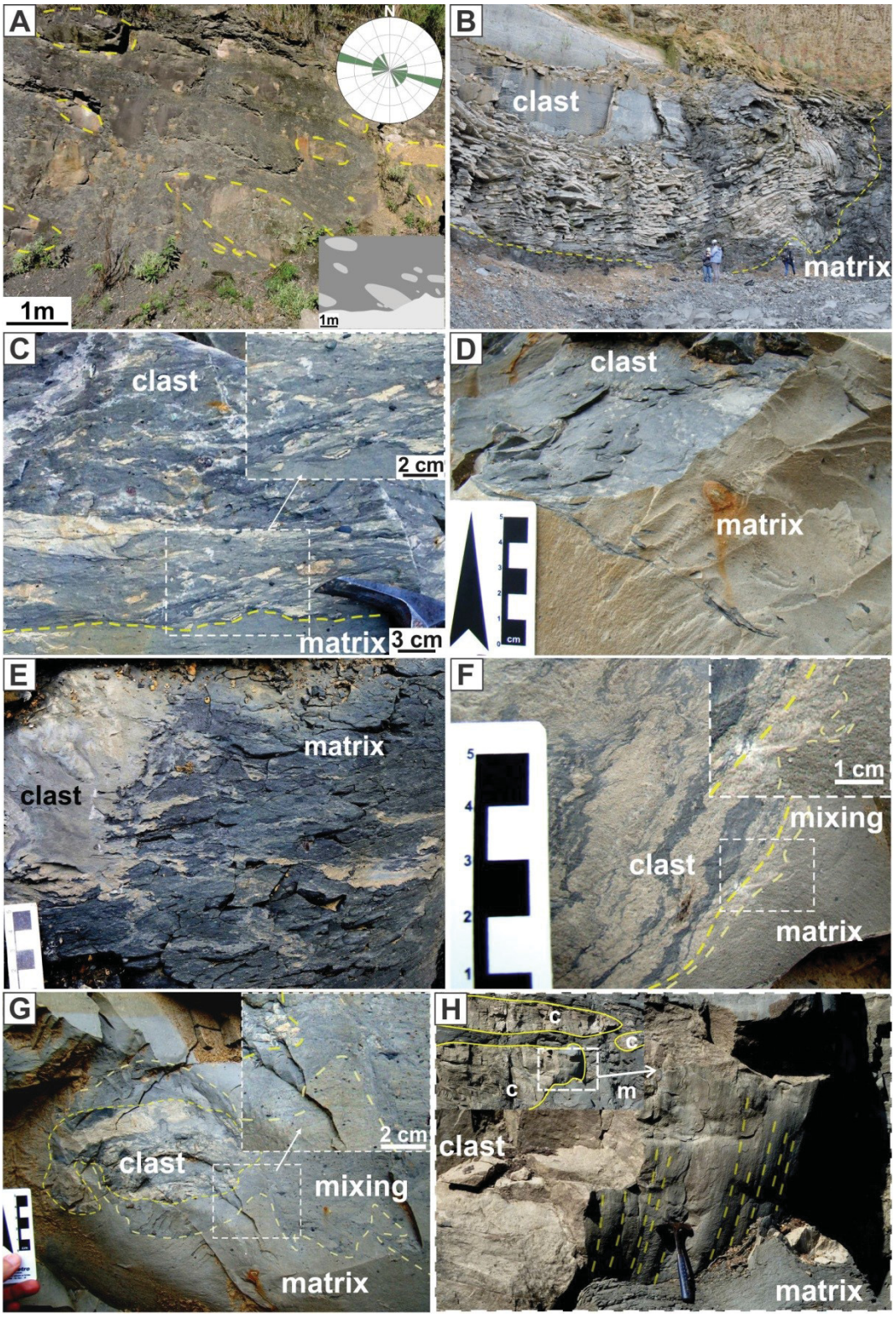

Fig. 3.10: Intrabasinal clasts in MTDs. A) Oriented sandstone clasts (locality 14). B) Clast of folded rhythmite (locality 9). C) Clast with disrupted lamination (locality 8). D) Shale clast with sheared border and filming of sediments incorporated into the matrix (locality 8). E) Disintegration at the border of sandstone clast with mutual injection (matrix injection in clast and clast sediments injection in matrix) and incorporation of clast material by matrix (locality 9). F, G) Incorporation of clast sediment by matrix generating a mixed zone at clast borders (locality 8). H) Grooves/stretch marks

(highlighted by yellow dashed line) at sandstone clast border (c; highlighted by yellow line) dispersed in diamictite matrix (m; locality 6).

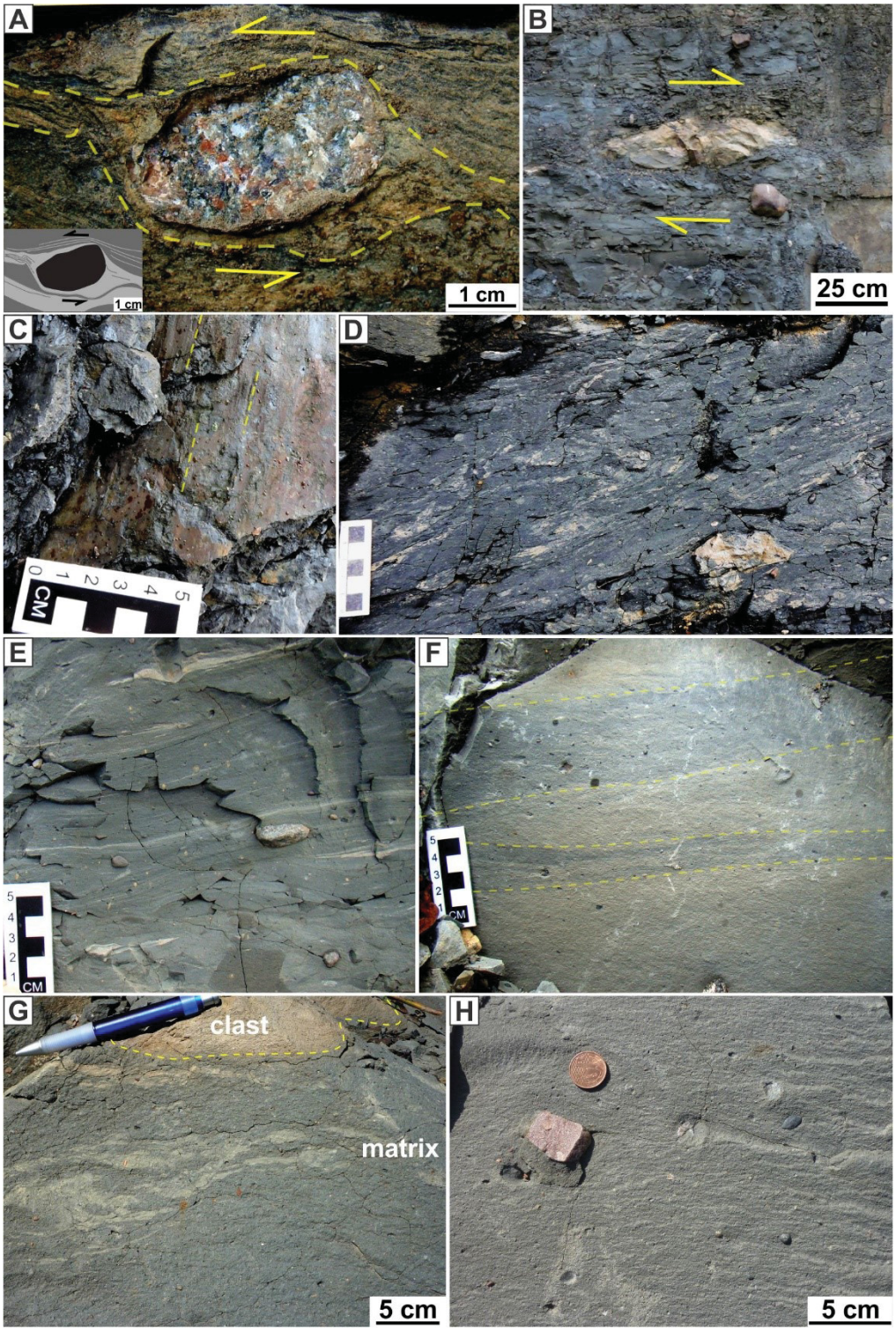

Fig. 3.11: Shear-related and mixing structures. A) Quarter structure around a granite clast (locality 10). B) Sigma structure formed in sandstone clast (locality 7). C) Intrastratal striated detachment surface along a folded shale bedding plane, where the slickenlines (indicated by yellow dotted lines) were generated by flexural folding (locality 10). D) Progressive disruption of lamination (locality 9). E) Sheared lamination

and fragments (locality 7). F) and G) Heterogenous matrix with discrete (F; locality 8) and defined (G; locality 6) textural/compositional banding. H) Homogenous matrix (locality 6).

3.4.3.1. Incipient MTDs with a lack of matrix

DF-1 is represented by incipient MTDs displaying a lack of matrix (Fig. 3.12), well preserved bedding commonly with sedimentary structures (Fig. 3.3B), and a structural assemblage consisting mainly of faults and folds (Fig. 3.3C, 3.4A, 3.4B and 3.5A), with symmetric boudins occurring along fold limbs (locality 11; Fig. 3.1). The mudstone layers that host symmetric boudins (formed in sandstone layers) preserve their lamination which is deformed around the boudins. In some cases, faults are directly associated with the folding processes such as where faults develop along the axial surface of folds, or drag folding along faults (localities 3 and 15, respectively; Fig. 3.1). While in other outcrops, faults show no direct relationship with folds and simply cut across them (localities 15 and 18; Fig. 3.1).

Gentle to open folds tend to show no thickness variation from limb to hinge (Fig. 3.4A; locality 18), whereas closed to tight folds may display thickened hinges (Fig. 3.4B; locality 11). Some particular types of folds identified in DF-1 include monoclinal folds, diapiric folds (Fig. 3.2F), parasitic folds (Fig. 3.2H) and kink band folds (localities 16, 3, 11 and 15 respectively; Fig. 3.1).

3.4.3.2. Mature MTDs with <50% matrix

DF-2 encompasses mature MTDs in which banded (locality 1; Fig. 3.1, and 3.4C) or mostly massive (localities 4, 10, 13 and 17; Fig. 3.1 and 3.8A) matrix forms up to 50% of the volume of the deposit (Fig. 3.12). Matrix occurs as partially mixed zones in the vicinity of intrabasinal clasts (Fig. 3.8A). The matrix tends to preserve little or no bedding or lamination, while the intrabasinal clasts preserve bedding which is usually deformed. These MTDs commonly show a greater variety of deformational structures than DF-1, which include folds (Fig. 3.3E and 3.4C), faults (Fig. 3.3E and 3.6B), symmetric and asymmetric boudins (Fig. 3.8A and C, respectively), injectites (Fig. 3.3E, 3.9A, C and F), and other shear-related features such as quarter-like structures (Fig. 3.11A). Folds usually display rounded hinge zones (Fig. 3.4C) and locally occur associated with faults in the form of drag folds (locality 4; Fig. 1). Folds may show open to tight interlimb angles and be upright to recumbent. In some cases, significant variation in fold geometry was identified in the same MTD; although no clear

pattern of distribution was observed. Particular kind of faults include discontinuous clay-sand smears (locality 10; Fig. 3.1 and 3.6H). Injectites are also common in DF-2, and may cut previous deformation structures (locality 13; Fig. 3.1 and 3.3E) or be subsequently deformed (localities 1 and 10; Fig. 1, 3.9F).

Symmetric boudins form in massive sandstone layers hosted in mudstone and occur along fold limbs (Fig. 3.8A). The mudstones show no lamination preserved around the boudins blocks; while in portions where there is no sandstone boudinage, internal lamination is still preserved in the mudstone. Boudin blocks (sensu Goscombe et al., 2004) generated by asymmetric boudinage tend to still be connected through the mud smeared by the associated faulting (Fig. 3.8C). Subsequent gentle folds generated during continuing mass flow can even slightly modify the orientation of asymmetrically boudinaged layers.

3.4.3.3. Evolved MTDs with >50% matrix

DF-3 is composed of evolved MTDs in which matrix forms more than 50% of the deposit (Fig. 3.3D, 3.3F and 3.12). It includes heterogeneous diamictites, with disrupted and highly deformed intrabasinal clasts (Fig. 3.3D, 3.3F and 3.10A to H) with poorly preserved bedding (Fig. 3.11E), banded diamictite (Fig. 11D, F and G), and homogenized diamictite (Fig. 3.11H). The matrix may display subtle change on a metric scale from homogeneous to heterogeneous within the same MTD outcrop (localities 6, 8, 9 and 12; Fig. 3.1, 3.11G and 3.11H). Deformational structures such as folds, faults, boudins and other shear-related structures are visible once they deform remnants of bedding or banded matrix (Fig. 3.11D). Besides the matrix, continuous clay smears (Fig. 3.6C to F) are an important deformational product in DF-3 as they record deformation independent of the presence of intrabasinal clasts, relict bedding or banded matrix (localities 8 and 12; Fig. 3.1). Faults can form drag folds (Fig. 3.6D) or fault-propagation folds or even deform previous folds. Symmetric boudinage seems to be an important process by which m-scale, elongated blocks have been formed in this deformational facies (locality 6; Fig. 3.1 and 3.8B).

For most evolved MTDs displaying DF-3 it is difficult to define the temporal relationship between structures due to the lack of physical interaction or obliteration, once the structures are highly dispersed. Reorientation of extra- and intrabasinal clasts is the main record of deformation in some cases (localities 8 and 14; Fig. 3.1 and 3.10A). Sedimentary clasts formed by rupture or boudinage of larger sandstone blocks

commonly show faults, folds, boudins and internal shear-related structures that predate rupture (Fig. 3.3F, 3.4E, 3.4G, 3.10B, 3.10C and 3.10E). Late deformation in intrabasinal clasts includes faulting (Fig. 3.6D and 3.8D) and, more commonly, shearing (Fig. 3.10D to G) and 'grooves' that affect their borders (Fig. 3.10H). The matrix sometimes shows shearing when it occurs between closely spaced clasts. In the matrix, shearing of fragments of blocks and remnants of lamination are observed (Fig. 3.11D, E and F). Injectites usually form after the main deformation as they cut the main structures (Fig. 3.9B and D).

3.5. DISCUSSION

3.5.1. Deformation processes within deformational facies

Deformation associated with mass gravity-flows occurs at shallow depths and therefore commonly involves unlithified to only poorly-lithified sediments (e.g., Alsop and Marco, 2014; Alves and Lourenço, 2010; Brooks et al., 2018; Festa et al., 2012; Fisher, 1983; Hodgson and Brooks, 2018; Martinsen, 1994; Nardin, 1979; Ogata et al., 2012a,b; Sobiesiak et al., 2016). In the sedimentological literature, mass flows and their deposits are usually defined as slides, slumps and debris flows based on the main transport mechanism and the presence of internal deformation (e.g., Dott, 1963; Nardin, 1979; Ogata et al., 2012a; Talling et al., 2012; Tripsanas et al., 2008). The deformational facies described herein broadly represent three different degrees of homogenization of sediments (disaggregation and mixing), which are represented by the proportion of matrix. In general, this deformation scheme is similar to MTD facies described by Ogata et al. (2012a,b), where DF-1 corresponds to slide/slump facies, DF-2 is a transition between slide/slump and blocky-flow facies, and DF-3 is a transition between blocky-flow and debris-flow facies. The identification of the three different facies in the MTC of the southern sector of the study area (Fig. 3.1 and 3.2) suggests that different degrees of homogenization of sediments, promoted by a variety of deformational processes, acted during the generation of the unit. In this MTC, the intrabasinal clasts in DF-3 show similar composition, primary depositional origin and internal deformation to the deformed sediments of DF-1 and DF-2. These observations suggest that the deformational facies represent different degrees of progressive homogenization of sediments. The deformation processes within incipient, mature and evolved MTDs, and their association with deformational facies marked by

remobilization of poorly to unlithified sediments, are summarized in Figure 3.13 and described below.

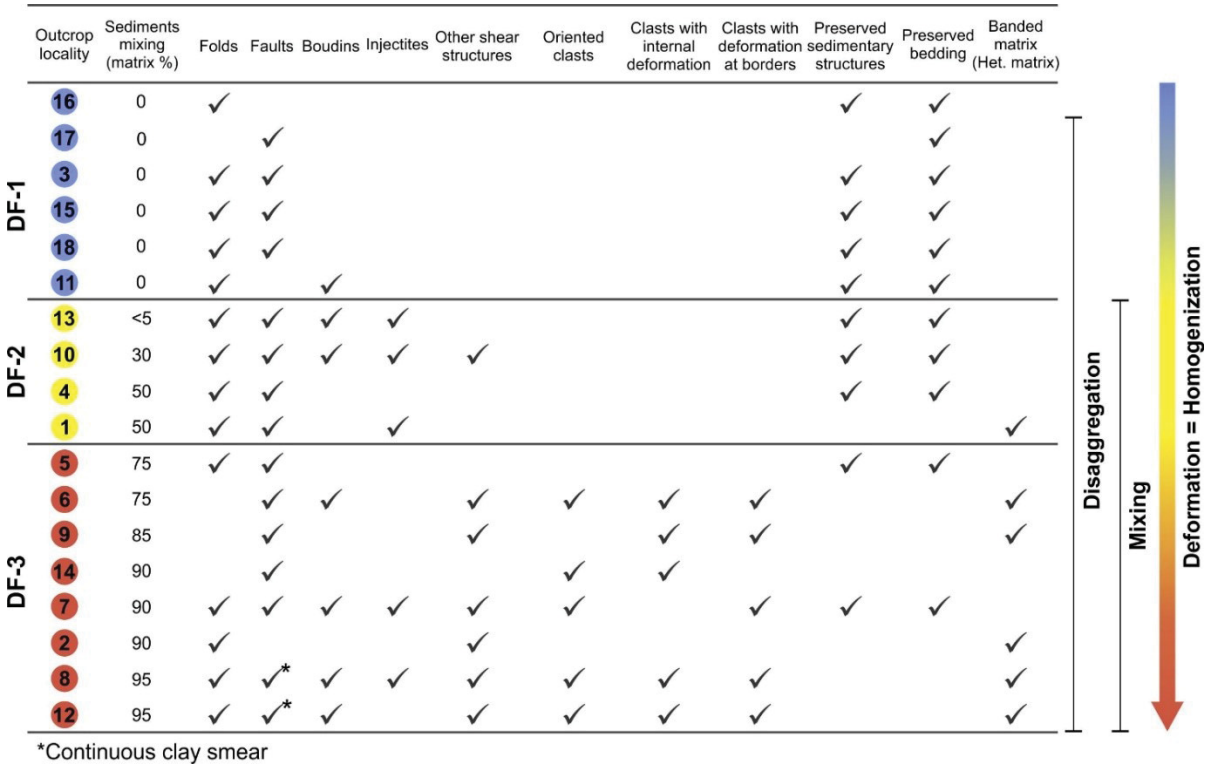

Fig. 3.12: Chart of structures identified in each outcrop locality (see Fig. 3.1) and compared with the respective amount of matrix. MTDs are divided into 3 deformational facies (DF) based on the amount of matrix and increase in disaggregation and mixing of sediments, which results in homogenization. Het. matrix means heterogeneous matrix.

3.5.1.1. Processes within deformational facies DF-1: incipient MTDs marked by a lack of matrix

The low diversity of deformational structures and the lack of matrix in DF-1 (Fig. 3.12, 3.13A) are interpreted as a result of poorly evolved or incipient mass flow with respect to disaggregation, mixing and homogenization. Despite these common characteristics between MTDs grouped in DF-1, the nature of some structures is variable, which may represent the different processes and stages of deformation during flow initiation. The occurrence of both gentle to open folds (Fig. 3.4A) and closed to tight recumbent folds (Fig. 3.4B) indicates flow interruption during different stages of shear strain accumulation, where the latter would suggest a more advanced stage than the former (e.g., Alsop and Marco, 2011).

Kink-band folds like those described in partially deformed mud-rich rhythmite (Fig. 3.4D) are, in tectonic settings, associated with deformation of laminated and anisotropic rocks under low temperatures and shortening parallel to bedding (Fossen, 2016). The geometry of kink bands is associated either with high mechanical anisotropy such as alternation of competent and incompetent layers (Fossen, 2016). These characteristics can also occur in shale or rhythmite, where low pore fluid pressure and some lithification or compaction would prevent a more ductile behaviour (Maltman, 1994). This seems to be corroborated by the local occurrence of broken bands and some associated faulting in DF-1.

In locality 11, recumbent folds with thickened fold hinges (Fig. 3.4B) are associated with parasitic folds in sandstone layers with no thickened hinge (Fig. 3.4F). Fold hinge thickening in these thin-bedded rhythmites can be associated with sand liquefaction and mobility due to the presence of overpressurized pore fluid contained in layers confined between mudstones (Waldron and Gagnon, 2011). Despite the evidence for sediment mobility, symmetric boudins in fold limbs, which result from extension parallel to fold limbs, and parasitic folds, suggest some viscosity contrast within this same MTD (e.g., Fossen 2016). The model of Treagus and Fletcher (2009) also suggests that viscosity contrast allows the thin competent layers to develop parasitic folds. In our case study the sandy beds acted as relatively competent layers as indicated by the occurrence of parasitic folds and symmetric boudins.

The rhythmite diapirs and their internal folds (Fig. 3.1 - locality 3, and Fig. 3.4F) show preferential vergence that agrees with paleocurrents from overlying cross-stratified sandstone (Vesely and Assine, 2006). These structures were interpreted as a result of mud diapirism due to sediment overloading (e.g., Collinson, 1994; Morley and Guerin, 1996; Morgues et al., 2009) associated with some shear due to slope instability (incipient mass flow), probably triggered by rapid sedimentation. Some studies suggest that overpressured shale becomes mobile and deforms under low stresses, producing diapirs and mud volcanoes (e.g., Deville et al., 2006; Morley and Guerin, 1996; Van Rensbergen and Morley, 2000, 2003).

In some cases, faulting seems to be a secondary process of deformation associated with folding in DF-1 (along the axial surface of folds or drag folds; localities 3 and 15, respectively). While in other cases, faults postdate folds (locality 18) or are the only deformation record (locality 17). Although no mixing processes occur in DF-1,

some disaggregation processes were promoted mainly by faulting and, secondarily, by boudinage resulting in disruption of layers, at least at the bedding scale.

3.5.1.2. Processes within deformational facies DF-2: mature MTDs marked by limited (<50%) matrix

Deformation within DF-2 is associated with mature mass flows that show increasing mass disaggregation and sediment mixing linked to the presence of preserved early deformational structures, bedding and primary sedimentary structures (Fig. 3.12 and 3.13A). Folds within DF-2 show different types of geometry even in the same outcrop locality. Folds may show thickening of hinges due to liquefaction related to pore-fluid overpressure of sandy layers, which, together with the general rounded shape of fold hinges is considered as indicative of plastic behaviour (Waldron and Gagnon, 2011). The complexity of folds seems to be related to variable shear-strain accumulation, which is indicated by the presence of open to tight and upright to recumbent folds.

Intense folding with associated boudinage of folds limbs in an interval of rhythmic sediments resulted in symmetric boudins (Fig. 3.1 – locality 13; Fig. 3.8A) and broken folds (Fig. 3.8A) of sandstone layers (competent layers) hosted in mudstone (incompetent layers). These differ from the symmetric boudins described in DF-1, as the mudstone layers here show no preservation of lamination in the highly deformed interval, and preserved lamination in the slightly deformed interval of the same MTD (locality 13). The intense deformation destroyed original lamination and the liquefaction of finer-grained layers allowed the filling of spaces created between boudin blocks (e.g., Odonne et al., 2011; Sobiesiak et al., 2017) and even the accumulation of mud in pods between the broken folds (Fig. 3.8A). Consequently, this resulted in the local development of muddy matrix (proto-matrix; Ogata et al., 2012a) due to mixing of mud from different layers that were previously separated by sandy layers. Contrary to symmetric boudinage associated with folding, asymmetric boudinage (Fig. 3.8C) seems to be inefficient in disrupting layers (Fig. 3.8A), as mudstone blocks forming asymmetric boudins (Fig. 3.8C) are still connected and no mixing of sandy sediments is observed.

Besides boudinage, faulting also promoted disaggregation through disruption of beds and laminae (Fig. 3.6B and H). When associated with smearing of sand and clay, grain-scale disaggregation, without grain deformation, also seems to be a potential

mechanism of sediment mixing (Fig. 3.6B and H). Bed-parallel shearing, which may form quarter-like structures (Fig. 3.11A), also contributed to grain-scale disaggregation and mixing. Within some DF-2 MTDs, relicts of sheared sandy laminations (locality 10) and faults (locality 4) show that disruption and mixing of sediments by shearing was an efficient mixing process (e.g., Ogata et al., 2012a). The banded matrix in locality 1 is interpreted as a relict of primary bedding, where the lack of primary sedimentary structures and the discrete contact between bands are possibly a result of sediment liquefaction and shearing (Fig. 3.4C). The increase in pore-fluid pressure also results in loss of grain cohesion (e.g. Allen, 1982; Maltman, 1994a; Martinsen, 1994; Nichols, 1995), allowing disaggregation and mixing as also observed in the muddy matrix of a folded and boudinaged interval in locality 13 (Fig. 3.8A).

In most DF-2 MTDs where early deformational structures, bedding and primary sedimentary structures are preserved we verified that boudinage, faulting and shearing parallel to layers tend to be non-pervasive (localities 4, 10 and 13). As these are the main processes of sediment disaggregation and mixing, this may explain the occurrence of matrix in localized horizons or pods. This partial generation of matrix may be a result of gradual disaggregation and mixing associated with a local increase of progressive deformation. During the early stages of internal slide deformation, Ogata et al. (2012a) described matrix occurring as “patches” or “pockets” and comprising matrix of different generations, which tend to form preferentially within shear zones that are focussed at the base and, secondarily, internally within the MTDs (Ogata et al., 2014a). According to these authors, this matrix has the same composition as the surrounding blocks, which suggests it is the result of progressive disarticulation of un-lithified sediment from these blocks. It is interesting to note that matrix generation in DF-2 occurs preferentially within rhythmite or mud-rich layers, which would indicate some influence of lithology in the deformation that produces matrix in our case study. The location of matrix in DF-2 may also be related to internal or basal shear zones, whose occurrence and propagation may also have some lithological control.

Injected sands are common in DF-2 (Fig. 3.12). However, the parental unit was identified in only one case (locality 10), which consists of deformed sandstone layers of a rhythmite body within the MTD. These injectites are interpreted as being contemporaneous to mass flow as they cut and are deformed by MTD structures. For the other injectite localities in DF-2, the parental rock can be either a non-exposed underlying sandstone bed or sandstone from remobilized intrabasinal clasts. The

fluidization of some sand layers, whether they are layers below or inside the MTD, are interpreted as a result of pore-fluid overpressure due to deformation (e.g., Farrell and Eaton, 1988; Sobiesiak et al., 2017; Strachan, 2008; Strachan and Alsop, 2006).

3.5.1.3. Processes within deformational facies DF-3: evolved MTDs marked by abundant (>50%) matrix

The most evolved MTDs of DF-3 comprise a high matrix content (>50%) and the greatest variety of deformational structures (Fig. 3.12 and 3.13A). These structures are recorded at clast margins, in the matrix and inside the intrabasinal clasts (sandstone and rhythmites), where they deform the whole clast and, in some cases, the surrounding matrix. Usually, clasts and matrix show similar composition (e.g., silty-clayey diamictite with clasts of rhythmite, or alternatively, sandy-muddy diamictite with clasts of sandstone and rhythmite). Clasts typically show increasing disaggregation towards their periphery where clast material is being incorporated into the matrix (Fig. 3.10D-H). Deformation inside intrabasinal clasts is similar to that recorded in DF-1 and DF-2 (Fig. 3.10B, C and E), which leads us to interpret this internal deformation as forming during earlier stages and that the intrabasinal clasts are remnants of the protolith that survived during the process of mixing and homogenization. Even the original sedimentary structures may be well preserved in sandstone blocks within some highly evolved DF-3 MTDs. This probably reflects contrasting composition and different rheology (e.g., different degrees of lithification, plasticity, permeability, water content etc.; e.g., Festa et al., 2012) and suggests that some parts of the original sediment are disaggregated and mixed earlier than others.

Intrabasinal clasts without internal deformation may be the result of incorporation of more lithified (deeply buried) layers (e.g., Sobiesiak et al., 2018) or simply portions of the MTD that were not deformed because of a non-uniform distribution of stress in the flow (survival clasts). These clasts also show deformation at their margins, which indicates some degree of incorporation into the matrix (e.g. Sobiesiak et al., 2016, 2017). The way margins are deformed, in fragments or grain by grain, seems to be more related to material properties. Seismic-scale studies (e.g., Alves and Cartwright, 2009; Bull et al., 2009; Gee et al., 1999) demonstrate that the size and number of allochthonous blocks generally reduce in the downflow direction. Observations in DF-3 suggest that marginal deformation (Fig. 3.10D to H), faulting (Fig. 3.6D and 3.8D) and boudinage of intrabasinal clasts (Fig. 3.8B and D) are the

processes by which clasts become progressively smaller (e.g. Sobiesiak et al., 2017). This seems to corroborate the idea of continuum deformation with disaggregation and mixing of sediments from intrabasinal clasts during the flow (Fig. 3.13A and B).

Despite the greater percentage of matrix in DF-3, the highly variable characteristics of matrix from heterogeneous (from banded to massive in the same MTD outcrop) to homogeneous (massive) seem to not necessarily be related to the amount of matrix. The amount of matrix in DF-3 may be linked to the degree of disaggregation, while the homogeneity may represent the degree of mixing. Therefore, if the disaggregation processes are more efficient, while the mixing processes are more limited or concentrated, then a heterogeneous matrix may result. If disaggregation and mixing of sediments within the MTD tend to be gradual, parts that were earlier disaggregated and mixed will also tend to be more homogeneous. In MTDs with local banded matrix (e.g., locality 6; Fig. 3.1, 3.11G and 3.11H), band disaggregation by faulting and layer-parallel shearing and mixing by layer-parallel shearing were observed (e.g. Ogata et al., 2012a; Sobiesiak et al., 2016). This suggests that with progressive disaggregation and mixing, these banded portions of matrix could be homogenised, reinforcing the idea of gradual matrix generation. The mixing by shearing processes is also indicated by the progressive shearing of fragments ripped-off sedimentary clasts.

The infilling of space between boudinaged blocks by matrix (Fig. 3.8B) and some injection of matrix in clasts suggest liquefaction to fluidization of matrix due to pore-fluid overpressure, in some way similar to the previously described behaviour for matrix (e.g., Festa et al., 2016; Odonne et al., 2011; Ogata et al., 2012a, 2014a; Sobiesiak et al., 2017). These features indicate a highly mobile mixture of sediment and water related to overpressured conditions (Ogata et al., 2012a, 2014a), which combined with shearing, may be the main process for mixing of sediments. The liquefication of sediments associated to shearing in MTDs is described by Ogata et al. (2014a) to occur mainly in shear zones at the base, which can propagate to internal portions, and, secondarily, internal shear zones. The authors also indicate the importance of liquefication, fluidization and soft-sediment deformation in the internal structural evolution of MTDs. In DF-3, it is not clear how the liquefication of matrix associated with shearing is distributed, with some cases associated with basal shear zones while others are along internal shear zones.

In DF-3, the parental unit for one sand injectite occurrence (locality 7) was identified and consists of a deformed sandy layer within the MTD; while for the other occurrence (locality 8) no parental unit was observed, and could be either an underlaying sandstone bed or an unexposed sandstone bed within MTD. The injectites of locality 7 were interpreted to be the result of either syn- or post-depositional pore fluid overpressure of sand layers isolated within a mud-rich matrix (e.g. Callot et al. 2008; Farrell and Eaton, 1988; Sobiesiak et al. 2017; Strachan and Alsop, 2006; Strachan, 2008).

3.5.2. The role of deformation in mass-flow transformation

Flow transformation processes in gravity flows have been widely discussed in the literature (e.g., Dasgupta, 2003; Fisher, 1983; Haughton et al., 2003; Morgenstern, 1967; Mutti et al., 2006; Piper et al., 1999; Strachan, 2008; Talling et al., 2012) but the role of deformation in the downslope evolution of mass flows is still poorly explored. The general idea for the evolution of mass-transport deposits is that the flow evolves from poorly-deformed to highly-deformed, to create homogenized sediment as a result of progressive deformation, disaggregation and mixing (e.g., Dasgupta, 2003; Eyles and Eyles, 2000; López-Gamundí, 1993; Martinsen, 1994; Mutti et al., 2006; Nemec, 1990) through flow transformation (e.g. Fisher, 1983; Dasgupta, 2003; Lopéz-Gamundí, 1993; Strachan, 2008). The matrix is considered as the final product of a continuum process that leads to progressive disaggregation and mixing of sediments (Ogata et al., 2012a).

According to Strachan (2008), the transformation of slumps into debris flows and turbidity currents result from multiple transformation mechanisms, associated with body, surface and fluidization transformation processes (Fisher, 1983) and linked to slump behaviour and evolution. Previously, other studies suggested two modes of flow transformation: 1) disaggregation or break-up in the flow (e.g. Schwarz, 1982; López-Gamundí, 1993; Lowe and Guy, 2000; Mohrig and Marr, 2003; Piper et al., 1999); and 2) shear-induced mixing and dilution of the flow surface with an ambient fluid (Morgenstern, 1967; Dasgupta, 2003; Van Der Knapp and Eijpe, 1968). Our results on the relationship between deformation and matrix generation (disaggregation and mixing) suggest that both mechanisms participate in flow transformation. However, most previous studies (including some recent papers such as Fallgatter et al., 2017

and Talling et al., 2012) have focused mainly on the transformation of mass flows (or debris flows) into turbidite currents rather than transformations during the mass flow. Flow transformations during mass flows, which are comparable to our study, have been described, for instance, by López-Gamundí (1993) and Strachan (2008).

From the flow transformation processes identified by Strachan (2008), those related to transformation between slump to debris flow consist of body and fluidization transformation (based on Fisher, 1983). The term body transformation was used originally by Fisher (1983) to describe flow changes between laminar and turbulent behaviours within the body of a flow without significant addition or loss of interstitial fluid, while Strachan (2008) used body transformation to explain local disaggregation of beds in the mass flow without significant addition or loss of interstitial fluid. In our study, body transformation can be associated with processes that promoted disaggregation, such as faulting, boudinage and shearing (layer-parallel, clast margin or matrix) as noted in the different deformational facies described. The role of boudinage in disruption of layers in MTDs was emphasized by Lopéz-Gamundí (1993), Festa et al. (2012) and Sobiesiak et al. (2016, 2017). We also attach a particular importance to boudinage (mainly symmetric) in the deformation and homogenization evolution of MTDs, as they promote disaggregation of beds and allow the interaction and mixing between sediments of previously disconnected layers (incompetent layers). This is combined with loss of grain cohesion due to sediment liquefaction in DF-1 and liquefaction of matrix infilling the space between boudins blocks in DF-3 (e.g. Odonne et al., 2011; Ogata et al. 2012a, Sobiesiak et al. 2017). Other disaggregation processes such as fracturing and brecciation (e.g. Callot et al., 2008; Martín-Merino et al., 2014; Ogata et al., 2012a) and clast disaggregation through collision with other debris during transport (Brooks et al., 2018) were not clearly identified in our case study. However, “grooves/stretch marks” in intrabasinal clasts may be generated by abrasion of matrix with rigid extrabasinal clasts, while shearing in matrix between closely spaced clasts indicates some interaction between clasts. The processes of faulting, layer-parallel shearing (e.g. Ogata et al., 2012a; Sobiesiak et al., 2016), matrix shearing and shearing at clast margins (e.g. Sobiesiak et al., 2016, 2017) also promote mixing of the poorly- to unlithified sediments remobilized by mass flows (e.g., Alsop and Marco, 2014; Alves and Lourenço, 2010; Brooks et al., 2018; Festa et al., 2012; Fisher, 1983; Hodgson and Brooks, 2018; Martinsen, 1994; Nardin, 1979; Ogata et al., 2012a; Sobiesiak et al., 2016, 2017).

The term fluidization transformation was used by Fisher (1983) to designate the elutriation of particles by upward-moving fluids from a high-density bed to produce an overlying turbulent dilute phase. Based on that, Strachan (2008) applied fluidization transformation to explain fluidized sediment through intraslump dykes interpreted as being generated during or shortly after folding by the upward movement of pore fluids driven by local overpressure and fluidization. In our case study, we identified some evidence for local pore-fluid overpressure leading to liquefaction or fluidization of sediments, which includes muddy matrix in pods from incompetent layers, through boudinage associated with folding, infilling of space between symmetric boudins by matrix, injection of matrix in blocks and sand injectites generated within the mass flow from fluidization of internal sand layers (e.g. Callot et al., 2008; Farrell and Eaton, 1988; Odonne et al., 2011; Ogata et al. 2012a; Pini et al. 2012; Sobiesiak et al. 2017; Strachan, 2002, 2008). Sand injectites have been described as associated with MTDs in all stages of flow evolution (e.g. Callot et al., 2008; Farrell and Eaton, 1988; Strachan, 2002, 2008; Sobiesiak et al. 2017). In our case study, the presence of folded injectites (Fig. 3.9F) suggests an early to middle stage of intrusion, while other injected sands that cut the matrix and previously deformed beds indicate a late stage. The parental units of injectites may not be involved in the flow and consist of underlying sands that are mobilized by MTD-induced loading (e.g., Jonk, 2010; Strachan, 2002). Alternatively, the source of injectites may be internal sand layers or blocks within the MTD (e.g. Callot et al., 2008; Farrell and Eaton, 1988; Sobiesiak et al., 2017). The injectites formed from internal parental units reflect the poorly or unlithified character of the block sediment, together with an increase in pore-fluid pressure during mass-transport due to deformation of the sandy layers or blocks (e.g. Farrell and Eaton, 1988; Sobiesiak et al., 2017). It also suggests that water-saturated sand layers are confined within mud in order to prevent significant water escape before the build-up of overpressure necessary for sand fluidization (Maltman and Bolton, 2003).

Our results indicate that liquefaction and fluidization of matrix is another process that promotes mixing of sediments, mainly when combined with shearing. According to Ogata et al. (2016), structures of mass-transport deposits are the product of high strain and soft-sediment deformation of undrained, water-saturated, poorly- to unconsolidated sediments at low confining pressure (shallow depths). This behaviour is a result of the loose aspect of sediments in the matrix and its common high mobility due to pore fluid overpressure (e.g. Ogata et al., 2012a; Pini et al., 2012), which can

be indicated by shearing features in grain-scale (Fig. 3.11D and E) and fluidal features in the matrix (Fig. 3.10E and F). Deformation of sediments promotes a spatial rearrangement of grains, through granular flow (frictional sliding and grain rotation and translation; e.g. Fossen, 2016), and pore fluid pressure variation resulting in changes of shear strength and cohesion of sediments, where pore fluid overpressure results in sediment mobilization (liquefaction and fluidization), and therefore may lead to changes in the mechanical behaviour and type of deformation (e.g. Collinson, 1994; Farrell and Eaton, 1988; Gomez-Rivas and Griera, 2011; Maltman, 1994a,b,c; Maltman and Bolton, 2003; Murray, 1994; Strachan 2002; Terzaghi, 1962). According to Tripsanas et al. (2008), the flow transformation is controlled by the nature of the sediments (e.g. potential for liquefaction, shear strength) and the slope gradient

Some studies indicate that different lithologies may display different mechanical behaviours and therefore control styles of deformation (e.g. Alsop and Marco, 2011, 2013; Morley and Guerin, 1996; Noble and Dixon, 2011; Stewart and Clark, 1999; Rowen et al., 2004; Waldron and Gagnon, 2011). Deformation is also controlled by heterogeneity, that is the interaction between layers of different lithologies and different competences that are deformed together (e.g. Alsop and Marco, 2011, 2013; Noble and Dixon, 2011; Waldron and Gagnon, 2011). The mechanical behaviour of each lithology and the viscosity contrast between different lithologies also depends on the pore fluid pressure (e.g. Alsop and Marco, 2011, 2013; Collinson, 1994; Farrell and Eaton, 1988; Maltman, 1994a,b,c; Maltman and Bolton, 2003; Morley and Guerin, 1996; Murray, 1994; Strachan, 2002; Terzaghi, 1962; Waldron and Gagnon, 2011). According to Morley and Guerin (1996), the behaviour of shale changes with pore fluid pressure and compaction, where highly pressurized and undercompacted shale becomes mobile and deforms under low stresses, and moderately pressured or more compacted shale becomes more rigid developing frictional detachments. This behaviour has been also indicated by other studies (e.g. Briggs et al., 2006; Deville et al., 2006; Van Rensbergen and Morley, 2000, 2003). Time and space variations and change of mechanical behaviour of different lithologies related to pore-fluid overpressure may also occur within the deformed layers because of local overpressure or dewatering (e.g. Alsop and Marco, 2013; Strachan, 2002, 2008; Ogata et al. 2012a, 2016; Waldron and Gagnon, 2011). Some evidence of pore-fluid overpressure was identified in matrix or sand layers in some of the studied MTDs (DF-2 and DF-3). These include matrix mobilization resulting in accumulation or infilling of space between

symmetric boudin blocks and matrix and sand injection. In MTD of locality 13, for example, local liquefaction of mud layers generates a muddy matrix and are associated with boudinage and faulting that may indicate local high pore-fluid overpressure. In locality 10, liquefaction and fluidization of matrix associated with detachment surfaces and flexural folding of shale seem to indicate local variability of pore-fluid within the same deposit. Waldron and Gagnon (2011) suggest the liquefaction by pore-fluid overpressure of sand may result in sand layers becoming weaker than mud layers, which may explain some features described here, such as thickening of folds hinges and asymmetric boudinage of mud layers (competent layers) hosted in sand layers (incompetent layers). In addition to these observations, we verified a preferential production of matrix in rhythmites and mud-rich intervals within DF-2. The muddy composition of matrix and the preservation of sandy intrabasinal clasts in some DF-3 MTDs may indicate some influence of lithology in the process of homogenization.

Some studies have discussed the efficiency of flow transformation processes, which have been considered either inefficient with minimal transformation achievable (Dasgupta, 2003; Haughton et al., 2003) or efficient with *en masse* transformation (Morgenstern, 1967; Piper et al., 1999). Strachan (2008) studied the Little Manly Slump and suggested partial rather than *en masse* transformation from slump to debris flow, where the development of longitudinal and lateral flow partitioning of grains may be prevented by early “freezing” as the mass flows did not move far from their source. Our observations in the different deformational facies suggest that matrix generation through disaggregation and mixing is gradual and progressive, and so are the processes of flow transformation and homogenization. The records of different stages of deformation in MTDs indicated by deformational facies may depend on the moment of “freezing” of the mass flow and/or non-pervasive strain accumulation (related to the gradual/partial flow transformation; e.g. Strachan, 2008).

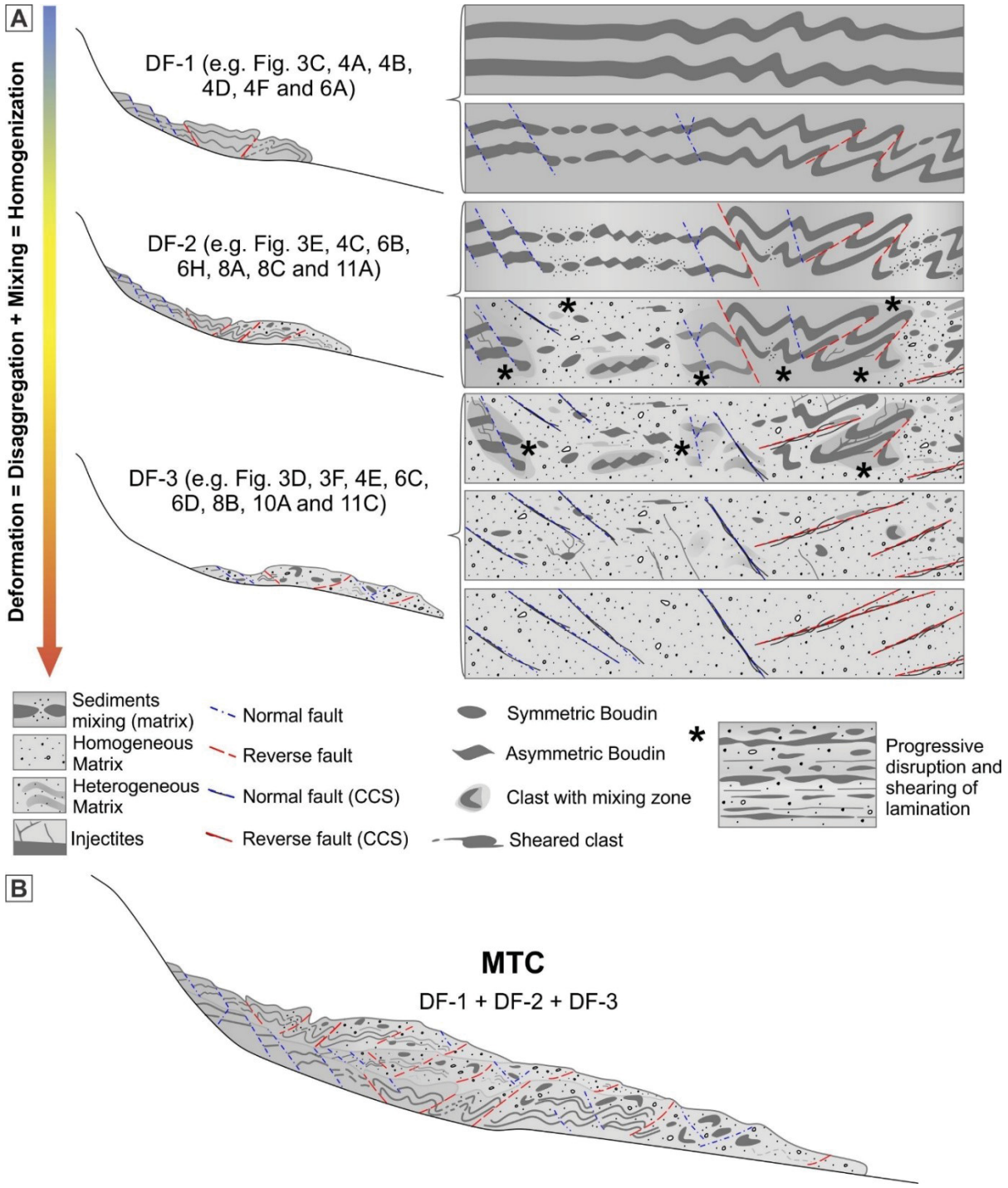

Fig. 3.13: A) Idealized model for MTD deformation evolution toward homogenization due to increase of disaggregation and mixing of poorly- to unlithified sediments. This is based on general models (e.g. Nemec, 1990; Ogata et al., 2012a; Festa et al., 2016) and field insights from structures and matrix relationship (deformational facies). DF-1 consists of less deformed and incipient stages of evolution with no matrix generation, which seems to be related to short-distance transport or preferential development at the proximal portions of MTDs. DF-2 correspond to the intermediate mature stage, where remobilized sediments are widely deformed and show matrix generation (up to 50%) associated with the presence of preserved early deformational structures, bedding and primary sedimentary structures. Main structures and processes of deformation are represented, with a schematic distribution along the MTD. CCS -

continuous clay smear. Progressive disruption and shearing of lamination based and modified from Ogata et al. (2012a, 2014b). B) Schematic drawing of a mass-transport complex generated by several mass flow events, with the record of different deformational facies and in which DF-1 and DF-2 tend to occur at proximal positions and DF-3 tends to occur in more distal positions.

3.6. CONCLUSIONS

The systematic analysis of deformation structures in MTDs exposed in the Paraná Basin allows us to shed some light on the role of deformation processes in sediment homogenization (disaggregation and mixing) and flow transformations within subaqueous mass flows.

- The amount of matrix and the assemblage of structures allows us to identify incipient, mature and evolved MTDs where deformational facies (DF1 to DF3) correspond to different stages of deformation and homogenization of mass flows.
- The disaggregation and mixing of sediments tend to be gradual as the mass flow evolves, together with mass-flow “freezing” at different stages or due to non-pervasive or non-uniform strain accumulation, allowing different stages of deformation and homogenization to be preserved.
- Within incipient MTDs (DF-1) deformation processes do not promote sediment mixing, but faulting and boudinage allow bed disaggregation. During mature stages (DF-2), disaggregation of beds take place by boudinage, faulting and layer-parallel shearing, while layer-parallel shearing, liquefaction/fluidization and some faulting promote mixing. In evolved MTDs (DF-3) disaggregation takes place by faulting, boudinage and marginal deformation of intrabasinal clasts, and layer-parallel shearing of banded matrix, while mixing derives from shearing and liquefaction/ fluidization.
- The production of matrix preferentially within mudstone layers and rhythmite suggests a control of lithology in disaggregation and mixing of sediments as previously described. However, further investigation is required to better understand the relationship between sediment composition, associated pore-fluid pressure and soft-sediment deformation in generating MTD matrix.

4. RESULTADOS – PARTE II: RELATIONSHIPS BETWEEN MASS-TRANSPORT KINEMATICS AND SEDIMENT DISPERSAL PATTERNS IN PALEOGEOGRAPHIC RECONSTRUCTION

Rodrigues, M.C.N.L.[1], Trzaskos B.[1], Vesely, F.F.[1], Mottin, T.E.[1], Schemiko, D.C.B.[1], Alsop, G.I.[2]

[1]Departamento de Geologia, Universidade Federal do Paraná

[2] Department of Geology and Petroleum Geology, School of Geosciences, University of Aberdeen

4.1. ABSTRACT

Deformation structures (mainly folds and faults) generated in remobilized sediments by submarine mass flows have been indicated as kinematic indicators of these flows and so the paleoslope orientation. The paleoslope azimuth integrated with other stratigraphic data can help in the interpretation of the depositional evolution and in the paleogeographical reconstruction of a basin. However, most studies have analysed MTDs structures and applied the paleoslope definition methods for well-exposed MTDs. This raise the issue about the validity of using MTDs structures for paleoslope definition in regions with limited exposure. To verify this were selected several MTDs of the Itararé Group of the Paraná Basin, in southern Brazil. Different structures were analysed through different methods and the datasets and transport direction results were evaluated to verify the robustness. The study allowed us to the define of the general orientation for paleoslope of Itararé Group in the different time interval within the studied area with some certainty, besides the limited exposure of the outcrops. Between the different structures analised, faults and folds show similar potential and are the main structures to define paleoslope, as expected. The use of other structures can be also important to clarify the kinematics of the mass flow, sometimes being the main indicators of the flow direction. The integration with paleocurrent data of associated deposits also indicates the potential of paleoslope definition through MTDs with limited exposure for paleogeographic reconstructions.

Keywords: mass-transport deposits; syn-sedimentary deformation; paleoslope; Itararé Group; Paraná Basin

4.2. INTRODUCTION

Mass-transport deposits (MTDs) derive from the collapse of subaqueous slopes and remobilization of rock and sediment via non-Newtonian gravity flows (e.g. Martinsen 1994; Posamentier and Martinsen, 2011). Deformation within MTDs is considered to reflect paleoslope orientation, once shear stresses originate from gravitational forces. This means that the kinematics of slides and slumps can be used to help interpreting detrital dispersal patterns in settings that are prone to slope instability like deepwater slopes and deltas. Deformation in MTDs can also be useful to interpret other aspects of sedimentary basins such as depositional environments (e.g. Martinsen, 1994; Strachan and Alsop, 2006; Bull et al., 2009; Posamentier and Martinsen, 2011; Alsop et al., 2016; Jablonská et al., 2016, 2018).

The definition of paleoslopes from structural analysis of MTDs may be complicated by sampling issues (e.g., scale of observation relative to the whole MTD and degree of exposure when dealing with outcrops) as well as factors that modify the original structure like rotation during the flow and overprinting by later tectonic deformation (Strachan and Alsop, 2006; Debacker et al., 2009; Waldron and Gagnon, 2011). In addition, factors like slope gradient, topography, changes in rheology and flow complexities may control the patterns of deformation in MTDs (e.g. Jones, 1939; Woodcock, 1979; Farrell, 1984; Martinsen, 1989; Strachan and Alsop, 2006). Some studies suggest that deformation in MTDs is chaotic and does not show consistent patterns (e.g. Davis and Reynolds, 1996; Van der Pluijm and Marshak, 2004). However, through careful and systematic structural analysis of several structures and using several techniques it is possible to identify coherent and meaningful patterns that allow understanding deformation processes and help reconstructing paleogeography (Strachan and Alsop, 2006; Debacker et al. 2009; Alsop and Marco, 2011; Sharman et al., 2015).

Several methods have been developed to deduce paleoslope direction from MTD structures through statistical analysis (see Debacker et al., 2009; Alsop and Marco, 2012; Sharman et al., 2015; and references therein) and the reliability of these methods have been also discussed (e.g. Lewis 1971; Woodcock, 1976a,b, 1979; Farrell, 1984; Maltman, 1984, 1994a,b; Bradley and Hanson, 1998; Debacker et al., 2001, 2009; Strachan and Alsop, 2006; Strachan, 2008; Alsop and Marco, 2011; Sharman et al., 2015). In this paper we test the accuracy of MTD structures as

paleoslope indicators through a systematic structural analysis of deformation records and comparison with a large database on fluvial/deltaic and turbidite palecurrents. The study is based on the examination of outcrops of late Paleozoic strata in the Paraná Basin (Itararé Group; southern Brazil), in which postdepositional tectonic overprint (mainly subvertical fractures) is easily discernible from MTD-related deformation.

4.3. GEOLOGICAL SETTING

The Paraná Basin consist of a large intracratonic basin (up to 1,600,000 km²) of polycyclic nature (Zalán et al., 1990) situated in southern South America. The basin display a NNE-SSW trending oval geometry and its current limits are erosive borders related to meso-cenozoic uplift in the South American continental margin (Milani et al., 2007). The stratigraphic-structural evolution of the Paraná Basin was controlled by NW-SE, NE-SW and subordinately E-W trends inherited from the heterogeneous basement, which comprise cratonic terrains and orogenic belts agglutinated during the Brasiliano orogenic cycle (Zalán et al., 1990). Sedimentation took place from Ordovician to early Cretaceous (Milani et al., 1994) and is divided in six second-order sequences bounded by inter-regional unconformities (Milani, 1997). The late Mississipian to Cisuralian Itararé Group is the lower half of the up to 2.5 km-thick Permo-carboniferous supersequence (e.g. Schneider et al., 1974; Zalán et al., 1990; França and Potter, 1991; Holz et al., 2010). The sediments of the Itararé Group were mostly accumulated in marginal to relatively deep marine environments during multiple stages of deglaciation associated with the late Paleozoic ice age in southwestern Gondwana (e.g., França and Potter, 1991; Vesely and Assine, 2006). França and Potter (1991) subdivided the Itararé Group into three basin-wide lithostratigraphic intervals (Fig. 4.1) classified as formations. These three units correspond roughly to the formations previously defined by Schneider et al. (1974) and can be correlated to the three palynozones defined by Souza (2006). The studied MTDs were positioned in these three wide time intervals, referred to as T1, T2 and T3 in the present paper (Fig. 4.1).

Several authors described penecontemporaneous deformational structures in the Itararé Group, which were, initially, interpreted mainly as glaciotectonic features associated with glacio-terrestrial deposition (e.g. Leinz, 1937; Almeida, 1948; Martin, 1961; Caetano-Chang, 1984; Canuto, 1985). However, subsequent research

associated most of these structures with subaqueous mass movements, which is corroborated by their association with turbidites, marine black shale and other types of gravity-flow deposits (e.g. Sanford and Lange, 1960; Salamuni et al., 1966; Rocha Campos, 1967; Schneider et al. 1974; França and Potter, 1991; Gama Jr. et al., 1992; Eyles et al., 1993; França et al., 1996; Carneiro and Costa, 2003; Vesely and Assine, 2006; Suss et al., 2014; Fallgatter and Paim, 2017; Carvalho and Vesely, 2017; Valdez et al., 2017; Mottin et al., 2018). These MTDs are identified throughout the succession of the Itararé Group and consist mostly of heterogeneous to homogeneous diamictites (gravely-sandy mudstones), deformed sandstones and mudstones, and large allochthonous intrabasinal clasts.

After the deposition of Itararé Group, the Paraná Basin passed through several tectonic events as a result of reactivation of ancient basement faults by tension associated with the active margin of the South American Plate, and opening of the Atlantic Ocean (e.g. Zalán et al., 1990; Soares, 1991; Milani, 1997, 2004). The Paraná basin eastern flank, where this study is situated, was affected by fracturing and basic magmatism during the opening of the South Atlantic and subsequent evolution of the South American margin (Milani and Zalán, 1999). The post-deposition deformation in the Itararé Group is, generally, easy to distinguish from mass-transport deformation, once it displays brittle structures that crosscut several layers and deposits and are related with regional (e.g. Rostirolla et al., 2000, 2002, 2003; Trzaskos et al., 2006).

The deposition of MTDs in recent studies of Itararé Group have been associated with instabilities caused by high sedimentation rates linked with deglaciation (e.g. Suss et al., 2014; Carvalho and Vesely, 2017; Fallgatter and Paim, 2017; Valdez et al., 2017; Mottin et al., 2018) or rapid base-level fall due to isostatic rebound (Mottin et al., 2018). The patterns of sediment dispersal in the Itararé Group is relatively well known because of several recent papers dedicated to reconstruct the paleogeography of the Paraná Basin at that time. These studies produced a huge amount of paleocurrent, paleo-ice flow and detrital provenance data (e.g. França et al., 1996; Gesicki et al., 2002; Vesely and Assine, 2006; Suss et al., 2014; Carvalho and Vesely, 2017; Fallgatter and Paim, 2017; Mottin et al., 2018). In general terms, a sediment transport to the NNW prevailed during T1 and T2, with local variations to the W and NE. This tendency changed during T3, with paleocurrents turning to the SW in the central-northern sector of the basin while in the south a more complex pattern started to

operate feeding sediment centripetally to a subsiding area known as the “Rio do Sul” sub-basin (e.g., Castro, 1991).

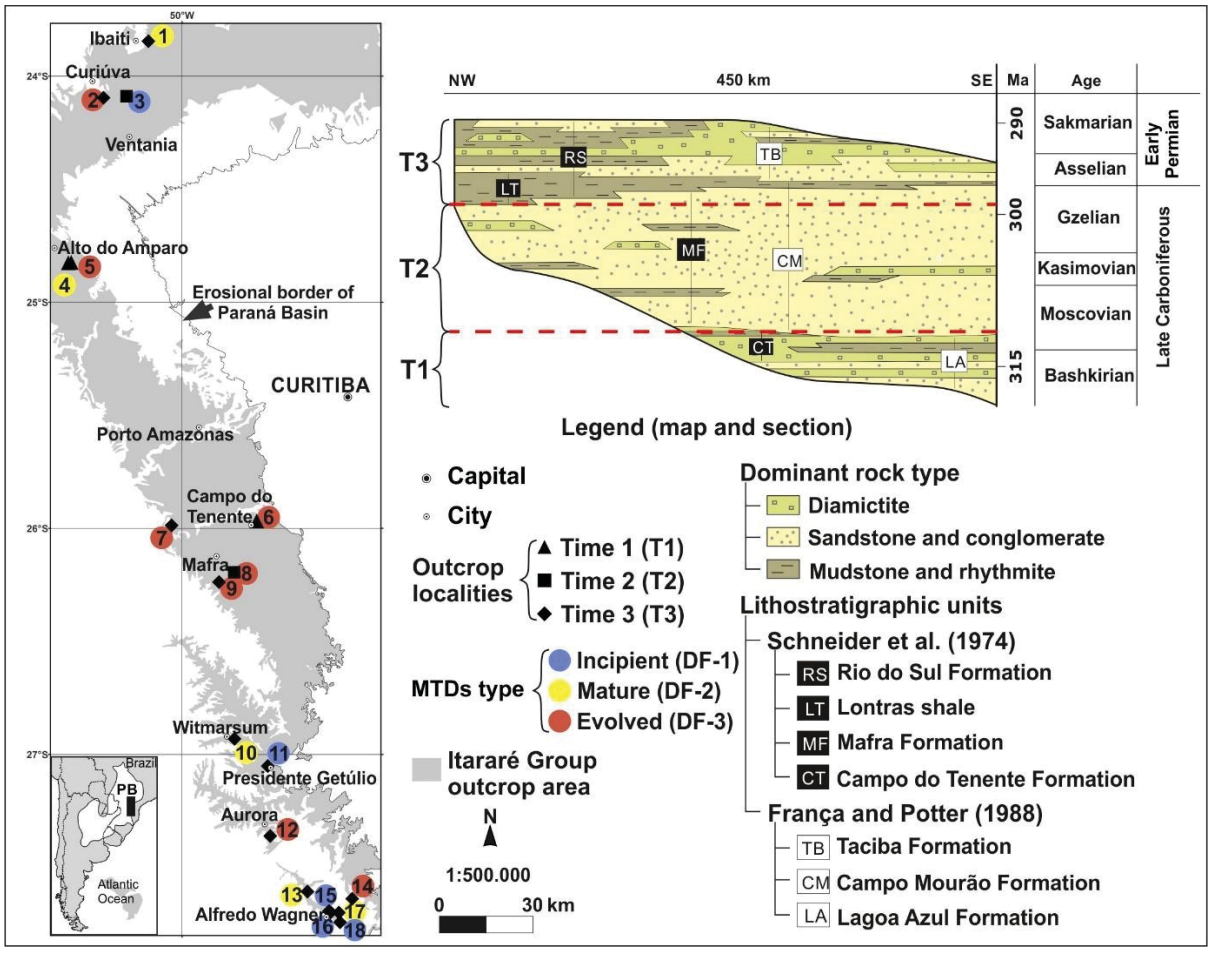

Fig. 4.1: Location map and stratigraphic setting of the study area in the Paraná Basin in the southern of Brazil. The geographic location, stratigraphic position and type of deformation facies of each examined mass-transport deposit are indicated by numbers and symbols respectively.

4.4. METHODS

The present research was conducted in the eastern belt of the Itararé Group in southern Brazil (Fig. 4.1), where outcrops present a wide variety of MTD-related facies and structures. The studied MTDs occur at different stratigraphic levels within the ~1.3 km thick Itararé Group and were positioned in the three time intervals T1, T2 and T3 (Fig. 4.1) based on the location of outcrops in previously published regional geological maps and cross-sections. As the Itararé Group also present some deposits deformed by glaciotectonics (e.g., Aquino et al., 2016; Rosa et al., 2019), the selection of localities for this studied took into account that the localities show no evidence of direct influence of ice sheets, such as subglacial striation/grooves and glacial deposits

(subglacial tillite), but evidence of proglacial marine deposits (e.g., Carvalho and Vesely, 2017; Mottin et al. 2018; Schemiko, 2018).

The study involved field work with description of MTDs in terms of facies composition, bounding relationships with other facies, deformational products as well as spatial and temporal relationships between different deformational products, whenever possible. Field work also included collection of structures orientation data, such as fold geometries (hinge trends, plunge, limb orientations, vergence and facing), fault orientation and kinematics, orientation of slickelines, bedding and banded matrix orientation, asymmetric boudins geometries (axis, faults and kinematics), injectites orientation, orientation of major axis of oriented intrabasinal and extrabasinal clasts, orientation of grooves and stretch marks at intrabasinal clasts borders, and kinematics of several features (quarter structures, sigma structures, shearing at intrabasinal clasts borders, and others). Though some fold orientations were measured directly in the field, most hinge orientation (line of intersection of folds limbs or in few cases β or π axis), axial plane orientation (the plane that bisects the fold limbs), fold facing orientation (Holdsworth, 1988) and interlimb angle were calculated stereographically from field information. For this was used softwares as Stereo32 1.0.3 (Röller and Trepmann, 2003) and Stereonet 10 (Allmendinger, 2011).

In order to better describe some structures geometry, samples were collected to produce polished slabs. Beside classical classification for faults, boudins (Goscombe et al., 2004) and folds (e.g. Fleuty, 1964; Ramsay, 1967; for more information see Twiss and Moores, 2007; Fossen, 2016), the flow perturbation fold model (e.g. Holdsworth, 1990; Alsop and Holdsworth, 1993, 2004) was applied. This model considers that layer-parallel shear folds (LPS) are generated by velocity gradients in the downslope direction and layer-normal shear folds (LNS) are generated by velocity gradients along strike (Alsop and Marco, 2011). Some structures were named based on their geometric similarities (e.g. Ogata et al., 2016) with structures typically observed in ductile shear zones in metamorphic rocks, which are a descriptive and non-genetic terminology used in structural geology (e.g. Passchier and Trouw 2005).

Stereographic projection of the structural data was applied to define the geometry of some structures, such as folds, to evaluate statistically the data quality and to apply methods of paleoslope definition. The evaluation of the structures datasets considered as parameters the number of measures, the preferential

orientation (Woodcock and Naylor, 1983) based on the strength parameter C (Woodcock, 1977) and confidence interval of 95%, for which were given classification values (see Appendix 1). The final classification of each structure dataset was obtained from the mode or mean of classification values of the cited parameters. The mean was used when no clear mode was defined. To evaluate transport direction through each kind of structure were considered as parameters the number of methods applied, the confidence interval (95%) of the average transport direction defined from the transport directions obtained from the methods applied and the final classification of structures datasets (see Appendix 2). For structures datasets analysed through two or more methods of paleoslope definition, it was calculated an average transport direction with the purpose of obtain the variation of confidence interval (95%) related to paleoslope definition, and their robustness for paleoslope definition (Appendix 2). For structures datasets analysed using just one method of paleoslope definition was used the confidence interval (95%). For these parameters were also given classification values (see Appendix 2) from which were also obtained the final classification for paleoslope definition by structure through the mode or mean. The evaluation of the final transport direction (or paleoflow, that correspond to the paleoslope) for each outcrop considered the evaluation of structures datasets (Appendix 1), transport direction by structure (Appendix 2), the total number of methods applied by outcrop (NM in Appendix 2) and confidence of interval (95%) of the final transport direction with the respective classification value (Appendix 2). The values used for classification (cv) represent the degrees of robustness of the evaluated parameters, structures datasets, structures transport direction and the final transport direction (more details in the Appendixes 1 and 2). The degrees of robustness consist of: a) no robustness (cv = 0); b) very weak robustness (cv = 1); c) weak robustness (cv = 2); d) moderate robustness (cv = 3); e) strong robustness (cv = 4); f) very strong robustness (cv ≥ 5).

The strength parameter C values were obtained through the software Stereo32 for data set with 5 or more measures, which is calculated from eigenvalues defined through Bingham distribution (C = ln (eigenvalue 1/eigenvalue 3); Woodcock, 1977). While the preferential orientation of each data cluster was defined from the strength parameter C (based on Woodcock and Naylor, 1983), which is considered here as none for C ≤ 1, weak when 1 > C ≤ 3, moderate when 3 > C ≤ 6 and strong for C > 6. The transport direction obtained from each method applied for faults, folds (hinge, axial plane and facing), injectites and asymmetric boudins (axis and faults) were defined

using the mean vector calculated through the softwares Stereo32 and Stereonet 10, which calculate through Fisher Vector Distribution (standard mean vector calculation). The confidence interval (95%) for structures datasets, average transport direction from methods applied for each structure and final transport direction for each outcrop was obtained through the Software Stereo32. The confidence interval (95%) is the semi-apical angle of confidence cone for a given confidence level calculated based on the Fisher Vector Distribution (Woodcock and Naylor, 1983). Other structures, as intrabasinal and extrabasinal clasts oriented, slickenlines of intrastratal detachment surfaces and grooves/stretch marks in intrabasinal clasts, were plotted in rose diagrams as axes and the transport direction was obtained through Von Mises distribution using the software Stereonet 10 (Allmendinger et al., 2013; Cardozo and Allmendinger, 2013), with respective confidence interval (95%).

To the definition of paleoflow one or more methods were applied for each kind of structure. For folds at least one method was applied for each element (hinge, axial plane and facing), such as mean axis method (MAM), downslope average axis method (DAM), separation arc method (SAM), mean axial plane strike method (MAPS), mean axial-planar dip method (MAD), axial-planar intersection method (AIM) and fold facing direction (FFD), which are methods widely applied in paleoslope studies (see Alsop and Marco 2012 and references therein).

Faults and faults in asymmetric boudins were treated through the application of the mean fault orientation method (MFOM) and fault intersection method (FIM) (see Debacker et al., 2009). The mean orientation of slickenlines (SM) associated with faults is a complementary method suggested in this research for faults. For boudins axis we considered its orientation in relation to other features and so to the flow direction (parallel or normal; Festa et al., 2013). Mean orientation of slickenlines of intrastratal detachment surfaces, major axis of oriented extrabasinal and intrabasinal clasts (based on Sobiesiak et al. 2016) and grooves/stretch marks at intrabasinal clasts (based on Ogata et al. 2014) have been also used to define mass-transport direction. The orientation of injectites was also considered, however with caution and considering its orientation in relation to other structures such as faults and folds. To the preferential orientation of bedding and banding in heterogeneous matrix we used the mean bedding strike method (MBSM) suggested by Sharman et al. (2015).

An average transport direction and respective confidence interval (95%) were obtained for each locality studied through analysis using Fisher Vector Distribution of

all transport direction defined by methods of paleoslope definition applied. In a few cases were defined two possible transport direction due to the occurrence of two possible interpretations for some structures. The average transport directions were considered to be the paleoflow direction in the correspondent location. The kinematics indicated by folds vergence, faults, quarter structures, shearing at intrabasinal clasts and SC-like structures, were also considered as paleoflow indicators.

Paleocurrent data were used to compare the directions of sediment dispersion with MTD kinematics using data from the literature. These included dip azimuth of cross-stratification in stream-related fluvial or fluvio-deltaic facies located in undeformed (not remobilized) strata stratigraphically below and above the MTDs. The orientation of current ripples and flute casts in turbidite were also used to compare to MTDs paleoflow. The paleocurrent data consist of data published by several studies developed in the study area (Vesely and Assine 2006, Suss et al. 2014; Fallgater, 2015; Juk, 2016; Carvalho and Vesely 2017; Fallgatter and Paim, 2017; Mottin et al., 2018; Schemiko, 2018). The final classification for each paleoflow (final transport direction) calculated were also considered to compare the results between themselves and with the paleoccurents, once represent the robustness of the paleoflows.

4.5. GENERAL CHARACTERISTICS OF MTDS

Most of the MTDs studied are developed in T3 (Fig. 4.1), which correspond to the earliest Permian Rio do Sul (Schneider et al., 1974) and Taciba (França and Potter, 1991) formations, although subaqueous landslides were recurrent during the deposition of the Itararé Group (Vesely et al., 2018), recorded in all T1 to T3 time-intervals. Consequently, the best exposures are located in the southern sector of the studied area where one main MTD complex, about 100 m thick, can be mapped in the upper half of the Rio do Sul Formation. The limits and thickness of a single MTD are usually difficult to access due to limited exposure of Itararé Group. The thickness of the studied MTDs, usually, ranges from about 5 m to 10s of meters (Carvalho and Vesely, 2017; Mottin et al., 2018; Schemiko, 2018). When exposed, boundaries between MTD and non-MTD strata are sharp, with the base of MTDs usually being erosive and irregular. The top surfaces of MTDs, when identified, are generally flat but low amplitude relief is reported locally, onto which fine-grained facies may be ponded.

The MTDs consist of 1) large intrabasinal clasts (IC) of sandstone and rhythmites (Fig. 4.3A-D), 2) deformed sandstone, rhythmite and shale, and 3) heterogeneous (banded matrix) to homogeneous (massive matrix), sandy-muddy diamictites with dispersed granules to boulders of intrabasinal (sandstones, shale, rhythmites and plant fragments) and extrabasinal (granites and metamorphic rocks) clasts, some of them striated and faceted. One or more type of deformational structures was identified in all 18 localities studied, such as folds, faults, boudins and others, and may also show allochthonous intrabasinal clasts and poorly-sorted matrix. Both extensional and compressional structural styles are identified in the same exposure and in equivalent proportions. The temporal relationship between structures is usually hard to determine because intersection is rare. However, folds tend to predate structures such as faults and boudins, once they are sometimes deformed by these structures. All structures studied consist of occurrences limited to the MTD and interpreted as generated by mass flow events.

The studied MTDs were grouped into three main deformational facies (incipiente, mature and evolved; Fig. 4.1 and Table 4.1) based on the relative proportion of coherent intrabasinal clasts and matrix, and on the linkage between different structures (see Paper 1 – Rodrigues et al. 2019 submitted). These deformational facies do not seem to have a stratigraphic relationship as they are found in different time intervals, which indicate different degrees of homogenization of sediments (disaggregation and mixing) associated to several deformation processes.

Table 4.1: Deformational facies defined based on matrix proportion, intrabasinal clasts and deformation structures identified in the localities studied.

Deformational facies (MTD type)	Characteristics	Matrix (%)	Outcrop localities
DF-1 (Incipient MTDs)	Display a lack of matrix, well preserved bedding with sedimentary structures. Deformational structures incluede faults (normal or reverse) and folds, and sometimes symmetric boudins occurring along fold limbs (locality 11). Particular kinds of folds include monoclinal folds, diapiric folds, parasitic folds and kink band folds (localities 16, 3, 11 and 18 respectively).	0	3; 11; 15; 16; 17; 18
DF-2 (Mature MTD)	Display banded (locality 1) or homogeneous (localities 4, 10, 13 and 17) matrix, which occur as pods in the vicinity of intrabasinal clasts. Deformational structures include folds, faults, symmetric and asymmetric boudins, injectites, and other shear structures such as quarter-like structures.	<5 - 50	1; 4; 10; 13
DF-3 (Evolved MTD)	Heterogeneous diamictite, with disrupted and highly deformed intrabasinal clasts with sedimentary bedding partially preserved (localities 5, 7 and 9), to almost homogenized diamictites (locality 6). Matrix is banded to homogeneous. The remnants of bedding or banded matrix record deformational structures such as folds, faults, boudins and other shear-related structures. Other records of deformation orientation of extrabasinal and intrabasinal clasts; shearing and 'grooves/stretch marks' that affect intrabasinal clasts borders; and injectites. Intrabasinal clasts disrupted may show, internally, faults, folds, boudins and shear-related structures that predate rupture.	>50	2; 5; 6; 7; 8; 9; 12; 14

4.6. STRUCTURAL AND STATISTICAL ANALYSIS

Many deformational products described in the MTDs (see Paper 1 – Rodrigues et al. 2019 submitted) were also analysed through stereographic projections and rose diagrams, such as folds (Fig. 4.2A-C), faults (Fig. 4.2D-H), injectites (Fig. 4.2I), asymmetric boudins (Fig. 4.2J), slickenlines of intrastratal detachment surface, oriented intrabasinal and extrabasinal clasts (Fig. 4.2K), and grooves/stretch marks (Fig. 4.2L). The kinematics indicated by some of these structures, as well as those indicated by sigma structures, quarter structures (Fig. 4.2M) and shearing features at the border of intrabasinal clasts and heterogenous matrix, were also analysed and considered for the understanding of the mass-flow direction.

4.6.1. Folds

Folds were classified as gentle to tight (Fig. 4.2A and B; Fleuty, 1964), and symmetrical or asymmetrical (Fig. 4.2A-C). Asymmetrical folds were identified as S or Z fold in most outcrops. Based on geometry, folds were also classified as sharp (kink band folds; Fig. 4.2C) to rounded, and as cylindrical to gently curvilinear. In general, fold datasets tend to show variable dispersion independent of the amount of data. Where 50% of folds datasets have no robustness to weak robustness, while the other 50% consist of datasets with moderate to strong robustness (Table 4.2). Folds hinge data show, commonly, preferential orientation ranging from weak to strong (Table 4.2). The confidence interval (95%) indicates that folds hinge main orientation ranges ± 4,5° to ± 28.8°, where more than 80% of data set vary ± 10° to ± 30° and about 20% show ± 10° or less (Fig. 4.3H). Axial surface datasets display preferential orientation, usually, weak and, secondarily, moderate to strong (Table 4.2). The confidence interval (95%) range from ± 6.2° to ± 32.1°, with main concentration (75%) between ± 10° and 20° (Fig. 4.3H). Folds facing datasets also show weak to strong preferential orientation (Table 4.1). The confidence interval (95%) range from ±3.9° to ± 34.4°, with about 80% ranging between ± 10° and 30° (Fig. 4.4A). Some datasets of hinges, axial planes and facing have undefined preferential orientation due to limited amount of data (Table 4.2 and Appendix 1). The ridges identified in folded sills of injectites display strong preferential orientation, confidence interval (95%) of ± 4.4° and main orientation parallel to hinge orientation (Fig. 4.3D).

The variety of folds geometry, from simple to complex, is clearly noticed in the stereographic projections, and is associated with progressive deformation and shear variation along the mass flow, which can be more parallel or more normal to the flow direction. Folds characterized by gentle interlimb angle and symmetry (Fig. 4.3A) show cylindrical geometry and unimodal data (hinge, axial plane and facing). These folds probably result from layer-parallel shear (LPS) which have undergone no progressive deformation. Simple folds as gentle symmetric folds generated by LPS were analysed through methods as MAM, MAPS and FFD (Fig. 4.3A). Folds generated by LPS with no hinge orientation display hinges and axial plane strike normal to flow direction flow direction (see Alsop and Marco 2011). Symmetrical folds tend to show up-facing and subvertical axial plane (Fig. 4.3A) that may not indicate properly the flow direction.

Besides that, folds facing and axial plane dip direction of symmetrical folds of locality 18 indicate possible flow toward S (Fig. 4.3A).

The asymmetrical and recumbent folds may be the opposite end-member for symmetrical and up-right folds due to progressive deformation associated to LPS. The example dataset of recumbent folds (Fig. 4.3B) shows bimodal and sub-horizontal hinges, unimodal and subhorizontal axial planes, and subhorizontal folds facing with a bimodal pattern and S and Z folds overlapping. The bimodality of recumbent folds hinges could be a result of progressive deformation of folds generated by LPS to sheath folds (see Alsop and Marco, 2011, and references therein). However, no clear evidence of sheath folding was identified (e.g. recumbent and isoclinal folds) to justify such interpretation (see graphic Fig. 4.3B). Although these folds show closed to tight interlimb angle and subhorizontal axial plane, this relationship is not directly proportional. These recumbents folds were generated by layer-normal shear with some associated progressive deformation. This resulted in axial planes tipping and hinges rotation from subparallel to the paleoslope azimuth to oblique or subparallel to paleoslope strike. This explains the unimodality of axial planes and close folds facing clusters, which were rotated toward each other. Due to this rotation MAM was applied for hinges data (Fig. 4.3B) instead of DAM, which is usually applied for LNS folds. Folds hinges distribution also allowed the application of SAM, which indicated similar direction to MAM (N-S; Fig. 4.3B). For fold facing FFD was applied and interpreted similarly to LNS folds. As recumbent folds display subhorizontal axial planes, it may not indicate properly the flow direction. MAPS results may diverge from the main direction of flow. However, the intersection between the mean axial planes of S and Z folds (AIM) show a more consistent flow direction. The paleslope directions obtained through each of these methods agree with folds vergence toward N (Fig. 4.3B).

Progressive deformation of layer-parallel shear folds result in variation of axial plane dip angle during deformation, and sometimes this variation may be seen in the same set of folds (Fig. 4.3C). For this kind of folds the decrease of axial plane dip angle occurs associated with a decrease in interlimb angle (see graphic in Fig. 4.3C). This kind of variation resulted in a fanning distribution of axial plane data. Besides, this particular distribution of axial plane data, the example dataset shows unimodal pattern for folds hinges, axial planes and folds facing. Some folds hinges and facing show different orientation in relation to their main concentration (Fig. 4.3C), which may be related to local rotation and/or refolding during progressive deformation. Besides

applying MAM, MAPS and FFD for folds generated by layer-parallel shear, that have undergone some progressive shear deformation with little hinge rotation, methods that tend to avoid the influence of more rotated data, such as MAD, were also applied. This method was applied for hinges associated with steeper axial planes (typically >45°relative to non-deformed beds), once folds with steeper axial plane are considered to have undergone less significant modification by progressive deformation in a set of LPS folds (Alsop and Marco, 2012). Considering the same principle, it is proposed a new method based in the mean orientation of this steeper axial planes (MAD-AP), which may give a more reliable direction than the MAPS, as in this example case (Fig. 4.3C). The methods MAD and MAD-AP confirmed the flow trend indicated by other methods, while the second methods indicated a clear sense of flow that agree with folds vergence (Fig. 4.3C).

Folds generated by LNS are characterized by its bimodal hinges, axial plane and fold facing data (more information in Table 4.1 of Alsop and Marco, 2011); however, the progressive deformation of this folds may also result in data rotation. In the example case (Fig. 4.3D), axial planes and folds facing show a bimodality with a little overlap of S and Z folds, while folds hinges form basically a cluster (unimodal pattern) with an overlap between S and Z folds. These folds also show some relationship between axial plane dip angle and interlimb angle (Fig. 4.3D) that may be associated with progressive deformation, although not so clear as for LPS folds. Regardless if folding is generated by LPS or LNS, comparing the relationship between axial plane dip angle and the interlimb angle (Fig. 4.3E) of the example folds (Fig. 4.3A-D) and considering their geometric characteristics was verified a clear influence of progressive deformation in folds geometry. Where symmetrical/up-right and gentle folds and asymmetrical/recumbent and tight folds are the end-members of the progressive deformation line, which leads to interlimb angle tightening and axial planes rotation and flattening towards the flow plane (e.g. Alsop and Marco 2013). For folds generated by LNS, methods as DAM, AIM and FFD were usually applied (Fig. 4.3B and 4.3D). For most LNS folds, when MAPS is applied for all axial plane data (S and Z folds) the mean plane calculated show strike normal to folds hinge. Although it may not represent the real orientation of axial plane of LNS folds, the dip direction of the mean plane (MAPS) is parallel to the transport direction obtained through AIM, DAM and FFD and was also used for paleoslope definition (Fig. 4.3D).

Some folds show particular geometry, such as kink band folds and diapiric folds, which result from quite different processes. Kink band folds show hinges in an arcuate concentration with some overlap of S and Z folds, while axial planes and fold facing show a bimodal pattern (Fig. 4.3F). This data distribution reflects the kink band folds geometry, which tend to form conjugated pairs. The comparison between interlimb angle and axial plane dip angle suggests no correlation (Fig. 4.3F), which may indicate no progressive deformation or it may affect differently kink band folds. This kink bands folds were interpreted to form with hinges and axial plane strike normal to flow direction and for that we applied MAM, MAPS, AIM and FFD. Due to dispersion of data and to verify the flow direction without interference of possibly rotated data we also applied MAD and MAD-AP.

Diapiric folds may show quite complex geometries. Consequently, these folds show high data dispersion (Fig. 4.3G). However, some preferential orientation was identified (Fig. 4.3G), which indicates that most diapirs should have an elongated shape. Elongated diapirs tend to be more or less parallel to paleoslope strike. The interlimb angle and axial plane dip angle relationship suggest progressive deformation for these folds (Fig. 4.3G). This may be evidence that these diapirs and diapiric folds were originated by local mass flows. For these folds MAM, MAPS and FFD indicate similar flow direction. MAD and MAD-AP also indicate similar flow direction, that confirms the idea of elongated diapirs, once steeper folds (with axial plane ~>45°) may represent more properly the geometry and flow direction.

The confidence interval (95%) of average transport direction of each fold dataset was calculated from transport directions obtained through the methods applied for definition of paleoslope. Folds average transport direction show confidence interval (95%) between ± 3.6° and ± 33.5°, where more than 80% is less than ± 20° (Fig. 4.3I). More than 60% of folds average transport direction were classified with moderate to very strong robustness (Table 4.2 and Appendix 2).

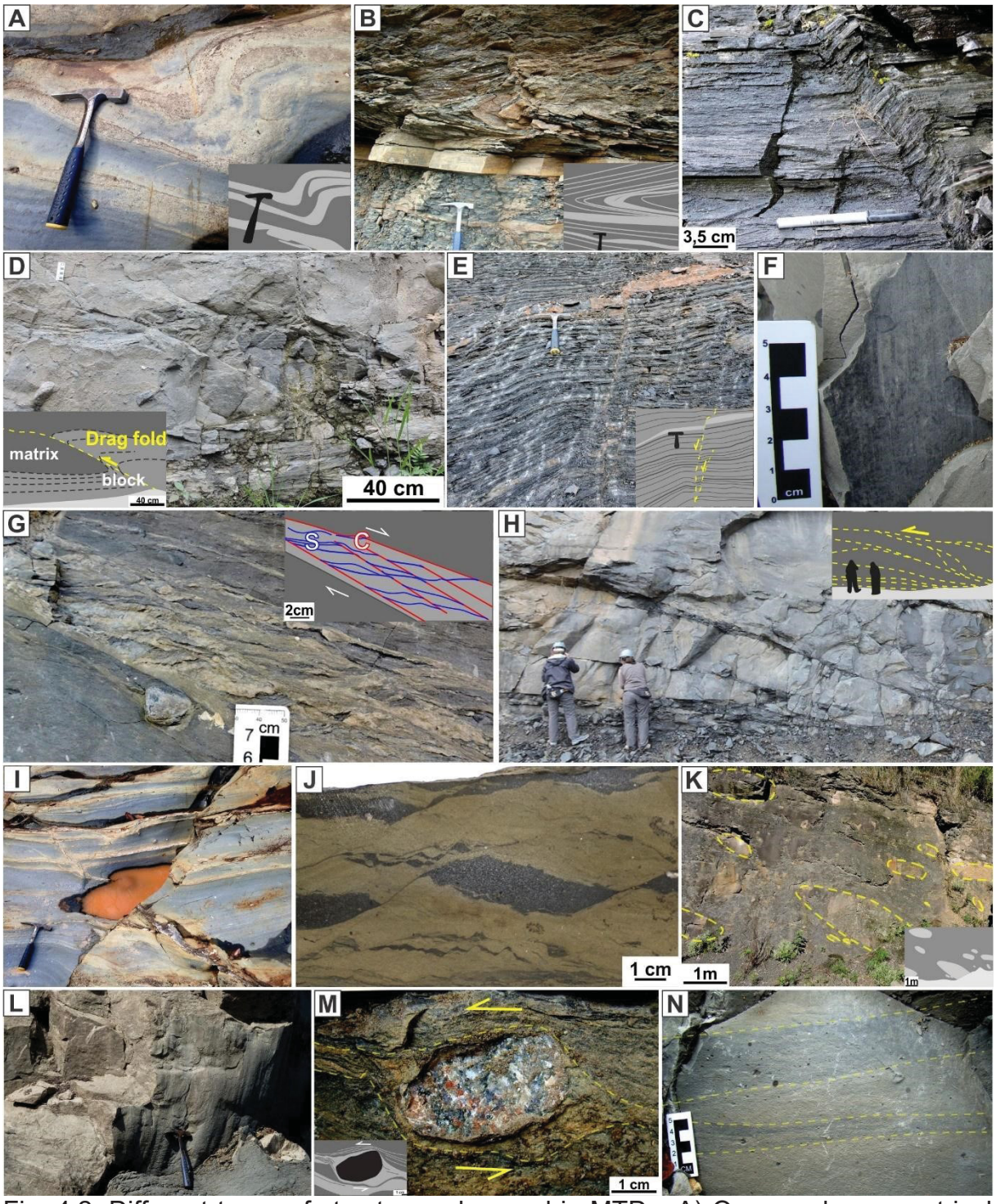

Fig. 4.2: Different types of structures observed in MTDs. A) Open and asymmetrical fold. B) Closed and asymmetrical fold. C) Kink-band fold. D) Reverse fault with associated drag fold. E) Normal faults. F) Displacement surface with slickenlines in continuous clay smear. G) Clay-sand smear with SC-like feature. H) Reverse anastomosed faults zone. I) Sandy injectites in the form of sills and dikes. J) Asymmetric boudins. K) Oriented sandstone clasts. L) Grooves/stretch marks at intrabasinal clasts border. M) Quarter structure around a granite clast. N) Heterogenous matrix with discrete textural/compositional banding (banded matrix).

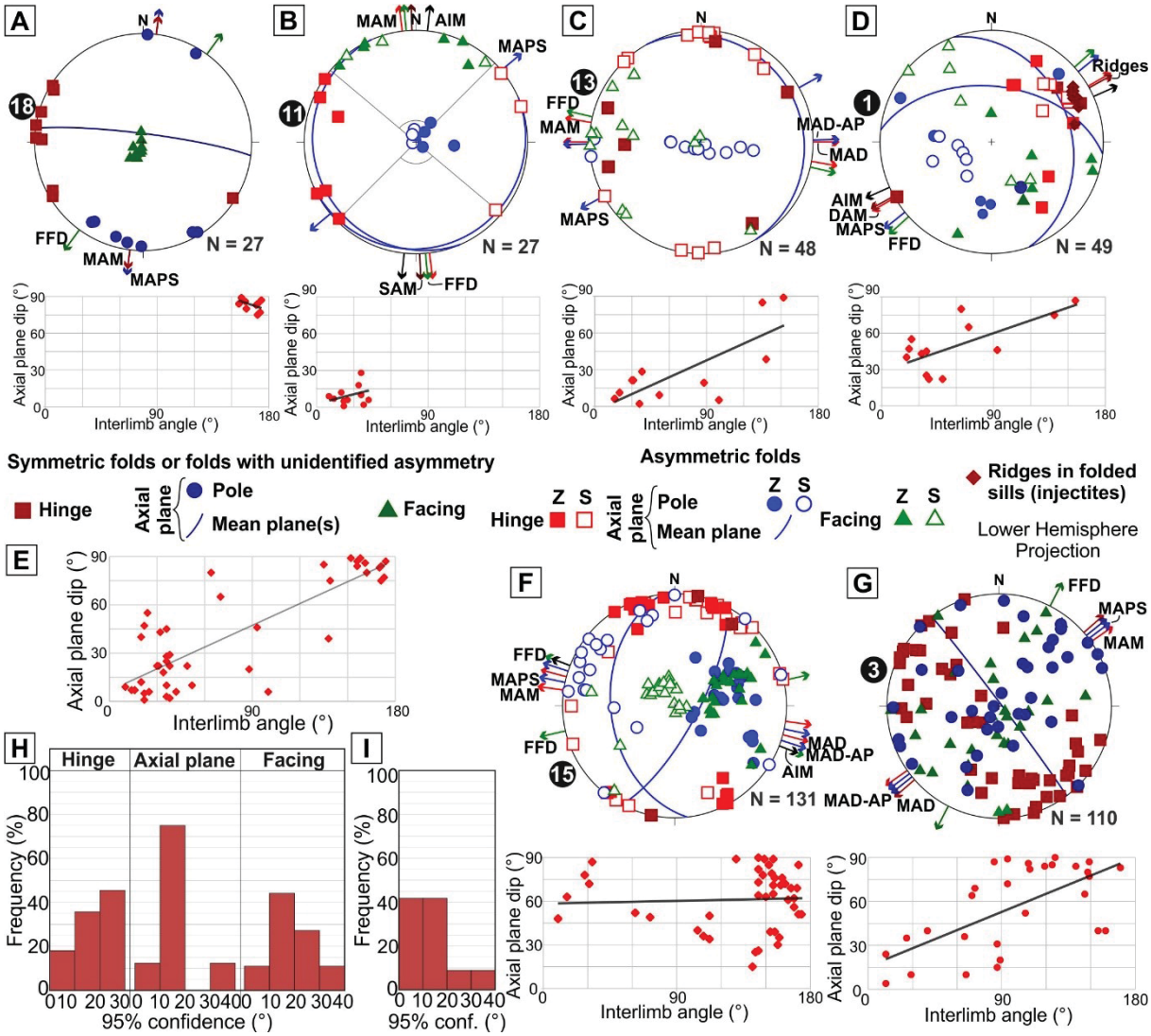

Fig. 4.3: Example of folds with stereograms and graphics (axial plane dip angle versus interlimb angle), with indication of transport direction (indicated in the stereograms by arrows) obtained through each method applied (indicated by acronyms): A) Gentle and symmetrical folds generate by LPS (locality 18); B) Recumbent folds, with close interlimb angle, generated by LNS (locality 11); C) Asymmetrical folds generated by LPS with positive relationship between axial plane dip angle and interlimb angle indicating progressive deformation (locality 13); and D) Asymmetrical folds generated by LNS with relatively positive relationship between axial plane dip angle and interlimb angle indicating progressive deformation (locality 1). E) Graphic of axial plane dip angle versus interlimb angle with data of examples datasets of (localities 1, 11, 13 and 18) that exemplify the evolution of folds with progressive deformation from gentle and symmetrical folds to close and recumbent folds. Example of particular kinds of folds, with respective stereograms and graphics (axial plane dip angle versus interlimb angle): F) Kink band folds, which show no relationship axial plane dip angle and interlimb angle probably indicating no progressive deformation; G) Diapiric folds that show positive relationship between axial plane dip angle and interlimb angle indicating progressive deformation. Histograms of all folds datasets: H) indicating the confidence interval (95%) of folds elements (hinge, axial plane and facing); and) indicating the confidence interval (95%) of the average transport direction of each fold dataset (each locality). The number of data (N) is indicated next to each stereogram.

Table 4.2: Structures datasets preferential orientation based in Strength parameter C and datasets and transport direction based on classification of different parameters indicated in the Appendixes 1 and 2.

Type of structure	Outcrop localities	Structures		
		Datasets Preferential orientation	**Datasets Classification**	**Transport direction classification**
Folds	1; 2; 3; 4; 5; 8; 10; 11; 13; 15; 16; 18	Hinge: 30.8% undefined, 30.8% weak, 23% moderate, 15.4% strong	21.4 % no robustness, 14.3% very weak robustness, 14.3% weak robustness, 43% moderate robustness, 7% strong robustness	14.3% no robustness, 21.4 weak robustness, 21.4% moderate robustness, 35.7% strong robustness, 7.2% very strong robustness
		Axial surface: 10% undefined, 50% weak, 30% moderate, 10% strong		
		Facing: 10% undefined, 50% weak, 30% moderate, 10% strong		
Faults	1; 4; 5; 6; 8; 9; 10; 12; 13; 14; 15; 17; 18	Faults: 43.5% undefined, 21.7% weak, 34.8% moderate	6.25% no robustness, 18.75% very weak robustness, 18.75% weak robustness, 50% moderate robustness, 6.25% strong robustness	6.25% no robustness, 18.75% weak robustness, 50% moderate robustness, 25% strong robustness
		Slickenlines: 40% undefined; 60% weak		
Injectite	1; 8; 13	33% undefined, 67% weak	33.3% weak robustness, 33.3% moderate robustness, 33.3% strong robustness	33.3% weak robustness, 33.3% moderate robustness, 33.3% strong robustness or 33.3% weak robustness, 66.7% moderate robustness
Boudins	10	moderate	moderate robustness	strong robustness
Slickenlines (intrastratal)	10	weak	weak robustness	weak robustness
Clasts oriented	14	Intrabasinal: weak	weak robustness	moderate robustness
		Extrabasinal: weak	moderate robustness	weak robustness
Grooves/ Stretch marks	6	weak	moderate robustness	weak robustness
Bedding	3; 4; 5; 10; 11; 13; 15; 16; 17; 18	45.5% weak, 54.4% moderate	27% moderate robustness, 64% strong robustness, 9% very strong robustness	91% moderate robustness, 9% strong robustness
Banded matrix	1; 2; 8	weak	67% moderate, 33% strong	moderate robustness

4.6.2. Faults

Faults occur as individual planes or clusters with straight, wavy or anastomosed shape (Fig. 4.2D-H). Kinematics can be reverse (Fig. 4.2D and H), normal (Fig. 4.2E and G) or undefined due to a lack of reliable indicators. Sometimes it was possible to identify antithetic and/or synthetic faults in some datasets. Faults can occur associated with other features such as drag folds (Fig. 4.2D) and tilted bedding. Some particular kinds of faults identified include fault with sheared muddy core of centimetric thickness, continuous clay smear (Fig. 4.2F and H), discontinuous clay smear and faults forming “SC” features (Fig. 4.2G), also associated with clay-sand smearing.

Faults datasets show usually a variable dispersion, independent on the amount of data. The preferential orientation tends to be weak to moderate (56.5%; Table 4.2 and Appendix 2) or undefined (43.5%; Table 4.2 and Appendix 2). For some datasets of which 50% is weak, 15% moderate and 10% strong, against 25% with none preferential orientation. The mean orientation of the faults displays confidence interval (95%) that range from ± 3.2° to ± 41.3°. Besides the wide range, 70% of faults sets show variation of ± 20° or less, while for 30% the confidence interval is between ± 20° and ± 50° (Fig. 4.4H). Faults slickenlines also show variable dispersion, usually similar to the related faults and, commonly weak preferential orientation (60%; Table 4.1 and Appendix 1). The confidence interval (95%) ranges from ± 13.4° to ± 30.1°, with 50% between ± 10 and ±20° and 50% between ± 20 and ± 40° (Fig. 4.4H). Folds datasets were classified mostly with weak to moderate robustness (75%; Table 4.2 and Appendix 1).

Normal faults tend to show moderate to high dip angles (Fig. 4.4A-C). Moderately dipping faults (Fig 4.4D and E) are usually associated with “SC” features or anastomosed sets. Faults with unclear kinematics show moderate to low dip angle (Fig. 4.4D, E and F). Reverse faults usually show low to moderate dip angles (Fig. 4.4D-G). Reverse faults with low dip angle correspond to thrust faults or anastomosed sets. The faults may display simple pattern with one dataset concentration (Fig. 4.4A) or conjugated pattern (Fig. 4.4B, C, F and G). For simple datasets just the MFOM was applied. The conjugated pattern consists, usually, of faults with more or less parallel strike direction and opposite dip directions (Fig. 4.4B, F and G), however it may also consist of obliquely conjugated faults (Fig. 4.4C). For both cases MFOM and FIM were

applied for each cluster (Fig. 4.4B, C, F and G). The method FIM considers the intersection between the mean plane of each cluster, where in conjugated faults with parallel strike is normal to flow direction (Fig. 4.4B, F and G) and in conjugated faults with oblique strike the intersection is parallel to the flow (Fig. 4.4C).

The faults sometimes present slickenlines (Fig. 4.2F, 4.4C, 4.4D, 4.4E and 4.4F), mainly in clay smear that display detachment surface or faults generated in mudstones. In these cases, slickenlines may not show kinematic indicators, which resulted in datasets of faults with slickenlines of unidentified kinematic (Fig. 4.4F). The mean orientation of the slickenlines (SLM) was also used for paleoslope definition and considered to be parallel to flow direction, once they display an overall dip pattern (Fig. 4.4C-F).

In some localities we identified both normal and reverse faults, and sometimes faults of unidentified kinematics (Fig. 4.4D and E). In these cases, normal and reverse faults tend to form one main set each, with parallel to subparallel strike direction and opposite dip directions (Fig. 4.4D and E); while the unidentified fault tend to form one concentration, in which the main fault plane displays subparallel (Fig. 4.4D) to oblique (Fig. 4.4E) strike direction to normal and reverse faults. In this case MFOM were applied for each cluster of each kind of fault and the intersection (FIM) was calculated between the mean plane of normal fault and the mean plane of reverse fault, which were interpreted to be normal to flow direction (Fig. 4.4D and E).

The confidence interval (95%) of average transport direction of each fault dataset, calculated from methods applied to faults and slickelines data when present, show values between ± 2.2° and ± 36°. From this transport direction about 56% display confidence interval (95%) of less than ± 20° (Fig. 4.4I). The average transport directions were classified as moderate to very strong robustness (75%; Table 4.2 and Appendix 2).

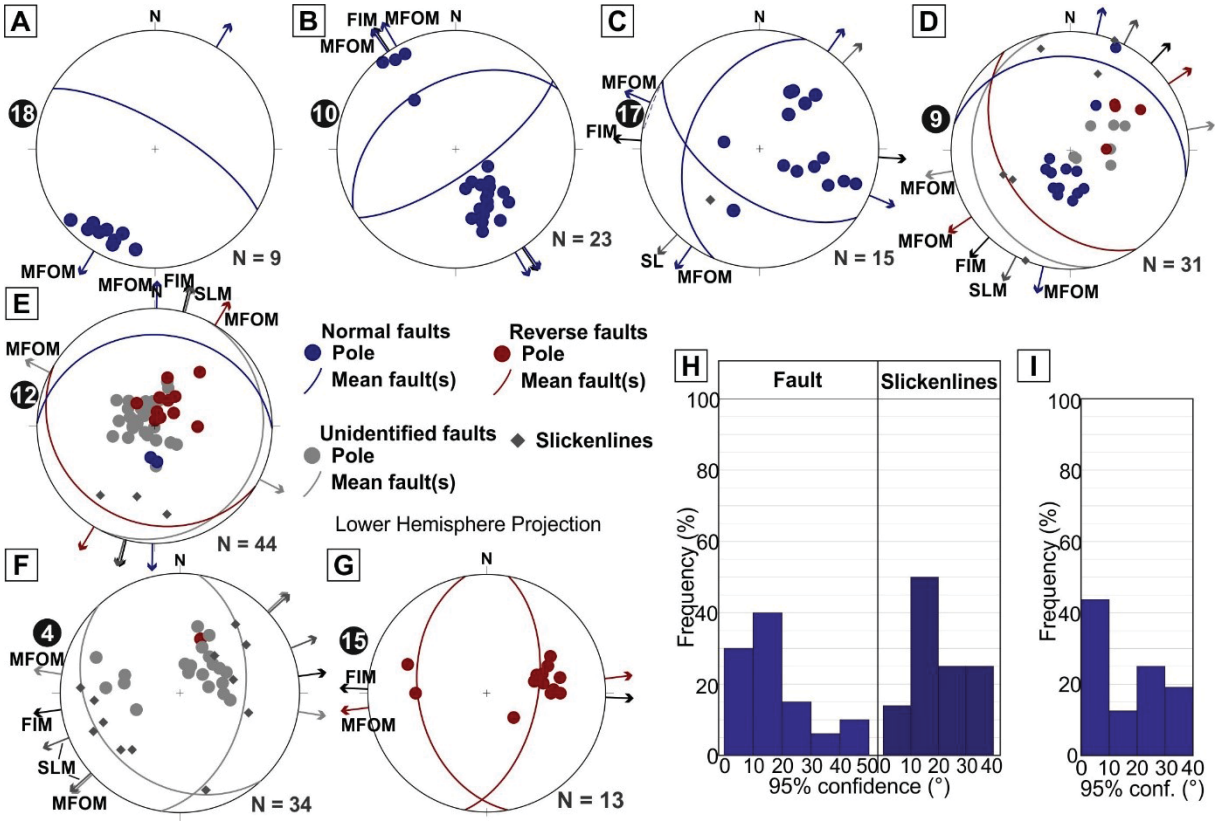

Fig. 4.4: Example of faults datasets stereograms: A) Normal faults with single cluster (locality 18), possible antithetic faults (with respect to regional information of paleocurrents of associated deposits) associated to major normal fault; B) Normal faults with conjugated parallel pattern (locality 10), in which the main cluster was identified as the synthetic faults with respect to others kinematics indicators; C) Normal faults with conjugated oblique pattern (locality 17); D) Normal, reverse and unidentified faults that show more or less parallel strike, while normal and reverse faults show opposite dip direction that indicate sense flow toward NE (locality 9); E) Normal, reverse and unidentified faults, of which normal and reverse faults show parallel strike and opposite dip direction indicating sense of flow toward NE (locality 12); F) Reverse fault and faults of unidentified kinematics (some intrastratal) with slickenlines (locality 4); G) Reverse faults with conjugated parallel pattern (locality 15). in which the main cluster was identified as the antithetic faults with respect to regional information of paleocurrents of associated deposits. Histograms of all faults datasets: H) indicating the confidence interval (95%) of faults and slickelines; and) indicating the confidence interval (95%) of the average transport direction of each fault dataset (each locality) from transport directions obtained through different methods of paleoslope definition (indicated in the stereograms by arrows and method by acronym). The number of data (N) is indicated next to each stereogram.

4.6.3. Injectites

Injectites occur as dikes (Fig. 4.2I), with tabular to anastomosed geometry or *en echelon*, and when intruded in MTD with bedding or well-defined banded matrix it is possible to identify associated tabular sills (Fig. 4.2I). In the MTD of locality 1 sills are

folded together with banded matrix. The dikes that connect these sills (Fig. 4.5A - dikes I; locality 1) show two main strike directions, more or less subparallel to each other and with opposite dip direction and moderate to subvertical dip angle. A second phase of injection generated thin dikes (mm thickness; Fig. 4.5A – Dikes II) that cut the folded banded matrix, sills and dikes (I) in the locality 1. These dikes show one main orientation and are subvertical (Fig. 4.5A). Comparing the orientation of the dikes I with folding, which is main type of deformation in this MTD, it seems that dikes I originated either subparallel or subnormal to flow direction while dikes II were generated normal to flow direction.

Injectites associated or parallel to continuous clay smear were described in locality 8. These injectites consist of dikes that intruded the heterogeneous, banded matrix. These dikes display a clear preferential orientation and tend to show moderate dip angle (Fig. 4.5B). In this case, the injection was interpreted to occur normal to the flow direction, which agree with general flow direction indicated by other structures. Other dataset of injectites was collected in the MTD of locality 13 and consist of subvertical dikes associated to a few and little intruded subhorizontal sills (Fig. 4.5C). These dikes are more or less parallel to faults, oblique to folding and oblique to normal to flow direction. Although the injectites usually show preferential orientation, an irregular injection pattern associated with breccias and resembling hydraulic fracturing was identified locally.

The injectites usually have a weak preferential orientation (67%; Table 4.2 and Appendix 1). Some datasets may display undefined preferential orientation (33%; Table 4.2 and Appendix 1) due to limited amount of data. Injectites datasets have weak to strong robustness (Table 4.2 and Appendix 1) The confidence interval (95%) ranges from ±6° to ±17.5° (Fig. 4.5D). The confidence interval (95%) of average transport direction of injectites of each MTD show values between ± 6° and ± 42.38° (Fig. 4.5E). While the transport direction classification indicates weak to strong robustness or weak to moderate depending on the interpretation of the orientation of injectites of locality 1 (Table 4.2, Appendix 1 and 2).

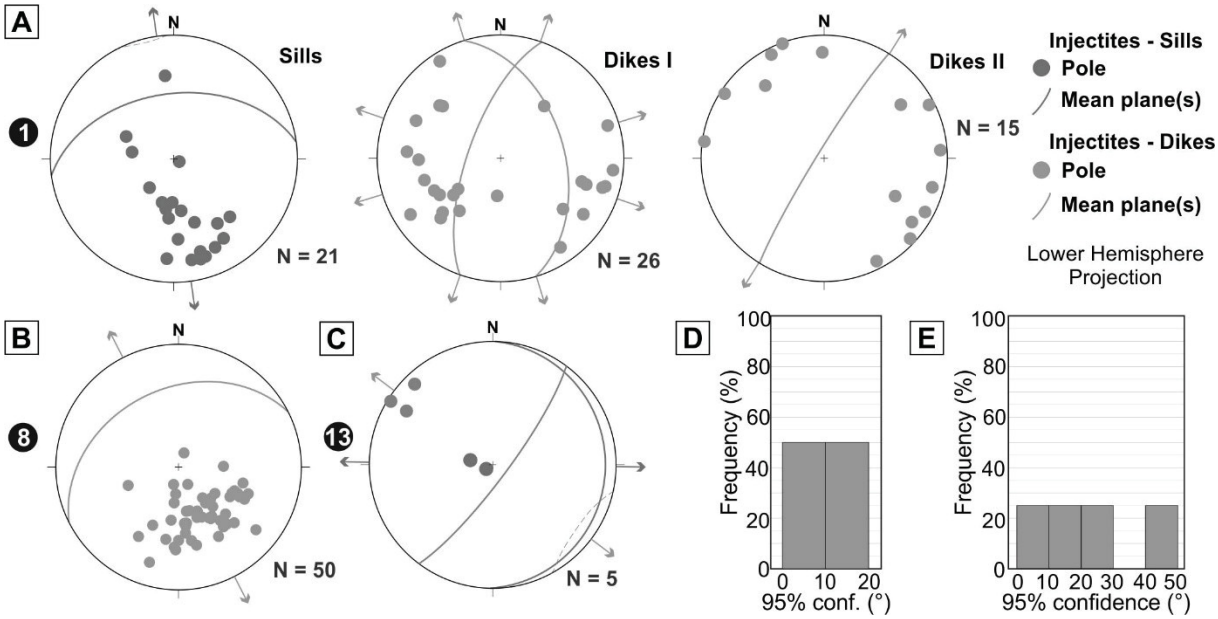

Fig. 4.5: Stereograms of injectites datasets: A) Sill and associated thicker dikes (I) generated in a first stage and thinner dikes (II) generated in a second stage (locality 1); B) Injectites associated to continuous clay smear with normal kinematics (locality 8); C) Dikes and associated sills (locality 13). Histograms of injectites datasets: D) indicating the confidence interval (95%) of injectites clusters; and) indicating the confidence interval (95%) of the average transport direction of injectites datasets of each locality from transport directions obtained by comparison with other structures (indicated in the stereograms by arrows). The number of data (N) is indicated next to each stereogram.

4.6.4. Other structures

Other structures analysed include asymmetric boudins, slickenlines identified in intrastratal detachment surface, grooves and stretch marks and intrabasinal and extrabasinal clasts. The asymmetric boudins (Fig. 4.2J) consist of shearband boudins, which show backward vergence resulting from antithetic rotation with respect to shearing. The axis of this asymmetric boudins have moderate preferential orientation (Table 4.2 and Appendix 1) and confidence interval (95%) of 13.7° (Fig. 4.6A and F). Boudin faults show preferential strike direction, which are more or less parallel to boudin axis. These faults encompass normal and reverse faults and are distributed in two clusters of opposite dip direction. They have low to moderate dip angles (Fig. 4.6A), moderate preferential orientation (Table 4.2 and Appendix 1) and confidence interval (95%) of 7.6° (normal faults) and 4.6° (reverse faults; Fig. 4.6F). The variation in boudin fault dip direction results of later gentle folding of the bedding containing these boudins. Both normal and reverse faults indicate kinematics towards NW (Fig.

4.6A), which agree with flow direction deduced from other kinematic indicators. Therefore, the extension that generated these boudins was considered to be parallel to flow direction and so axis and strike direction of faults is normal to flow direction. Based on that, MAM was applied to axis data and MFOM and FIM to fault data (Fig. 4.6A). The average transport direction of this boudins show confidence interval (95%) of 11.3° (Fig. 4.6F) and show strong robustness based in the transport direction classification (Table 4.2 and Appendix 1). Considering the general classification, the asymmetric boudins studied show strong robustness (Table 4.2, Appendix 1 and 2).

The slickenlines of intrastratal detachment surface were developed along shale lamination or muddy lamination in rhythmites and may be related to faulting or folding. The dataset collected is associated to folding, for that these slickenlines display opposite dip direction with a main trend (Fig. 8B), weak preferential orientation (Table 4.2 and Appendix 1) and confidence interval (95%) of 22.6° (Fig. 4.6F). The dataset, transport direction and general classification of intrastratal slickenlines show weak robustness (Table 4.2, Appendix 1 and 2). The main trend for oriented clasts (elongated intra- and extrabasinal granules to blocks) (Fig. 4.2K) were defined through rose diagram of their major axes (e.g. Sobiesiak et al., 2016). Although extrabasinal clasts display higher dispersion than intrabasinal clasts (Fig. 4.6C and D, respectively) with confidence interval (95%) of 22.3° and 15.3°, respectively (Fig. 4.6F), both show weak preferential orientation (Table 4.2 and Appendix 1). For intrabasinal oriented clasts studied, the dataset classification indicates weak robustness, while transport direction and general classifications indicate moderate robustness (Table 4.2, Appendix 1 and 2). The dataset of the extrabasinal oriented clasts was classified as with weak robustness, while the transport direction and general classifications indicate moderate robustness (Table 4.2, Appendix 1 and 2). Intrabasinal clasts may show also deformation at their borders (see Paper 1), such as grooves and stretch marks (Fig. 4.2L). These features were analysed through rose diagram as axes (as Ogata et al., 2014), which indicated a main trend (Fig. 4.6E) with confidence interval (95%) of 14.3° (Fig. 4.6F), despite the dataset weak preferential orientation. The grooves and stretch marks studied show moderate robustness for dataset classification and weak robustness transport direction and general classification (Table 4.2, Appendix 1 and 2). The main orientation of each of these structures was considered in paleoslope definition.

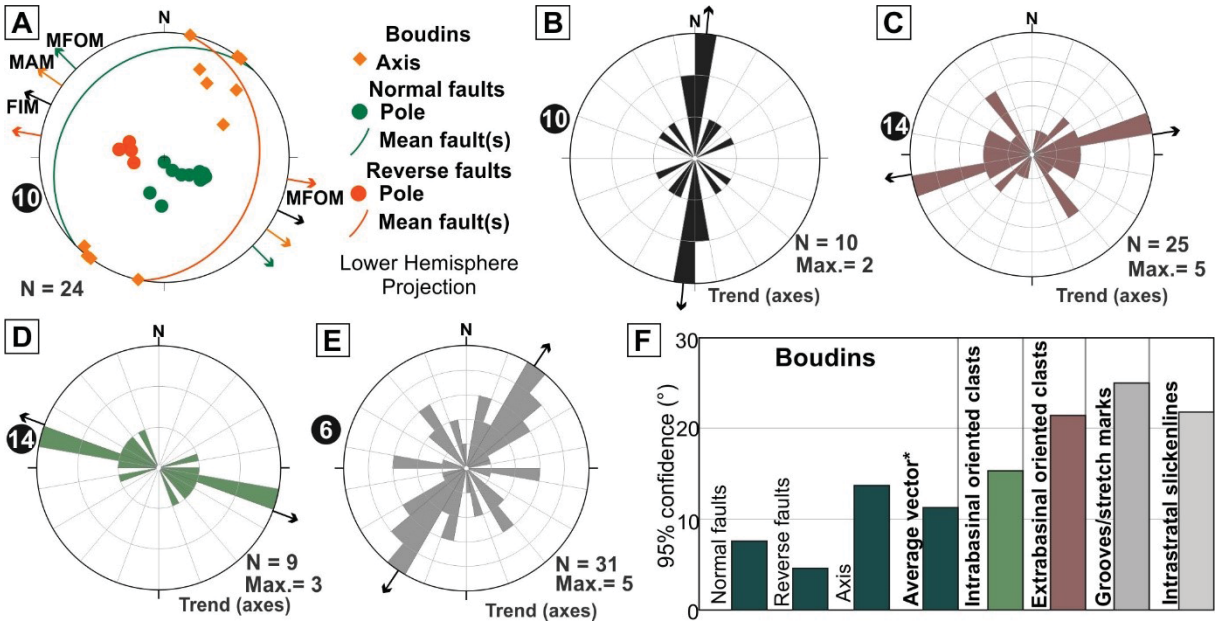

Fig. 4.6: A) Stereogram of asymmetric boudins with boudins faults and axis plotted and transport direction (indicated in the stereograms by arrows) of different methods of paleoslope applied (indicated by acronyms; locality 10). B) Rose diagram of slickenlines of intrastratal detachment surface with transport direction (indicated in the stereograms by arrows; locality 10). C) Rose diagram of oriented extrabasinal clasts with transport direction (indicated in the stereograms by arrows; locality 14). D) Rose diagram of oriented intrabasinal clasts with transport direction (indicated in the stereograms by arrows; locality 14), E) Rose diagram of grooves and stretch marks at intrabasinal clasts with transport direction (indicated in the stereograms by arrows; locality 6). F) Graphic with the confidence interval (95%) of each element of asymmetric boudins (faults and axis) and the average transport direction of asymmetric boudins, as well as, the confidence interval of the datasets of oriented intrabasinal and extrabasinal clasts, grooves/stretch marks and intrastratal slickenlines. The number of data (N) is indicated next to each stereogram or rose diagram.

4.6.5. Bedding and banded matrix

According to Jones (1939), bedding in MTDs can be expected to show preferential orientation with respect to the paleoslope. The strike orientation of bedding is considered to be subparallel or parallel to paleoslope strike (MBSM), but this should be applied with caution due to fold geometry variation, tilting, rotation and later tectonic activities (Sharman et al., 2015).

For those MTDs with some bedding preservation or heterogenous matrix (Fig. 4.2N) with compositional/granulometric banding, the MBSM was applied. Bedding display, commonly, a weak to moderate preferential orientation and the datasets were classified as moderate to very strong robustness (Table 4.2, Appendix 1). They also show confidence interval (95%) between ±4° and ±11.7°, of which more than 70% is

less than ±10° (Fig. 4.7A). The bedding transport direction classification indicate mostly moderate robustness and secondarily strong robustness (Table 4.2, Appendix 2). Banded matrix shows weak preferential orientation and dataset classified with moderate to strong robustness (Table 4.2, Appendix 1). The confidence interval for banded matrix is of ±9.6° to ±17.5°, with more than 65% of datasets between ±10° and ±20° (Fig 4.9A). The banded matrix transport direction classification indicates moderate robustness (Table 4.2, Appendix 2).

The transport direction obtained for each bed and band dataset was evaluated in relation to the mean orientation obtained through the structures that occur in the same locality. One aspect analysed was the angle between the paleoslope azimuth indicated by bedding or banded matrix and the mean paleoslope azimuth obtained from other structures, considering for that the most plausible flow direction based on kinematic indicators. The angle between bedding and structures average transport direction range from 2° to 86° and more than 80% is less than 60° (Fig. 4.7B). While the angle between banded matrix and structures average transport direction range from 11° to 109°, with about 55% less than 60° (Fig. 4.7B). Comparing the final transport direction for each MTD (where bedding or banded matrix data was collected) using MBSM with the final transport direction without MBSM is verified change of orientation from 3° to 15° (90% less than 10°) in MTDs with bedding and from 4° to 41° (80% less than 10°) in MTDs with banded matrix (Fig. 4.7C).

Other aspect analysed was the confidence interval (95%) of final transport direction of each MTD, which present bedding or banded matrix, calculated with and without MBSM. For MTDs with bedding the final transport direction without MBSM display confidence interval (95%) between ±6.7° and ±31.9°, with more than 80% less than ±20° (Fig. 4.7D), while the confidence interval for the final transport direction with MBSM range from ±9.8° to ±36.5°, where about 80% of the transport direction show confidence interval less than ±20° (Fig. 4.7E). MTDs with banded matrix have the final transport direction without MBSM ranging from ±10° to ±26.4° with 60% between ±10° and ±20° (Fig. 4.7D), while the final transport direction with MBSM display confidence interval between ±8.5° and ±31° of which 60% is less than ±20° (Fig. 4.7E).

Although the direction obtained through MBSM may vary widely with respect to other structures, in most cases the bedding and banded matrix direction tend to be subparallel to oblique (Fig. 4.7B) and the final transport direction (Fig. 4.7C) or its confidence interval (Fig. 4.7D and E) do not seem to change a lot. Based on that, the

results obtained through MBSM for bedding and matrix banded matrix was considered to define the final average transport direction of flow for each MTD.

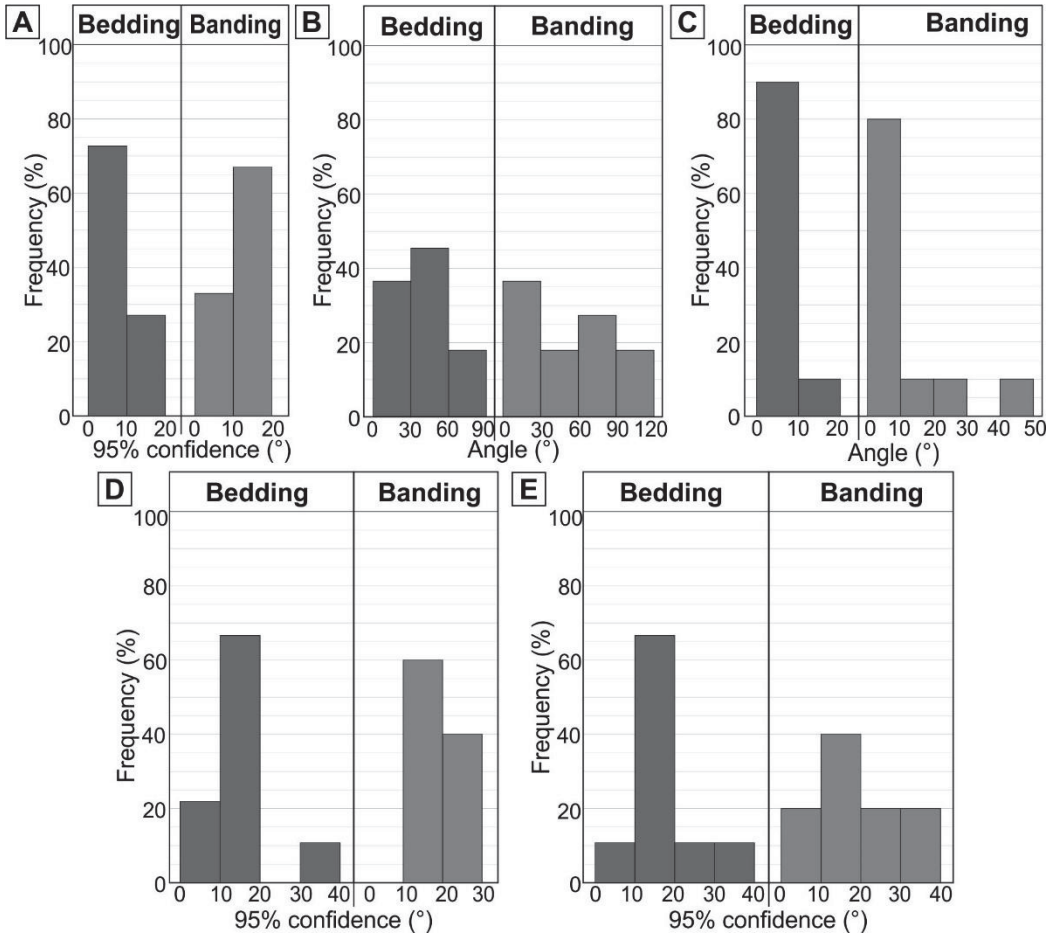

Fig. 4.7: Histograms of: A) the confidence interval (confidence interval 95%) of datasets of bedding and banded matrix; B) the angle between the transport direction of bedding and banded matrix with the transport direction of the structures; C) the angle between the final transport direction of each locality with and without the transport direction of bedding and banded matrix (MBSM); D) the confidence interval (95%) of the final transport direction of each locality without MBSM; and E) the confidence interval (95%) of the final transport direction of each locality with MBSM.

4.7. MTD KINEMATICS VS. OTHER PALEOFLOW INDICATORS

Through the deformational structures one main paleoflow direction was indicated for most outcrop localities (Fig. 4.9), but for two localities two possible directions were defined with a slightly oblique orientation and same sense, depending on the interpretation of the orientation of one structure in relation to the flow direction. In general, the calculated paleoflows have a confidence interval (95%) ranging from ±7.4° to ±36.5° with about 70% of the paleoflows with less than ±20° of confidence

interval (Fig. 4.8). The evaluation of structures datasets, structures transport direction and final transport direction combined by outcrop locality allowed us to define the robustness for each final transport direction, which correspond to the MTD paleoflow (Fig. 4.9 and Appendixes 1 and 2). Most MTDs paleoflow defined here show moderate robustness (70.6%; Fig. 4.9), some MTDs paleoflow have strong robustness (23.5%; Fig. 4.9) and just one MTD paleoflow show weak preferential orientation (5.9%; Fig. 4.9) These results were compared with paleocurrent records previously collected near and in the same stratigraphic level than the studied MTDs by several studies.

Placed in T1, localities 4 and 5 show, in general, a paleoflow towards the W (Fig. 4.9), which is subparallel to paleocurrents obtained from turbidites in the nearby by Juk (2016). The MTD of locality 6 revealed a paleoflow to SW, which is in agreement with paleoflow direction obtained by Amato (2017) using anisotropy of magnetic susceptibility (AMS) in the same diamictite. However, this direction diverges from paleocurrents of fluvial-deltaic deposits in the surroundings (Beraldin, 2014; Rosa et al., 2019), that indicate stream flows going to N and NW. All MTDs paleoflow placed in T1 show moderate robustness.

T2 presents two MTD localities (3 and 8), respectively located in the northern and central regions of the studied outcrop belt. Both MTDs revealed paleoflow to NE (strong robustness) and NNW (moderate robustness), even the localities being located several hundreds of km from each other Fig. 4.9). This paleoflow direction is the same indicated by cross-stratified sandstones interpreted as proglacial fluvial and delta-plain deposits (Vesely and Assine, 2006; Carvalho and Vesely, 2017). In locality 3 these sandstone facies lie directly onto the deformed facies (DF-1) on which the structural analysis was conducted.

T3 contains the largest number of MTD localities. Localities 1 and 2, which correspond to two separate MTD units, have paleoflows to SW with moderate robustness and in agreement with paleocurrents from outwash and fluvio-deltaic facies placed both below and above the MTDs (Mottin et al., 2018). On the other hand, in locality 9, inferred mass-flow direction is to the NE and show strong robustness. Fluvio-deltaic paleocurrents of this time interval near locality 9 are not available, but current ripples and flute casts from underlying turbidites 60 km to SE indicate westward turbidity currents flowing perpendicular to the mass flows (Fallgatter, 2015).

In the southern sector of the study area all MTDs are from T3 (Rio do Sul Formation). Within this interval, all outcrops except for locality 11 are placed above the

Lontras shale and compose a MTC (mass transport complex) at the upper Rio do Sul. Fluvial and delta-plain paleocurrents (above MTD) in this area are preferentially to the west, with some variations to SSW and NW (Schemiko, 2018), whereas turbidity currents (below MTD) flowed to the NW with local variation to SW (Fallgatter, 2015; Schemiko, 2018). MTDs from localities 10 to 12 have paleoflow ranging from NE and NW in agreement with AMS results from Amato (2017) but oblique to perpendicular to paleocurrents. The paleoflow in localities 10 and 12 show moderate robustness, while the paleoflow in locality 11 have strong robustness. MTDs from localities 13 to 18, more to the south, display a radial paleoflow pattern ranging from WNW to SW that is strongly parallel to paleocurrents (Schemiko, 2018) and corroborate MTD kinematics from AMS data (Amato, 2017). Most of these localities show paleoflow with moderate robustness, while the locality 15 and 16 show strong and weak robustness, respectively.

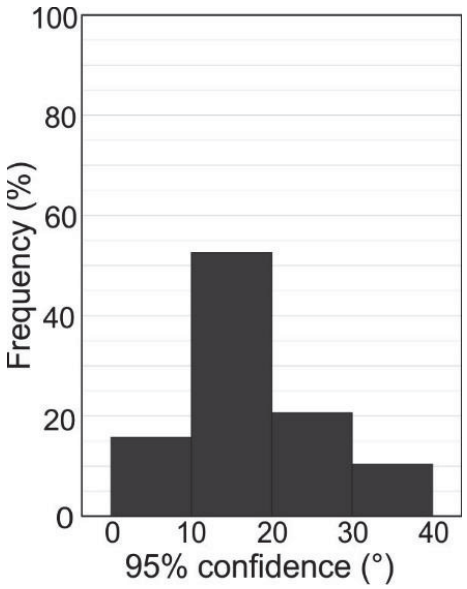

Fig. 4.8: Histogram of confidence interval of the paleoflows defined for the studied MTDs.

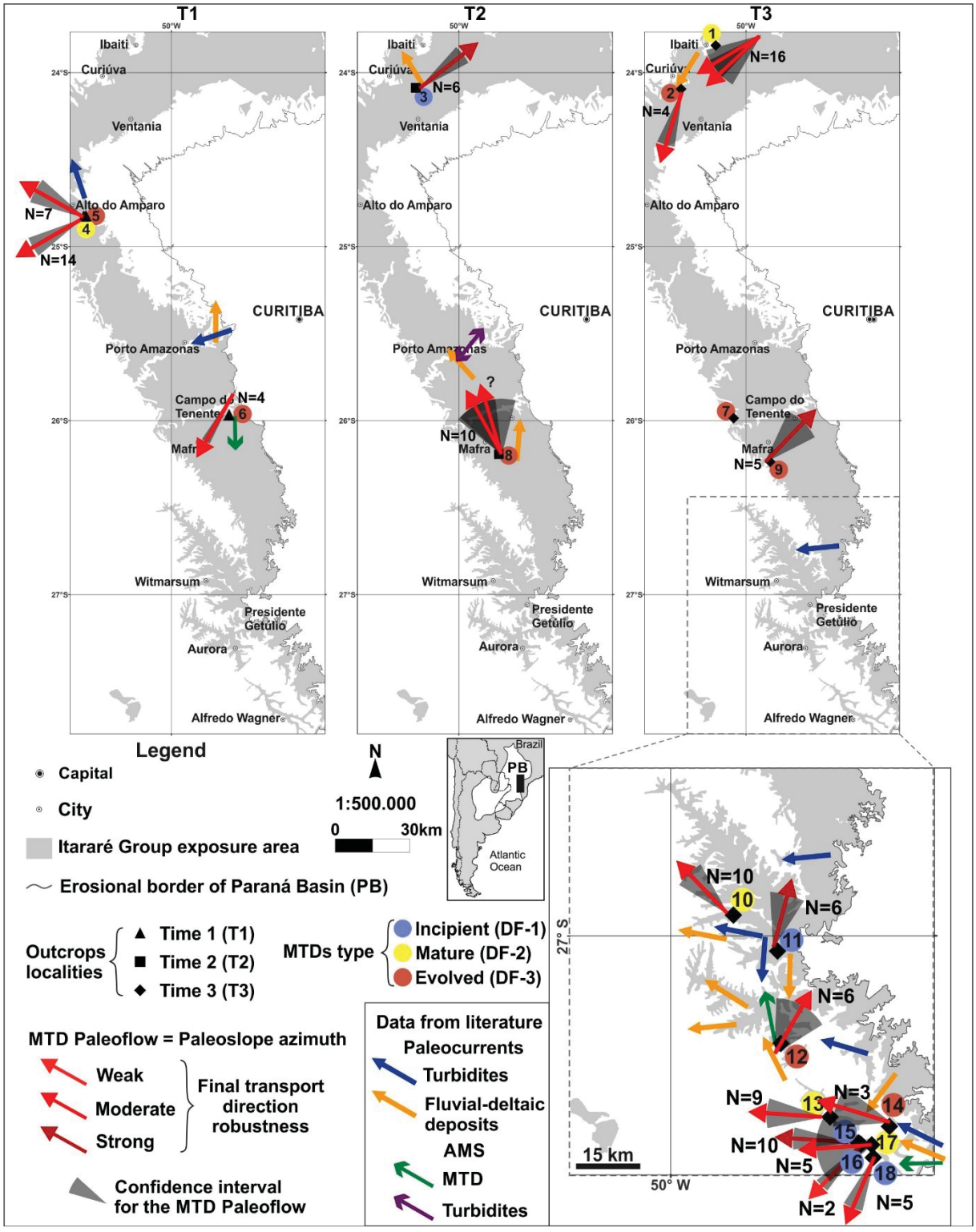

Fig. 4.9: Maps with the paleoflow of studied MTDs, in each stratigraphic level (T1 to T3) that correspond to the azimuth of the local paleoslope, with indication of confidence interval. N is the number of methods applied. Paleocurrents of fluvial deltaic deposits and turbidites described by several studies (e.g. Vesely and Assine, 2006; Beraldin, 2014; Suss et al., 2014; Juk, 2016; Amato, 2017; Carvalho and Vesely, 2017; Fallgatter and Paim, 2017; Mottin et al., 2018; Schemiko, 2018; Rosa et al., 2019) are also indicated in the maps.

4.8. DISCUSSION

4.8.1. MTD structures robustness

Since the pioneer study of paleoslope definition through of slump folds of Jones (1939) several studies have used folds and other soft-sediment structures generated by mass flow to define the orientation of paleoslope (e.g., Lewis, 1971; Woodcock, 1976a,b, 1979; Farrell, 1984; Maltman, 1984, 1994a,b; Bradley and Hanson, 1998; Debacker et al., 2001, 2009; Strachan and Alsop, 2006; Alsop and Marco 2011, 2012; Ogata et al., 2014; Sharman et al., 2015; Alsop et al., 2016; Sobiesiaki et al. 2016; Jablonská et al., 2018), some of these studies also have discusses the usefulness and robustness of several techniques (e.g., Woodcock, 1976a,b, 1979; Debacker et al., 2001, 2009; Strachan and Alsop, 2006; Alsop and Marco 2012; Sharman et al., 2015).

The structures orientation and kinematic within MTDs is commonly complex, which can complicate the MTD paleoflow definition and, therefore, the paleoslope definition. For instance, folds formation can be initiated at variable angles with respect to paleoslope azimuth (parallel, oblique and normal) and folds hinge and axial plane may be rotated during the mass flow toward the transport direction (e.g., Hansen, 1971; Woodcock, 1979; Farrell and Eaton, 1987; Strachan and Alsop, 2006; Alsop and Marco, 2011, 2012, 2013; Alsop et al., 2016). Further complications may include variable overprinting relationships between adjacent MTDs, variable slope or transport directions that may evolve with time, local backthrusts and folds verging up the palaeoslope (e.g. Alsop and Marco, 2011). Another complication that may be considered for incipient and evolved MTDs (DF-2 and DF-3, respectively) is disaggregation and mixing of remobilized sediments that tend to obliterate structures generated in earlier stages of the mass flow. Furthermore, MTDs paleoflow definition will also depend on the dataset sampling and, therefore, on the degree of exposure (e.g. Debacker et al., 2009).

Several studies indicate the application of many methods as possible to define the paleoslope from MTDs structures, so it would prevent misleading transport directions (e.g. Woodcock, 1979; Strachan and Alsop, 2006; Debacker et al., 2009; Alsop and Marco, 2012; Sharman et al., 2015). Besides applying several methods, the present study evaluated the robustness of structures datasets and the transport directions obtained from each structure through some parameters (number of data, preferential orientation, dataset confidence interval of 95%, number of methods and

confidence interval of 95% of the average transport direction) to better understand the reliability of the structure for the paleoslope definition.

The structures datasets and related transport direction have quite variable quality considering not just the robustness classification (Table 4.2, Appendixes 1 and 2), but also the confidence interval (95%; Appendixes 1 and 2) and the preferential orientation (Appendix 1). However, the datasets tend to show some preferential orientation (weak to very strong) and both structures datasets and transport direction tend to show moderate to strong robustness and confidence interval (95%) of about ± 20° or less (Fig. 4.3H, 4.4H, 4.5D, 4.6F and 4.7A and Appendix 1 and 2). The confidence interval consists of the range of values where the true mean orientation lies and tend to be influenced by the data dispersion and followed by the number of measurements (e.g., Woodcock and Naylor, 1983). So, the mean orientation vector for a dataset and the average transport direction by structures will be closer to the real mean orientation as the confidence interval (95%) is lower. Considering that most structures datasets and transport direction show confidence interval (95%) of ± 20° or less the mean orientation for these datasets can be considered more closer to the real mean orientation.

Fold have been the structure most commonly used in paleoslope definition and considered the most reliable (e.g., Jones, 1939; Woodcock, 1979; Bradley and Hanson, 1998; Strachan and Alsop, 2006; Debacker et al., 2009; Alsop and Marco, 2012; Ogata et al., 2014; Sharman et al., 2015; Alsop et al., 2016; Sobiesiak et al. 2016; Jablonská et al., 2018; Naji et al. 2018). While, faults are the second most commonly used structure to define paleoslope orientation (e.g., Farrell, 1984; Debacker et al., 2009; Ogata et al., 2014; Sharman et al., 2015; Alsop et al., 2016; Sobiesiak et al. 2016; Jablonská et al., 2016, 2018). Both folds and faults are common structures in MTDs and in this study were collected in 12 and 13 outcrop localities, respectively.

The average transport direction of folds, obtained from one or more methods, show confidence interval (95%) with similar range to the average transport direction of faults, also obtained from one or more methods. However, about 80% of folds average transport directions display confidence interval (95%) of less than ±20° (Fig. 4.3I), against just 56% of faults average transport direction (Fig. 4.4I). Although the transport direction of folds display better confidence than faults, datasets of faults and folds elements show similar degree of preferential orientation and confidence. In general,

the geometry complexity of folds and faults seems to not control the confidence interval (95%).

Both folds and faults also show roughly similar and variable datasets and transport direction robustness ranging from none to strong or very strong robustness (Table 4.2). The geometry of folds and associated complexity has apparently no influence on the robustness of the dataset or transport direction. Some datasets of different kinds of folds show similar robustness, such as the simple LPS upright symmetrical folds of locality 18 and the more complex LNS folds of locality 1 (Fig. 4.3A and D, respectively), both with (Appendix 1). But these two datasets show different transport direction robustness, locality 1 with strong robustness and locality 18 with moderate robustness (Appendix 2), which seems to be related to the number of methods applied rather the number of measuments. In its turn, the kink band folds of locality 15 (Fig. 4.3F) show strong robustness beside lower preferential orientation compare, for instance, to the folds of localities 13 and 18 with moderate robustness (Fig. 4.3A and C), which seems to be a result of larger dataset that compensated the mostly weak preferential orientation (Appendix 1). Although more complex folds (as from locality 1) tend to show weaker preferential orientation than more simple folds (as from locality 18), for the first case more methods can be applied than the second one. Besides the application of several methods be recommended (e.g., Debacker et al., 2009; Alsop and Marco, 2012; Sharman et al., 2015), the number of methods applied may control the confidence interval (95%). Although the robustness of folds shows no clear control by the geometry, the combination of the data dispersion (preferential orientation) and the number of measurements still important for the reliability of the results. Faults datasets and transport direction robustness seems to be controlled by the number of data and preferential orientation rather than the kinematic (normal, reverse or undefined; Appendix 1). Faults with simpler pattern tend to show better robustness, such as faults from the localities 10 (Fig. 4.4B), 15 (Fig. 4.4G) and 18 (Fig. 4.4A) compare to faults of locality 17 (Fig. 4.4C). However, for some simpler datasets (as from locality 18; Fig. 4.4A) less methods can be applied when compared to more complex datasets (as from locality 9; Fig. 4.9D), which may affect the robustness of the transport direction and its confidence interval (95%).

Between folds and faults, the second one seems to be easier to analyse and their methods can easily indicate a broad transport sense (cf. Debacker et al., 2009). Normal faults within the toe and central zone tend to be in high angles to transport

direction, but may also be generated parallel to flow (Alsop and Marco, 2011). Folds on the other hand may show complex orientation patterns and require more careful analysis and, even though it may result in more than one interpretation. This is related to several factors, such as variable angles of fold initiation, variable amounts of fold hinge and axial plane rotation, interaction between adjacent MTDs or second-order flow cells (see Alsop and Marco, 2014), variable slope or transport directions that may change with time (Alsop and Marco, 2011, 2012). We analysed the orientation of faults and folds with respect to each other using a different approach. For cases where folds show more than one possible interpretation, it was analysed the orientation with respect to normal and reverse faults that shows subparallel to parallel strike and preferential opposite dip direction. We considered that this arrangement of faults is more likely to represent the sense and direction of transport, where the fault strike is more or less parallel to paleoslope strike. This analysis allowed to reduce the possible interpretation for folds in the same locality, as well as, to define with more confidence the sense and direction of transport even in localities where just faults were identified.

Comparing the orientation of average transport direction of faults and folds from the same locality we verified a difference of orientation ranging from 1° to 89°, where 85% are less than 45° (23% is up to 10°; 54% between 10° and 30°; 8% between 40° and 50°; and 15% between 80° and 90°). This suggests that for most cases folds and faults indicate parallel to slightly oblique transport directions. and, so, the robustness of the transport direction obtained from each structure. Based on all these observations we conclude that, in general, folds and faults display similar quality and robustness. Difference of robustness between these structures should depend on sampling, which may affect the interpretation. Therefore, careful analysis of structures allows obtaining transport direction equally significant from both kinds of structures. However, as fold geometry is more complex than faults the selection of appropriated methods for paleoslope definition may be more difficult for folds than for faults.

The use of injectites to define transport direction of MTDs was also applied by Ogata et al. (2014). In our study, injectites show preferential orientation and quite good confidence interval (95%; ±20° or less; Fig. 4.5D). However, the confidence interval (95%) of transport direction from injectites ranges widely (Fig. 4.5E) due to complexity presented by some datasets. As the transport direction obtained from injectites depends on the interpretation and orientation with respect to other structures, it should be applied with caution to paleoslope definition and as a complementary

analysis. The injectites show weak to strong robustness despite the weak preferential orientation, which indicate none or low influence of the data dispersion (Table 4.2 and Appendix 1). Instead, the robustness of injectites datasets is also associated to the number of measurements.

Once bedding may also reflect the paleoslope orientation (Jones, 1939; Sharman et al., 2015). Based on that bedding and banded matrix orientation was also analysed. Both bedding and banded matrix show confidence interval (95%) up to ±20°, but bedding tend to show better preferential orientation than banded matrix (Fig. 4.7A). In terms of robustness, bedding and banded matrix tend to show datasets with moderate to strong robustness, while the transport direction robustness is moderate for banded matrix and range from moderate to strong for bedding. This difference between bedding and banded matrix datasets tend to be followed by moderate and weak preferential orientation, respectively (Table 4.2 and Appendix 1). The weak preferential orientation of the banded matrix datasets is possible related to the nature of the structures, which results of deformation and modification of the original bedding. While the bedding datasets with weak preferential orientation seems to be related the data dispersion due to deformation, such as folds associated to diapirs (locality 3; Appendix 1), LNS folds (locality 4; Appendix 1) and normal faults (locality 7; Appendix 1). In some cases, the dispersion of data was compensated by large number of data allowing to classify the dataset with strong robustness (e.g., locality 3; Appendix 1). However, when compared bedding and banded matrix transport direction to other structures transport direction (or average transport direction), both show sometimes considerable difference of orientation (Fig. 4.7B). Although the difference that bedding and banded matrix transport direction may show with respect to other structures, in the studied cases the use of the mean orientation of bedding or banded matrix (MBSM) resulted in little or no significantly change in the final transport direction and its confidence interval (95%; Fig. 4.7C-E). In some localities, tilted bedding and banded matrix may be the main features indicative of deformation in the MTD. Therefore, we suggest that the application of MBSM should be done with caution, and preferentially with the incorporation of other structures, as complementary method in paleoslope definition.

For the other structures analysed, such as boudins, intrastratal slickenlines, oriented clasts and grooves and stretch marks, no robustness trend was defined due to the limited datasets collected by structure (Table 4.2 and Appendix 1). Between

these structures boudins seems to be the more reliable with moderate preferential orientation, moderate dataset robustness and transport direction with strong robustness and confidence of interval (95%) about ±10°. The other structures show confidence interval (95%) between ±15 and ±25°, weak preferential orientation, datasets and transport direction with weak to moderate robustness, of which the number of measurements tend to compensate the dispersion (Table 4.2, Appendix 1 and 2). The weak preferential orientation of the oriented clasts and grooves and stretch marks in clasts borders it is possible related to the nature of these structures. These features described are related to clasts dispersed in matrix (diamictite) and, therefore, the data orientation depends on how shear is distributed within the matrix and how it affects the clasts (e.g., Ogata et al., 2014; Sobiesiak et al., 2016). However, paleoflows indicated by boudins, intrastratal slickenlines, oriented clasts and grooves and stretch marks are reasonably consistent and in agreement with transport direction from folds and faults in the same MTDs. In most cases, their analysis may be an important complementary method for paleoslope definition, or even the main method in case of lack of folds and faults, as in some evolved MTDs (DF-2 and 3).

4.8.2. MTDs paleoflow robustness

Beside the indication of the application of as many methods as possible to define the paleoslope from MTDs structures (e.g. Woodcock, 1979; Strachan and Alsop, 2006; Debacker et al., 2009; Alsop and Marco, 2012; Sharman et al., 2015) some studies have concluded that the analysis of more than one kind of structures also improves the reliability of paleoslope definition (e.g. Debacker et al., 2009; Sharman et al. 2015). The analysis of more than one kind of structure also imply that more different methods are applied. Through a careful analysis of geometry, spatial relationship and kinematics of the structures and the application of several methods at the same locality it was possible to obtain reasonable transport directions, which show mostly good confidence (70% with confidence interval 95% of ±20° or less; Fig. 4.8) and moderate to strong robustness (more than 90%; Appendix 2). A similarity of paleoflow orientation in different localities of the same stratigraphic level as well as between some of our results and paleoflow orientation obtained through AMS by Amato (2017) reinforces the applicability of this kind of study on paleoslope definition (Fig. 4.9).

Comparing the final transport direction for each locality (MTD paleoflow) with some paleocurrents data of associated deposits (turbidites and fluvial-deltaic deposits)

from literature (Vesely and Assine, 2006; Suss et al., 2014; Fallgater, 2015; Juk, 2016; Carvalho and Vesely, 2017; Fallgatter and Paim, 2017; Mottin et al., 2018; Schemiko, 2018) was also verified some similarity of orientation. Although the orientation of a MTD paleoflow may not be necessarily the same to other deposits paleocurrents in a basin, the combination of all this observation may be considered as a indicative of quite reliability of the results obtained.

4.8.3. MTD paleoflow meaning and role as a paleogeograhic tool

Even though several studies have defined paleoslope orientation using MTD structures (e.g. Farrell, 1984; Farrell and Eaton, 1987; Martinsen, 1989; Strachan and Alsop, 2006; Debacker et al., 2009; Alsop and Marco, 2012; Sharman et al., 2015; Alsop et al., 2016; Jablonská et al., 2016, 2018; Naji et al. 2018), just a few studies have integrated MTD structures with paleocurrents of associated deposits to better define paleoslopes and their paleogeographic implications (e.g. Strachan and Alsop, 2006; Fig. 4.10). Where a MTD is well-exposed the collection of data of different parts within this same MTD may allow a consistent definition of paleoslope based on MTD structures only. However, where MTDs are exposed in disconnected outcrops, as is the case for the present study, data collection from the same stratigraphic level (i.e. the same MTD complex) and comparison with paleocurrents from associated deposits should give the best results. The orientation of structures within MTD may varies widely (e.g. Sharman et al. 2015) and therefore the paleoslope definition through one MTD must be conduct carefully. Besides this, the paleoslope azimuth indicated by a MTD may or not represent the main orientation of a paleoslope, once a MTD paleoflow orientation may be controlled by the paleoslope and see floor topography (e.g. Alves and Cartwright, 2009; Dalla-Valle et al., 2015). Considering these observations, the MTDs paleoflow obtained are considered to represent the local paleoslope orientation.

As the structural framework of the Paraná Basin at the time the Itararé Group was deposited (T1 to T3) is poorly known, on what extent the examined MTDs correspond to local or regional paleoslopes is difficult to define. In general, our results show that MTDs from the same stratigraphic level and same region have similar orientation, as, for instance, in the northern portion of the studied area during T1 (Fig. 4.9, localities 4 and 5) and T3 (Fig. 4.9, localities 1 and 2), and in the southern portion during T3 (Fig. 4.9, localities 10-12 and 13-18). However, within these groups of MTDs

that indicates a general orientation for a given region, local variation of paleoflow orientation is also observed. According to previous work, this can be due to different situations such as: 1) irregular paleoslope and sea-floor topography (Fig. 4.10) associated with irregular morphology of previously deposited MTDs (e.g. Amerman et al., 2011; Alsop and Marco, 2014; Alves, 2015), presence of tectonic features like folds and faults (Dalla Valle et al., 2015) or salt tectonics (Alves and Cartwright, 2010); 2) variable orientation of the head scarp with respect to the intra-basinal slope gradient (Jablonská et al., 2016); 3) limitation of MTDs exposure resulting in non-representative dataset; 4) difference of flow direction indicated by folds and thrusts at the lateral portions of MTDs (e.g. Alsop and Marco, 2012, 2013) or due to fan out of structures around the toe of MTDs (e.g. Strachan and Alsop, 2006; Alsop et al., 2016); 5) variable angles of fold initiation; 6) fold hinge and axial-planar rotation; 7) overprinting between deformation of adjacent MTDs or MTDs cells flow (Alsop and Marco, 2012, 2014). Here, we infer that variations are possible related to the limited degree of exposure and fan-out or spreading characteristic of MTDs, once lateral zones of MTDs weren't identified.

At the regional scale, significant variation of paleoslope orientation can be verified in the same time interval. This is clearer in T3 (larger dataset), where three groups of paleoflow patterns can be observed, being, from south to north: to the west (localities 13 to 18), to the northwest and northeast (localities 9 to 12) and to the southwest. Paleoslopes dipping to the W and SW fit well with a depocenter located in Santa Catarina state at that time (Rio do Sul sub-basin), where isopachs of T3 (Rio do Sul-Taciba Formation) reach a maximum. This is also in agreement with fluvial/deltaic paleocurrent patterns, indicating a nice relationship between shoreline progradation and subaqueous slope development (Fig. 4.10A, 4.10B, 4.10D and 4.10E). However, MTD paleoflows to the north (NW and NE) seem to reflect local changes in mass flow paths, which could be related to some topographic control (Fig. 4.10F).

Although there is some coincidence between MTD paleoslopes and paleocurrent direction (localities 1, 2, 4, 5, 8 and 9; Fig. 4.9), in some cases these two different types of data show some divergence. This is the case, for instance, of locality 3 (Fig. 4.9 – T2), where diapiric folds verge to the NE and paleocurrents from immediately above it go to the NW. This may be related to a limited amount of data and/or the nature of diapiric folds that may not indicate well the paleoslope because they represent local shear stresses also influenced by loading. In locality 6 (T1), the

MTD displays an oblique to almost opposite transport direction with respect to fluvial-deltaic paleocurrents. This divergence may be a result of regional control related to tectonics (e.g. Dalla-Valle et al., 2015) or local topographic control (e.g. Amerman et al., 2011; Alsop and Marco, 2014; Alves, 2015). Considering the first hypothesis, the direction of fluvial sediment input may be near perpendicular to the dip azimuth of subaqueous slopes in elongated, structurally-controlled basins that are fed both laterally and axially (e.g. Mutti et al, 2003). In the second case, it should be noted that the MTD of locality 6 is a matrix-rich diamictite formed at the final stages of mixing and homogenization of the flow (evolved, DF-3 type). In evolved mass flows, the transport direction may lose the influence of paleoslope azimuth and reorient because of sea-floor topography or depocenter location (Fig. 4.10G; e.g. Gee et al., 1999; Bull et al., 2009; Alves and Cartwright, 2010). Therefore, the type of MTD (incipient, mature and evolved) and its paleoflow relationship with paleocurrents of associated deposits may indicate if the MTD represent the more proximal or distal portions of the paleoslope system (Fig. 4.10). The majority of incipient and mature MTDs described herein has paleoflows similar to paleocurrents of associated fluvio-deltaic deposits, as, for instance, in DF-1 MTDs of localities 15, 16 and 18 (Fig. 4.9). Evolved MTDs, on the other hand, are more variable, meaning that their transport direction may indicate the influence of seafloor topography and not necessarily the parental paleoslope.

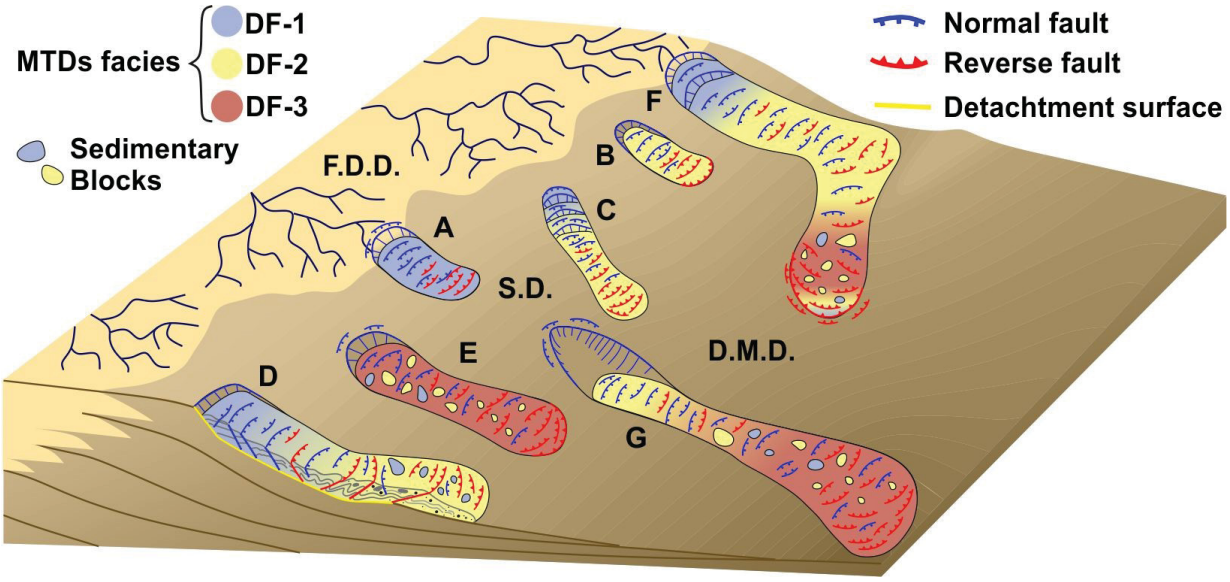

Fig. 4.10: Schematic block diagram that indicate some of the possible orientations of MTDs paleoflow with respect to the paleoslope main orientation and the depocenter, as well as, some possible morphological controls in the paleoslope and sea floor. The possible relationship between amount of transport and MTDs evolution related to

homogenization is indicated by deformational facies (DF-1, DF-2 and DF-3 – incipient, mature and evolved MTDs respectively). A) and B) Incipient and mature MTDs, respectively, with general paleoflow orientation parallel to main paleoslope orientation. C) Incipient to mature MTD with paleoflow oblique to main paleoslope orientation. D) and E) Incipient to mature MTD and evolved MTD, respectively, with general paleoflow orientation parallel to main paleoslope orientation. F) Incipient to evolved MTD with proximal portion paleoflow orientation parallel to main paleoslope orientation and distal portion reoriented by structural high. G) Mature to evolved MTD with proximal portion paleoflow orientation parallel to main paleoslope orientation and distal portion reoriented toward the basin depocenter. F.D.D. are fluvial-deltaic deposits; S.D. are slope deposits; and, D.M.D. are deep-marine deposits.

4.9. CONCLUSIONS

From the study of deformational structures of MTDs of Itararé Group we were able to evaluate their use in paleoslope definition in cases of limited exposure. As well as, we were able to define local paleoslope orientation for each locality, indicate some implications for the paleogeography and enhance some ongoing discussions about the Paraná Basin evolution during the deposition of Itararé Group.

- Through careful analysis of geometry and orientation of deformational structures generated in mass gravity-induced flows is possible to define the orientation of paleoslope (and/or sea floor). However, the data of deformational structures of MTDs with limited exposure is considered here to indicate the orientation of paleoslope in a local scale.
- Faults and folds datasets provided paleoslope azimuth with quite similar robustness when present in the same locality. However, their potential for this kind of study depend on the complexity of the data collected, which may turn difficult the comprehension of the geometry and orientation of the structure.
- Beside faults and folds, the data of orientation and/or kinematics of other structures (such as boudins, oriented intrabasinal and extrabasinal clasts, quarter structures, and others) may help to understand the flow and to define the paleoslope avoiding ambiguous interpretations given sometimes by folds or faults. For studies of MTDs with limited exposure the sampling of many structures as possible may be essential. In mature MTDs (DF3), other structures may be the only indicators of the flow. In studied cases, these others structures display reasonably good robustness for paleoslope definition.
- The analysis of MTDs structures through as many methods as possible and the robustness evaluation of the datasets and transport direction results allow us to define

local paleoslope azimuths for different localities in different stratigraphic levels of Itararé Group with quite reliability. The MTDs paleoflow combined with the paleocurrents allows to indicate some general patterns for the paleoslope. For T1 a general orientation of paleoslope toward W can be indicated, while for T2 the paleoslope can be indicated a general orientation toward N. At the north of the studied MTDs paleoflow of T3 indicates a general orientation toward SW. While at the south portion, MTDs paleoflow indicates that from S to N of the subregion the paleoslope orientation ranges from SW to NNE, with a general orientation toward W. The MTDs paleoflow results also indicates change of Itararé Group paleoslope during the time.

- For paleogeography studies is recommended the analysis of several MTDs, regardless of exposure, that occur in a same stratigraphic interval in a certain region. Through the information of several MTDs is possible to define more properly the main orientation of the paleoslope. As well as, some local variation in paleoslope orientation and its possible controls. The paleoflow of MTDs may also indicates variation of sea floor morphology and the orientation of the paleoslope with respect to the depocenter of the basin, when compared to others kinds of data (such as paleocurrents of associated deposits, isopach maps, tectonic structures and others).

5. CONSIDERAÇÕES FINAIS

5.1. DEFORMAÇÃO EM DEPÓSITOS DE TRANSPORTE EM MASSA

Diferentes produtos de deformação associada a fluxos gravitacionais em massa foram identificados nos MTDs estudados, tais como dobras, falhas, boudins, blocos, matriz, entre outros. Com base na comparação entre a proporção de matriz e assembleia de estruturas os MTDs estudados foram agrupados em três fácies deformacionais: 1) DF-1 que é caracterizada pela ausência de matriz, acamamento bem preservado com estruturas sedimentares e assembleia de estruturas consistindo principalmente de dobras, falhas e *boudins* simétricos; 2) DF-2 que apresenta menos de 50% de matriz, que pode ser heterogênea (bandada) ou homogênea (maciça), e estruturas como dobras, falhas, *boudins* simétricos e assimétricos, injetitos e outras feições indicativas de cisalhamento, como estruturo tipo em quadrante; e 3) DF-3 que é caracterizada por mais de 50% de matriz heterogênea (bandada) a homogênea (maciça), estruturas deformacionais como dobras, falhas, *boudins*, injetitos e outras feições indicativas de cisalhamento, além de blocos sedimentares (arenitos a ritmitos) que mostram deformação nas bordas e podem apresentar deformação interna.

Através da relação entre os produtos deformacionais foram identificados alguns padrões de deformação que se relacionam com o processo de desagregação e mistura de sedimentos que leva a homogeneização de sedimento remobilizados por fluxos em massa. Os MTDs caracterizados por DF-1 foram denominados MTDs incipientes e interpretados como resultantes de fluxos em massa pouco evoluídos ou incipientes devido a baixa diversidade de estruturas e falta de matrix. Na DF-1 os processos de falhamento e boudinagem permitiram alguma ruptura das camadas. Os MTDs caracterizados por DF-2 foram denominados MTDs maduros e interpretados como produto de evolução intermediária, pois mostra aumento de desagregação e mistura dos sedimentos, variada deformação. Nestes MTDs estruturas deformacionais iniciais, acamamentos e estruturas sedimentares estão preservadas. Na DF-2 a ruptura de camadas e desagregação de sedimentos se relaciona com processos de falhamento, boudinagem e outras processos de cisalhamento; enquanto que o cisalhamento em escala de laminação e a fluidização auxiliam no processo de mistura dos sedimentos. Por sua vez, MTDs caracterizados por DF-3 foram denominados MTDs evoluídos devido alto conteúdo de matriz e grande variedades de produtos deformacionais. Na DF-3 processos como falhamento e boudinagem de blocos

sedimentares, bem como a deformação nas bordas desses blocos, são os principais processos relacionados a desagregação e ruptura. O cisalhamento nas bordas de blocos, fragmentos menores e da própria matriz permitem a mistura dos sedimentos na DF-3. Nessas fácies a deformação interna observada em blocos sedimentares indicam processos iniciais de deformação, enquanto as deformações nas bordas indicam a progressiva contínua assimilação de sedimentos dos blocos pela matriz.

Todas as fácies deformacionais foram identificadas nos MTDs que compõem um MTC no intervalo superior de T3, no setor sul da área de estudos. Estes MTDs estão geneticamente associados em clinoformas progradacionais a depósitos flúvio-deltáicos. A partir da relação com depósitos associados verificou-se que os MTDs incipientes a parte dos MTDs maduros ocorrem em porções proximais do paleotalude associados aos depósitos de frentes deltaicas. Essa interpretação é reforçada pela presença de feições fácies deltáicas preservadas nestes MTDs. Enquanto que alguns MTDs maduros e os MTDs evoluídos ocorrem em porções relativamente mais distais do paleotalude associados a depósitos de pró-delta e marinho profundo. Nestes MTDs também foram observados em camadas ou blocos de fácies deltaicas. Esta relação observada entre os diferentes de fácies deformacionais em um MTC foi associada com deformação progressiva (desagregação e mistura) dos sedimentos remobilizados, pouco ou não litificados, talude a baixo. A deformação progressiva é evidenciada pela composição similar entre matriz e blocos, deformação interna dos blocos que registram fases iniciais da deformação e deformação na borda dos blocos.

5.2. IMPLICAÇÕES PARA A PALEOGEOGRAFIA DO GRUPO ITARARÉ

Uma vez que o fluxos de MTDs indica a orientação do paleotalude ou mesmo a morfologia do fundo marinho (e.g. Farrell 1984, Martinsen 1989, Alves & Cartwright 2010, Alsop & Marco 2012, Dalla Valle et al. 2015, Sharman et al. 2015, Alsop et al. 2016, Jablonská et al. 2018), sua cinemática pode auxiliar a entender a paleogeografia e a evolução da bacia se integrada com outras informações, tais como paleocorrentes, isópacas, estruturas regionais, entre outras. Consequentemente, os resultados deste estudo podem trazer alguma luz sobre a evolução paleogeográfica de parte da Bacia do Paraná durante o intervalo do Carbonífero ao Permiano Inferior.

Durante T1, depósitos fluvio-deltaicos e turbiditos registram paleocorrentes para norte, noroeste e localmente oeste-sudoeste (e.g. Vesely & Assine 2006, Beraldin 2012, Juk 2016, Rosa 2018) indicam proveniência sedimentar preferencialmente de área localizadas a S e SE (Fig. 5.1A – T1). Um depocentro principal à NW é sugerido pelo mapa de isópacas de T1-equivalente a Formação Lagoa Azul (França & Potter 1988), que indicaria um gradiente deposicional mergulhando nesta direção na área de estudo. Paleofluxos de MTD para NWpara este interval no setor centro-noroeste são de alguma forma equivalente. Desvio para SW poderam ser resultado de mudanças locais no fluxo devido à natureza madura a evoluída dos depósitos. Porém, como isso ocorre em diferentes localidades um depocentro secundário a oeste é mais plausível. O MTD com paleofluxo para SSW (resultados de AMS de Amato 2017) pode também indicar alguma mudança local do azimute do paleotalude, o qual pode ter sido controlado tectonicamente devido a bloco basculado ou falhamento. França & Potter (1988) sugerem que a deposição da Formação Lagoa Azul foi influenciada por complexidades estruturais controladas por zonas de falhas NE e NW herdadas do embasamento, as quais podem ter controlado paleotaludes locais.

Paleocorrentes em T2 tem um consistente azimute médio para NW (e.g. França et al. 1996; Vesely & Assine, 2006; Carvalho & Vesely, 2017), mas algumas mudanças na geometria da bacia são sugeridas pelo mapa de isópacas da Formação Campo Mourão (França & Potter, 1988) e paleofluxos de MTDs registrado no estudo (Fig. 5.1A – T2). Apesar de um fluxo geral para norte também é observado nos MTDs de T2, os paleotaludes parecem desviar para um depocentro a NE (thicknesses > 600 m). A Formação Campo Mourão (T2) é a mais arenosa dentre os três intervalos devido ao predomínio de depósitos proximais ricos em areia (continentais a transicionais) nesta unidade (e.g. Carvalho & Vesely 2016). Neste caso, parece plausível considerer que os palotaludes indicados pelos MTDs refletem melhor a configuração da bacia durante este intervalo do que as paleocorrentes.

Para T3 as paleocorrentes de depósitos flúvio-deltaicos (e.g. Suss et al. 2014, Fallgatter 2015, Fallgatter & Paim 2016, Amato 2017, Schemiko 2018, Mottin et al. 2018), isópacas da Formação Taciba (França & Potter 1988) e paleofluxo de MTDs definidos neste estudo indicam mudanças significantes na paleogeografia (Fig. 5.1A – T3), um fato que tem sido sugerido por estudos mais recentes (e.g. Mottin et al. 2018). No setor norte da área estudada depósitos flúvio-deltáicos e de leques de

outwash mostram paleocorrentes para sudoeste (Mottin et al. 2018) que concordam com os paleofluxos dos MTDs (Fig. 5.1A – T3). Com base nisto, Mottin et al. (2018) indicam uma fonte glacial a nordeste corroborada por paleodireções de fluxo de gelo a norte (Santos et al. 1996, Rocha-Campos et al. 2000) e litofácies com distribuição em escala de bacia baseado em poços de exploração (França & Potter, 1988; Eyles et al., 1993). Isto mostra uma importante mudança no padrão de dispersão de sedimentos de T2 para T3 (Mottin et al. 2018). O padrão de dispersão para sudoeste se mantém na região durante a deposição pós-glacial da Formação Rio Bonito indicado por paleocorrentes fluviais para sudoeste (Assine et al. 2003, Zacharias 2004, Zacharias & Assine 2005) e associada com a migração do depocentro para sul devido a atividades tectônicas (e.g. Milani 1997). Este depocentro a sul também é indicado pelas isópacas (Fig. 5.1A – T3).

No setor sul da área de estudo padrões de paleotalude e paleocorrentes de T3 estão melhor restringidos devido ao conjunto de dados maior. Nós sugerimos uma direção geral N-S para o paleotalude na região e com azimute de mergulho para oeste e um depocentro principal a noroeste (Fig. 5.1A – T3 e 5.1B). Isto é indicado pelo paleofluxo dos MTDs, pelas paleocorrentes (Fallgatter 2015, Fallgatter & Paim 2016, Amato 2017, Schemiko 2018) e pelas isópacas da Formação Taciba (França & Potter, 1988). Variações gerais do paleofluxo dos MTds e paleocorrentes de depósitos associados de sudoeste para noroeste podem estar associadas avariações locais da orientação do paleotalude (Fig. 5.1B). Os MTDs e depósitos associados de T3 podem ser divididos em dois intervalos de tempo menores (T3.1 e T3.2 da base para o topo) separados por uma superfície de inundação máxima materializada no folhelho Lontras (e.g. Schemiko 2018). Durante T3.1, turbiditos com paleofluxos para noroeste (Fig. 5.1B – T3.1) tiveram algum controle local por paleovales com orientação noroeste (Fallgatter 2015, Fallgatter & Paim 2016) em localidades proximais a sudeste. Mais a norte, os turbiditos tendem a mostrar paleocorrentes para oeste em direção ao depocentro; enquanto mais localmente turbiditos com paleocorrentes para sul e MTDs com paleofluxo para para norte permitem sugerir variações no azimute do paleotalude de sul para norte associada com alguma possível protuberância em direção ao depocentro (Fig. 5.1B – T3.1). Durante T3.2 depósitos flúvio-deltáicos mostram paleocorrentes com direção principal para oeste, variando de sul para noroeste (Fig. A – T3 e B – T3.2). Mais a sul da área, este trend para oeste está em concordância com paleofluxos de MTDs, que incluem principalmente MTDs incipientes (DF-1) e

maduros (DF-2) que são menos evoluídos em termo de homogenização. Por isso, consideramos que estes paleofluxos indicam porções mais proximais do paleotalude. Alguns destes MTDs podem ter sido convertidos em fluxos mais homogenizados (DF-3 – MTD evoluído). Como os MTDs são transportados talude abaixo a orientação do seu paleofluxo pode representar alguma mudança local relacionada a topografia que pode ter sido controlada por falhas (Fig. 5.1B – T3.2). Na porção central da região discutida os paleofluxos dos MTDs são considerados representativos da orientação principal do paleotalude e da localização do depocentro (e.g. localidade 12; Fig. 5.1B – T3.2). Enquanto que o paleofluxo do MTD na localidade 9, mais a norte, possivelmente representa a orientação do depocentro, possivelmente foi controlada por falhas NE-SW, do que o azimute do paleotalude (Fig. 5.1B – T3.1). Este paleofluxo de MTD em direção a nordeste pode também indicar alguma conexão entre os dois depocentros na área de estudo indicados pelo mapa de isópacas da Formação Taciba de França & Potter (1988) e outros dados (Fig. 5.1A – T3).

Algumas variações da orientação do paleotalude comparada a orientação de falhas regionais sugerem que falhas podem ter controlado a orientação pelo menos localmente durante a deposição do Grupo Itararé (Fig. 5.1A). Este possível controle é mais claro em T3 na porção sul da área de estudo onde mais dados estão disponíveis (Fig. 5.1B). As mudanças na orientação do paleotalude e localização dos depocentros entre os três intervalos de tempo discutidos podem indicar ainda que algumas falhas estavam ativas durante a deposição do Grupo Itararé. Diversos estudos indicam a influência de estruturas do embasamento, principalmente NE-SW e NW-SE, na sedimentação do Permocarbonifero (e.g. Fúlfaro et al. 1982, Ferreira 1982, Zalán et al. 1987, França & Potter 1988, Soares 1991, Eyles et al. 1993, Milani 1997, Rostirolla et. al. 2000, 2003, Riccomini et al. 2005). Contudo, mais estudos de detalhe são necessários para verificar esta possível relação entre a variação da orientação do paleotalude e feições tectônicas.

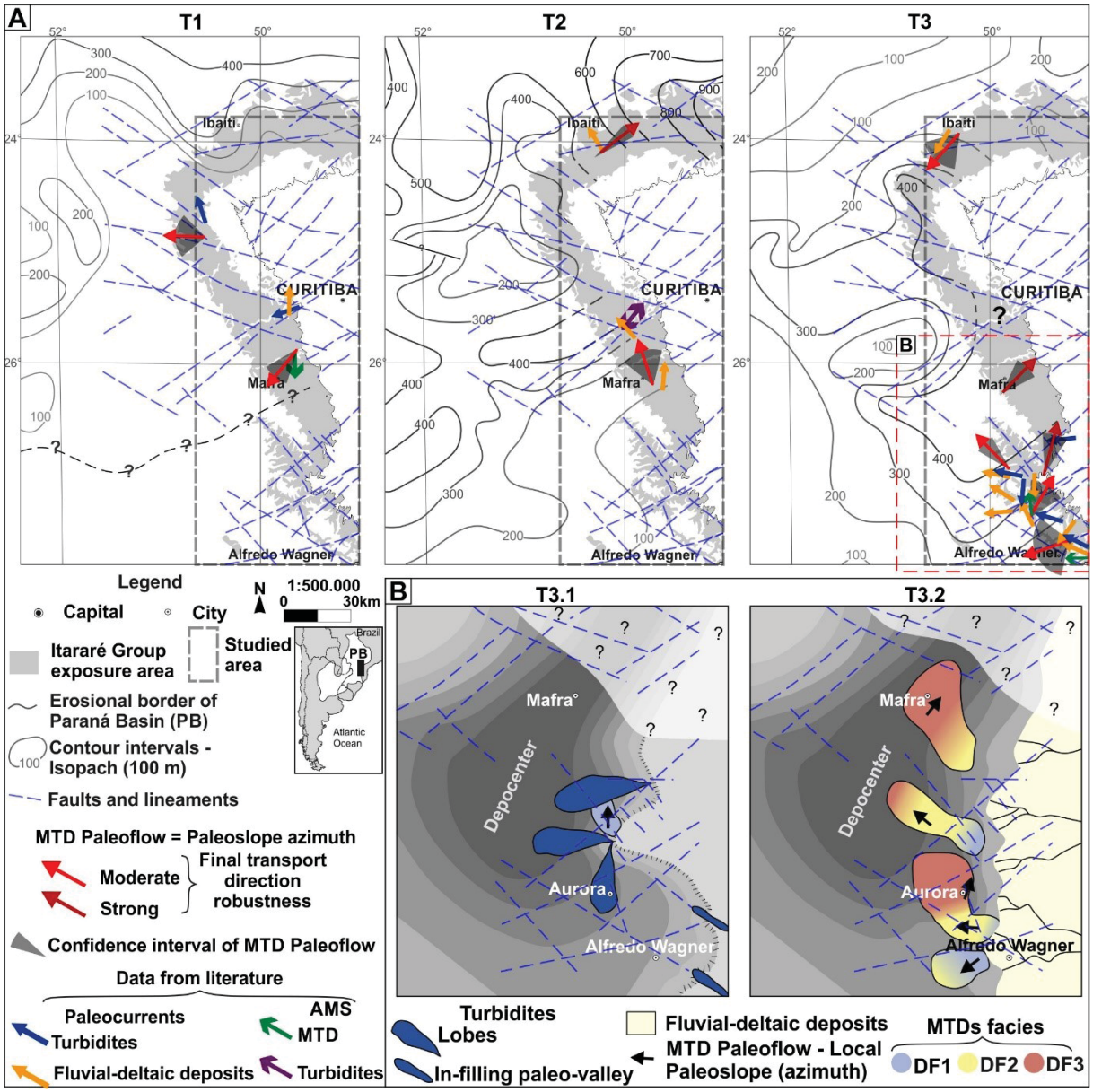

Fig. 5.1: A) Mapas dos três intervalos de tempo do Grupo Itararé (T1, T2 e T3) com área extendida a partir da área de estudo. Estes mapas mostram a orientação dos paleofluxos dos MTDs (alguns integrados para simplificar), paleocorrentes de depósitos associados (dados da literatura; ver texto), falhas (CPRM 2004) e isópacas das formações Lagoa Azul, Campo Mourão e Taciba (adaptado de França & Potter 1988; respectivamente T1, T2 e T3). B) Paleogeografia do setor sul da área de estudo durante T3 dividida em dois intervalos de tempo menores (da base para o topo - T3.1 e T3.2) com indicação do depocentro principal. Durante T3.1 foram depositados um dos MTDs estudados e turbiditos. Enquanto durante o T3.2 foram depositados depósitos flúvio-deltáicos e a maioria do MTDs estudados.

REFERÊNCIAS

ALLEN, J.R.L. Sedimentary Structures; Their Character and Physical Basis, Volume I: Amsterdam, Elsevier Science Publishers, Developments in Sedimentology 30, 593 p, 1982.

ALLMENDINGER, R.W.; CARDOZO N.C.; FISHER D. **Structural geology algorithms: vectors and tensors.** Cambridge, England, Cambridge University press, 289 p, 2013

ALMEIDA, F.F.M. A "Roche Moutonnée" de Salto, Estado de São Paulo. **Boletim Geologia e Metalurgia**, 5: 112-118, 1948.

ALSOP, G.I.; CARRERAS, J. Structural evolution of sheath folds: a case study from Cap de Creus. **Journal of Structural Geology**, 29: 1915-1930, 2007.

ALSOP, G.I.; HOLDSWORTH, R.E. The distribution, geometry and kinematic significance of Caledonian buckle folds in the western Moine Nappe, northwest Scotland. **Geological Magazine** 130, 353-362, 1993.

ALSOP, G.I.; HOLDSWORTH, R.E. The geometry and kinematics of flow perturbation folds. **Tectonophysics**, 350: 99-125, 2002.

ALSOP, G.; HOLDSWORTH, R. Shear zone folds: records of flow perturbation or structural inheritance? Geological Society, London, Special Publications 224, 177–199, 2004. https://doi.org/10.1144/GSL.SP.2004.224.01.12

ALSOP, G.I.; HOLDSWORTH, R.E; MCCAFFREY, K.J.W. Scale invariant sheath folds in salt, sediments and shear zones. **Journal of Structural Geology**, 29: 1585-1604, 2007.

ALSOP, G.I.; MARCO, S. Soft-sediment deformation within seismogenic slumps of the Dead Sea Basin. **Journal of Structural Geology**, 2011. https://doi.org/10.1016/j.jsg.2011.02.003

ALSOP, G.I.; MARCO, S. A large-scale radial pattern of seismogenic slumping towards the Dead Sea Basin. **Journal of the Geological Society** 169, 99–110, 2012. https://doi.org/10.1144/0016-76492011-032

ALSOP, G.I.; MARCO, S. Seismogenic slump folds formed by gravity-driven tectonics down a negligible subaqueous slope. **Tectonophysics** 605, 48–69, 2013. https://doi.org/10.1016/j.tecto.2013.04.004

ALSOP, G.I.; MARCO, S. Fold and fabric relationships in temporally and spatially evolving slump systems: A multi-cell flow model. **Journal of Structural Geology** 63, 27–49, 2014. https://doi.org/10.1016/j.jsg.2014.02.007

ALSOP, G.I.; MARCO, S.; WEINBERGER, R.; LEVI, T. Sedimentary and structural controls on seismogenic slumping within mass transport deposits from the Dead Sea Basin. **Sedimentary Geology** 344, 71–90, 2016. https://doi.org/10.1016/j.sedgeo.2016.02.019

ALSOP, G.I.; MARCO, S.; LEVI, T.; WEINBERGER, R. Fold and thrust systems in Mass Transport Deposits. **J. Struct. Geol.** 94, 98–115, 2017. https://doi.org/10.1016/j.jsg.2016.11.008

ALVES, T.M. Submarine slide blocks and associated soft-sediment deformation in deep-water basins: A review., **Marine and Petroleum Geology**, 2015.

https://doi.org/10.1016/j.marpetgeo.2015.05.010

ALVES, T.M.; CARTWRIGHT, J.A. Volume balance of a submarine landslide in the Espírito Santo Basin, offshore Brazil: quantifying seafloor erosion, sediment accumulation and depletion. **Earth Planet. Sci. Lett.**, 2009. doi:10.1016/j.epsl.2009.10.020

ALVES, T.M.; CARTWRIGHT, J.A. The effect of mass-transport deposits on the younger slope morphology, offshore Brazil. **Marine and Petroleum Geology** 27, 2027–2036, 2010. https://doi.org/10.1016/j.marpetgeo.2010.05.006

ALVES, T.M.; LOURENÇO, S.D.N. Geomorphologic features related to gravitational collapse : Submarine landsliding to lateral spreading on a Late Miocene – Quaternary slope (SE Crete, eastern Mediterranean). **Geomorphology** 123, 13–33, 2010. https://doi.org/10.1016/j.geomorph.2010.04.030

AMERMAN, R.; NELSON, E.P.; GARDNER, M.H.; TRUDGILL, B. Submarine mass-transport deposits of the Permian Cutoff Formation, west Texas, U.S.A.: Internal architecture and controls on overlying sand deposition, In: Shipp, R. C., Weimer, P., and Posamentier, H. W., eds., Mass-Transport Deposits in Deepwater Settings, SEPM Special Publication 96: Tulsa, Oklahoma, SEPM (Society for Sedimentary Geology), p. 235–267, 2011.

AMATO, J.A. Using ams to help interpret glaciogenic deposits of the Late Paleozoic Ice Age in the Paraná Basin, Brazil. Master degree thesis, The University of Wisconsin-Milwaukee, USA, 146p, 2017.

AQUINO, C.D.; VALDEZ B.V.; FACCINI, U.F.; MILANA, J.P.; PAIM, P.S.G. Facies and depositional architecture according to a jet efflux model of a late Paleozoic tidewater grounding line system from the Itararé Group (Paraná Basin), southern Brazil. **Journal of South American Earth Sciences**, 67: 180-200, 2016.

ARAB, P.B.; PERINOTTO, J.A.J.; ASSINE, M.L. Grupo Itararé (P–C da Bacia do Paraná) nas regiões de Limeira e Piracicaba-SP: contribuição ao estudo das Litofácies. **Geociências** 28(4), 501-521, 2009.

ARMITAGE, D.A.; ROMANS, B.W.; COVAULT, J.A.; GRAHAM, S.A. The Influence of Mass-Transport-Deposit Surface Topography on the Evolution of Turbidite Architecture: The Sierra Contreras, Tres Pasos Formation (Cretaceous), Southern Chile. **J. Sediment. Res.** 79, 287–301, 2009. https://doi.org/10.2110/jsr.2009.035

BERALDIN, S. Estratigrafia do Grupo Itararé na região de Balsa Nova (PR) e definição de critérios para sua distinção da Formação Furnas. Dissertação de Mestrado, Universidade Federal do Paraná, Brasil, 72p, 2014.

BERTON, F.; VESELY, F.F. Stratigraphic evolution of Eocene clinoforms from northern Santos Basin, offshore Brazil: Evaluating controlling factors on shelf-margin growth and deep-water sedimentation. **Mar. Pet. Geol.** 78, 356–372, 2016. https://doi.org/10.1016/j.marpetgeo.2016.09.007

BRADLEY, D.; HANSON, L. Paleoslope Analysis of Slump Folds in the Devonian Flysch of Maine. **The Journal of Geology** 106, 305–318, 1998. https://doi.org/10.1086/516024

BRIGGS, S.E.; DAVIES, R.J.; CARTWRIGHT, J.A.; MORGAN, R. Multiple detachment levels and their control on fold styles in the compressional domain of the deepwater

west Niger Delta. **Basin Research** 18, 435–450, 2006. https://doi.org/10.1111/j.1365-2117.2006.00300.x

BROOKS, H.L.; HODGSON, D.M.; BRUNT, R.L.; PEAKALL, J.; FLINT, S.S. Exhumed lateral margins and increasing flow confinement of a submarine landslide complex. **Sedimentology** 65, 1067–1096, 2018. https://doi.org/10.1111/sed.12415

BRYN, P.; BERG, K.; FORSBERG, C.F.; SOLHEIM, A.; KVALSTAD, T.J. Explaining the Storegga Slide. **Marine and Petroleum Geology** 22, 11–19, 2005. https://doi.org/10.1016/j.marpetgeo.2004.12.003

BULL, S.; CARTWRIGHT, J.; HUUSE, M. A review of kinematic indicators from mass-transport complexes using 3D seismic data. **Marine and Petroleum Geology** 26, 1132–1151, 2009. https://doi.org/10.1016/j.marpetgeo.2008.09.011

CAETANO-CHANG, M.R. Análise ambiental e estratigráfica do Subgrupo Itararé (PC) no sudoeste do Estado de São Paulo. São Paulo. Instituto de Geosciências da USP IG-USP (Tese de Doutorado), 310 p, 1984.

CALLOT, P.; SEMPERE, T.; ODONNE, F.; ROBERT, E. Giant submarine collapse of a carbonate platform at the Turonian–Coniacian transition: the Ayabacas Formation, southern Peru. **Basin Research** 20, 333–357, 2008. https://doi.org/10.1111/j.1365-2117.2008.00358.x

CANUTO, J.R. Origem dos diamictitos e de rochas associadas do Subgrupo Itararé no sul do Estado do Paraná e norte de Santa Catarina. Dissertação de mestrado. Intituto de Geociências-USP, 1985.

CARDOZO, N.; ALLMENDINGER, R.W. Spherical projections with OSXStereonet. **Computers & Geosciences** 51, 193-205, 2013.

CARNEIRO, C.D.R.; COSTA, F.G.D. Estruturas atectônicas da Bacia do Paraná em Campinas (SP): deformação sin-sedimentar no Subgrupo Itararé. **Terrae Didática** 2(1): p. 34-43, 2006.

CARVALHO, A.H.; VESELY, F.F. Facies relationships recorded in a Late Paleozoic fluvio-deltaic system (Paraná Basin, Brazil): Insights into the timing and triggers of subaqueous sediment gravity flows. **Sedimentary Geology** 352, 45–62, 2017. https://doi.org/10.1016/j.sedgeo.2016.12.004

CASTRO, J.C. A evolução dos sistemas glacial, marinho e deltáico das formações Rio do Sul e Rio Bonito/Mb. Triunfo (Eopermiano), sudeste da Bacia do Paraná. Tese de Doutorado - Instituto de Geociências e Ciências Exatas da Universidade Estadual Paulista, 1991.

COLLINSON, J. Sedimentary deformational structures. In: Maltman A. (Ed.), The Geological Deformation of Sediments. Chapman & Hall, London, 95-125p, 1994.

CPRM - Serviço Geológico do Brasil. Folha Curitiba (SG.22). Carta Geológica do Brasil ao Milionésimo. Escala 1:1.000.000, 2004.

DAEMON, R.F.; QUADROS, L.P. Bioestratigrafia do Neopaleozóico da Bacia do Paraná. In: Sociedade Brasileira de Geologia, 24º Congresso Brasileiro de Geologia, Brasília, Anais..., 359-412p, 1970.

D'AVILA, R.S.F. Sequências Deposicionais do Grupo Itararé (Carbonífero e Eopermiano), Bacia do Paraná, na Área de Dr. Pedrinho e Cercanias, Santa Catarina, Brasil. Porto Alegre. PhD. Thesis, Universidade do Vale do Rio dos Sinos –

UNISINOS, 192p, 2009.

DALLA VALLE, G.; GAMBERI, F.; FOGLINI, F.; TRINCARDI, F. The Gondola Slide: A mass transport complex controlled by margin topography (South-Western Adriatic Margin, Mediterranean Sea). **Marine Geology** 366, 97–113, 2015. https://doi.org/10.1016/j.margeo.2015.05.001

DASGUPTA, P. Sediment gravity flow-the conceptual problems. **Earth-Science Rev**. 62, 265–281, 2003. https://doi.org/10.1016/S0012-8252(02)00160-5

DAVIS, G.H.; REYNOLDS, S.J. Structural Geology of Rocks and Regions, second ed. John Wiley and Sons, New York, 776 p, 1996.

DEBACKER, T.N.; DUMON, M.; MATTHYS, A. Interpreting fold and fault geometries from within the lateral to oblique parts of slumps: A case study from the Anglo-Brabant Deformation Belt (Belgium). **Journal of Structural Geology** 31, 1525–1539, 2009. https://doi.org/10.1016/j.jsg.2009.09.002

DEBACKER, T.N.; SINTUBIN, M.; VERNIERS, J. Large-scale slumping deduced from structural and sedimentary features in the Lower Palaeozoic Anglo-Brabant fold belt, Belgium. **Journal of the Geological Society of London** 158, 341–352, 2001. https://doi.org/10.1144/jgs.158.2.341

DE BLASIO, F. V.; ELVERHØI, A. Properties of Mass-Transport Deposits as Inferred From Dynamic Modeling of Subaqueous Mass Wasting: A Short Review. Mass-Transport Depos. Deep. Settings, 499–508, 2011. https://doi.org/10.2110/sepmsp.096.499

DEVILLE, E.; GUERLAIS, S.; CALLEC, Y.; GRIBOULARD, R.; HUYGHE, P.; LALLEMANT, S.; MASCLE, A.; NOBLE, M.; SCHMITZ, J. Liquefied vs stratified sediment mobilization processes : Insight from the South of the Barbados accretionary prism. **Tectonophysics** 428, 33–47, 2006. https://doi.org/10.1016/j.tecto.2006.08.011

DOTT, R.H. JR. Dynamics of subaqueous gravity depositional processes. **Bulletin of the American Association of Petroleum Geologists**, 47, 104-128, 1963.

ELLIOT, C.G.; WILLIAMS, P.F. Sediment slump structures: a review of diagnostic criteria and application to an example from Newfoundland. **Journal of Structural Geology** 10, 171–182, 1988.

EYLES, C.H.; EYLES, N.; FRANCA, A.B. Glaciation and tectonics in an active intracratonic basin: the late Palaeozoic Itarare Group, Parana Basin, Brazil. **Sedimentology** 40, 1–25, 1993.

EYLES, C.H.; EYLES, N. Subaqueous mass flow origin for Lower Permian diamictites and associated facies of the Grant Group, Barbwire Terrace, Canning Basin, Western Australia. **Sedimentology** 47, 343–356, 2000. https://doi.org/10.1046/j.1365-3091.2000.00295.x

FALLGATTER, C. Confined to unconfined deep-water systems of the Paraná (Brazil) and Paganzo (Argentina) basins.Tese de Doutorado, Unisinos, 191, 2015.

FALLGATTER, C.; KNELLER, B.; PAIM, P.S.G.; MILANA, J.P. Transformation, partitioning and flow-deposit interactions during the run-out of megaflows. **Sedimentology** 64, 359, 2017. https://doi.org/10.1111/sed.12307.

FALLGATTER, C.; PAIM, P.S.G. On the origin of the Itararé Group basal nonconformity and its implications for the Late Paleozoic glaciation in the Paraná

Basin, Brazil. **Palaeogeography, Palaeoclimatology, Palaeoecology**, 2017. https://doi.org/10.1016/j.palaeo.2017.02.039

FARRELL, S.G. A dislocation model applied to slump stuctures, Ainsa Basin, south central Pyrenees. **J.Struc.Geol**. 6, 727–736, 1984.

FARRELL, S.G.; EATON, S. Slump strain in the Tertiary of Cyprus and the Spanish Pyrenees. Definition of palaeoslopes and models of soft sediment deformation. In: Jones M.F., Preston R.M.F. (Eds.), Deformation of Sediments and Sedimentary Rocks, Special Publication of the Geological Society of London, 29: 181-196, 1987.

FARRELL, S.G.; EATON, S. Foliations developed during slump deformation of Miocene marine sediments, Cyprus. **J. Struct. Geol.** 10, 567–576, 1988. https://doi.org/10.1016/0191-8141(88)90024-7

FERREIRA, F.J.F. Alinhamentos estruturais – magnéticos da região centro oriental da Bacia do Paraná e seu significado tectônico. Relatório Paulipetro, Consórcio CESP/IPT Reavaliação da Potencialidade e Prospectividade em Hidrocarbonetos, 143-166p, 1982.

FESTA, A.; DILEK, Y.; PINI, G.A.; CODEGONE, G.; OGATA, K. Mechanisms and processes of stratal disruption and mixing in the development of mélanges and broken formations: Redefining and classifying mélanges. **Tectonophysics** 568–569, 7–24, 2012. https://doi.org/10.1016/j.tecto.2012.05.021

FESTA, A.; DILEK, Y.; CODEGONE, G.; CAVAGNA, S.; PINI, G.A. Structural anatomy of the Ligurian accretionary wedge (Monferrato, NW Italy), and evolution of superposed mélanges. **Geological Society of America Bulletin**, 125 (9–10): 1580–1598, 2013.

FESTA, A.; OGATA, K.; PINI, G.A.; DILEK, Y.; ALONSO, J.L. Origin and significance of olistostromes in the evolution of orogenic belts: A global synthesis. **Gondwana Res**. 39, 180–203, 2016. https://doi.org/10.1016/j.gr.2016.08.002

FISHER, Q.J.; KNIPE, R.J. The permeability of faults within siliciclastic petroleum reservoirs of the North Sea and Norwegian Continental Shelf. **Mar. Pet. Geol.** 18, 1063–1081, 2001. https://doi.org/10.1016/S0264-8172(01)00042-3

FISHER, R. Flow transformations in sediment gravity flows. **Geology** 11, 273–274, 1983. https://doi.org/10.1130/0091-7613(1983)11

FLEUTY, M. J. The description of folds. **Proc. Geol. Assoc.**, 75, 461-492, 1964.

FOSSEN, H. Structural geology. Cambridge University Press, 2nd edition, 510p, 2016.

FRANÇA, A.B.; POTTER, P.E. Estratigrafia, ambiente deposicional e análise de reservatório do Grupo Itararé (Permocarbonífero), Bacia do Paraná (parte 1). **Boletim de Geociências da Petrobrás**, 2, 147-191, 1988.

FRANÇA, A.B.; POTTER, P.E. Stratigraphy and reservoir potential of glacial deposits of the Itararé Group (Carboniferous-Permian), Paraná Basin, Brazil. **AAPG Bulletin**, 75: 62-85, 1991.

FRANÇA, A.B.; WINTER, W.R.; ASSINE, M.L. Arenitos Lapa-Vila Velha: Um modelo de trato de sistemas subaquosos canal-lobos sob influência glacial, Grupo Itararé (C-P), Bacia do Paraná. **Revista Brasileira de Geociências**, 26(1): 43-56, 1996.

FÚLFARO, V.J.; SAAD, A.R.; SANTOS, M.V.; VIANNA, R.B. Compartimentação e evolução tectônica da Bacia do Paraná. In: Geologia da Bacia do Paraná: Reavaliação

da Potencialidade e Prospectividade em Hidrocarbonetos. São Paulo, Paulipetro, Consórcio CESP/IPT, p. 75-116, 1982.

GAMA JR., E.G.; PERINOTTO, J.A.J.; RIBEIRO, H.J.P.S.; PADULA, E.K. Contribuição ao estudo da ressedimentação no Grupo Itararé: tratos de fácies e hidrodinâmica deposicional. **Revista Brasileira de Geociências**, 22: 228-236, 1992.

GEE, M.J.R.; MASSON, D.G.; WATTS, A.B.; ALLEN, P.A. The Saharan debris flow: An insight into the mechanics of long runout submarine debris flows. **Sedimentology** 46, 317–335, 1999. https://doi.org/10.1046/j.1365-3091.1999.00215.x

GESICKI, A.L.D.; RICCOMINI, C.; BOGGIANI, P.C. Ice flow direction during the late Paleozoic glaciation in western Paraná Basin, Brazil. **Journal of South America Earth Sciences** 14, 933-939, 2002.

GOMEZ-RIVAS, E.; GRIERA, A. Strain rate influence on fracture development in experimental ductile multilayers. **Tectonophysics** 502, 351–363, 2011. https://doi.org/10.1016/j.tecto.2011.02.006

GOSCOMBE, B.D.; PASSCHIER, C.W.; HAND, M. Boudinage classification: End-member boudin types and modified boudin structures. **Journal of Structural Geology** 26, 739–763, 2004. https://doi.org/10.1016/j.jsg.2003.08.015

HAHN, F. Untermeerische gleitung bei Trenton falls (Nord-America) und ihr Verhaltnis zu ahnlinchen storungs blidern: Geologie und Palaeontologie, Abhand lungen, Abteilung A: Mineralogie, Petrographie, Stuttgart, Verlagsbuchhandlung, 36:1–41, 1913.

HANSEN, E. Strain Facies. Springer-Verlag, Berlin, 207p, 1971.

HAUGHTON, P.D.W.; BARKER, S.P.; MCCAFFREY, W.D. 'Linked' debrites in sand-rich turbidite systems – origin and significance. **Sedimentology**, 50, 459–482, 2003.

HODGSON, D.M.; BROOKS, H.L. Entrainment and abrasion of megaclasts during submarine landsliding and their impact on flow behaviour. Geological Society, London, Special Publications, 477, 2018. https://doi.org/10.1144/SP477.26

HOLDSWORTH, R.E. The stereographic analysis of facing. **Journal of Structural Geology** 10, 219–223, 1988. https://doi.org/10.1016/0191-8141(88)90119-8

HOLDSWORTH, R.E. Progressive deformation structures associated with ductile thrusts in the Moine Nappe, Sutherland, N. Scotland. **Journal of Structural Geology**, 12: 443-452, 1990.

HOLZ, M.; FRANÇA, A.B.; SOUZA, P.A.; IANNUZZI, R.; ROHN, R. A stratigraphic chart of the Late Carboniferous/Permian succession of the eastern border of the Paraná Basin, Brazil, South America. **Journal of South American Earth Sciences** 29, 381–399, 2010. https://doi.org/10.1016/j.jsames.2009.04.004

JABLONSKÁ, D.; DI CELMA, C.; KORNEVA, I.; TONDI, E.; ALSOP, I. Mass-Transport deposits within basinal carbonates from southern Italy. **Italian Journal of Geosciences** 135, 30–40, 2016. https://doi.org/10.3301/IJG.2014.51

JABLONSKÁ, D.; DI CELMA, C.N.; ALSOP, G.I.; TONDI, E. Internal architecture of mass-transport deposits in basinal carbonates: A case study from southern Italy. **Sedimentology** 65, 1246–1276, 2018. https://doi.org/10.1111/sed.12420

JENNER, K.A.; PIPER, D.J.W.; CAMPBELL, D.C.; MOSHER, D.C. Lithofacies and origin of late quaternary mass transport deposits in submarine canyons, central

Scotian Slope, Canada. **Sedimentology** 54, 19–38, 2007. https://doi.org/10.1111/j.1365-3091.2006.00819.x

JONES, O.T. The geology of the Colwyn Bay district: A study of submarine slumping during the Salopian period: **Geological Society of London Quarterly Journal**, 95: 335–382, 1939.

JONK, R. Sand-rich injectites in the context of short-lived and long-lived fluid flow. **Basin Res**. 22, 603–621, 2010. https://doi.org/10.1111/j.1365-2117.2010.00471.x

JUK, K.F.V. Reservatórios turbidíticos e depósitos de transporte em massa associados a progradações deltaicas: estudo comparativo integrando dados de subsuperfície e afloramentos. Dissertação de mestrado. Universidade Federal do Paraná, Brasil, 2016.

KNELLER, B.; DYKSTRA, M.; FAIRWEATHER, L.; MILANA, J.P. Mass-transport and slope accommodation: Implications for turbidite sandstone reservoirs. **Am. Assoc. Pet. Geol. Bull.** 100, 213–235, 2016. https://doi.org/10.1306/09011514210

KRISTENSEN, M.B.; CHILDS, C.; OLESEN, N.; KORSTGÅRD, J.A. The microstructure and internal architecture of shear bands in sand-clay sequences. **J. Struct. Geol.** 46, 129–141, 2013. https://doi.org/10.1016/j.jsg.2012.09.015

LABERG, J.S.; VORREN, T.O. The Trænadjupet Slide, offshore Norway – morphology, evacuation and triggering mechanisms. **Marine Geology** 171, 95–114, 2000.

LEINZ, V. Estudos sobre a glaciação carbonífera no sul do Brasil. Boletim DNPM/DFPM, 21: 1-47, 1937.

LESEMANN, J.E.; ALSOP, G.I.; PIOTROWSKI, J.A. Incremental subglacial meltwater sediment deposition and deformation associated with repeated ice-bed decoupling: a case study from the Island of Funen, Denmark. **Quaternary Science Reviews**, 29: 3212-3229, 2010.

LEWIS, K.B. Slumping on a continental slope inclined at 1–4°. **Sedimentology**, 16: 97–110, 1971.

LOPÉZ-GAMUNDI, O.R. Pebbly mudstones in the Cretaceous Pigeon Point Formation, western California: a study in the transitional stages from submarine slumps to cohesive debris flows. **Sed. Geol.**, 84, 37–50, 1993.

LOWE, D.R.; GUY, M. Slurry-flow deposits in the Britannia Formation (Lower Cretaceous), North Sea: a new perspective on the turbidity current and debris flow problem. **Sedimentology**, 47, 31–70, 2000.

MAACK, R.A. Geologia e geografia da região de Vila Velha (Paraná) e considerações sobre a glaciação carbonífera no Brasil. Arquivos do Museu Paranaense, 5: 1-305, 1946.

MALTMAN, A. On the term “soft-sediment deformation.” Journal of Structural Geology 6, 589–592, 1984. https://doi.org/10.1016/0191-8141(84)90069-5

MALTMAN, A. The Geological Deformation of Sediments. Chapman & Hall, London, 362 p, 1994a.

MALTMAN, A. Introduction and overview. In: Maltman, A. (Ed.), The Geological Deformation of Sediments. Chapman & Hall, London, p. 1-35, 1994b.

MALTMAN, A. Deformation structures preserved in rocks. In: Maltman, A. (Ed.), The Geological Deformation of Sediments. Chapman & Hall, London, p. 261-307, 1994c.

MALTMAN, A.J.; BOLTON, A. How sediments become mobilized. Geol. Soc. London, Spec. Publ. 216, 9–20, 2003. https://doi.org/10.1144/GSL.SP.2003.216.01.02

MARTÍN-MERINO, G.; FERNÁNDEZ, L. P.; COLMENERO, J.R.; BAHAMONDE, J.R.; Mass-transport deposits in a Variscan wedge-top foreland basin (Pisuerga area, Cantabrian Zone, NW Spain). **Marine Geology** 356, 71–87, 2014.

MARTINSEN, O.J. Styles of soft-sediment deformation on a Namurian (Carboniferous) delta slope, Western Irish Namurian Basin, Ireland. Geological Society, London, Special Publications 41, 167–177, 1989. https://doi.org/10.1144/GSL.SP.1989.041.01.13

MARTINSEN, O.J. Mass movements, In: Maltman, A., ed., The Geological Deformation of Sediments: London, Chapman & Hall, 127–165, 1994.

MARTINSEN, O.J.; LIEN, T.; WALKER, R.G.; COLLINSON, J.D. Facies and sequential organisation of a mudstone-dominated slope and basin floor succession: The Gull Island Formation, Shannon Basin, Western Ireland. **Mar. Pet. Geol.** 20, 789–807, 2003. https://doi.org/10.1016/j.marpetgeo.2002.10.001

MARTIN, H. The directions of flow of the Itararé ice sheets in the Paraná Basin, Brazil. **Boletim Paranaense de Geografia**, 10/15: 25-77, 1961.

MILANI, E.J. Evolução Tectono-estratigráfica da Bacia do Paraná e seu Relacionamento com a Geodinâmica Fanerozóica do Gondwana Sulocidental. PhD Thesis, Instituto de Geociências da Universidade Federal do Rio Grande do Sul, Porto Alegre, 255p, 1997.

MILANI, E.J. Comentários sobre a origem e evolução tectônica da Bacia do Paraná. In: Bartorelli, A., Carneiro, C.D.R., Brito Neves, B.B. (Eds) Geologia do Continente Sul-Americano: Evolução da Obra de Fernando Flávio Marques de Almeida, São Paulo, Beca, p. 265-279, 2004.

MILANI, E.J.; MELO, J.H.G. DE; SOUZA, P.A. DE; FERNANDES, L.A.; FRANÇA, A.B. Bacia do Paraná. **Boletim de Geociências Da Petrobras** 15, 265–287, 2007.

MORGENSTERN, N.R. Submarine slumping and the initiation of turbidity currents. In: Marine Geotechnique (Ed. A.F. Richards), University of Illinois Press, Champaign, IL, p. 189–220, 1967.

MOHRIG, D.; MARR, J.G. Constraining the efficiency of turbidity current generation from submarine debris flows and slides using laboratory experiments. **Mar. Pet. Geol**., 20, 883–899, 2003.

MORLEY, C.K.; GUERIN, G. Comparison of gravity-driven deformation styles. **Tectonics** 15(6), 1154–1170, 1996.

MOSCARDELLI, L.; WOOD, L.; MANN, P. Mass-transport complexes and associated processes in the offshore area of Trinidad and Venezuela. **Am. Assoc. Pet. Geol. Bull**. 90, 1059–1088, 2006. https://doi.org/10.1306/02210605052

MOTTIN, T.E.; VESELY, F.F.; DE LIMA RODRIGUES, M.C.N.; KIPPER, F.; DE SOUZA, P.A. The paths and timing of late Paleozoic ice revisited: New stratigraphic and paleo-ice flow interpretations from a glacial succession in the upper Itararé Group (Paraná Basin, Brazil). **Palaeogeography, Palaeoclimatology, Palaeoecology** 490,

488–504, 2018. https://doi.org/10.1016/j.palaeo.2017.11.031

MOURGUES, R.; LECOMTE, E.; VENDEVILLE, B.; RAILLARD, S. An experimental investigation of gravity-driven shale tectonics in progradational delta. **Tectonophysics**. 474, 643–656, 2009.

MURRAY, T. Glacial deformation. In: MALTMAN A. (Ed.), The Geological Deformation of Sediments. Chapman & Hall, London, p. 73-93, 1994.

MUTTI, E.; TINTERRI, R.; BENEVELLI, G.; DI BIASE, D.; CAVANNA, G. Deltaic, mixed and turbidite sedimentation of ancient foreland basins. In: Mutti et al. (Eds), Turbidites: Models and Problems: **Mar Petrol Geol** 20, 733–755, 2003.

MUTTI, E.; CARMINATTI, M.; MOREIRA, J.L.P.; GRASSI, A.A. Chaotic deposits: examples from the Brazilian offshore and fromoutcrop studies in the Spanish Pyrenees and Northern Apennines, Italy. A.A.P.G. Annual Meeting, April 9–12, Houston, Texas, 2006.

NARDIN, T. A review of mass movement processes, sediment and acoustic characteristics, and contrasts in slope and base-of-slope systems vs. canyon-fan-basin floor systems, 1979. https://doi.org/10.2110/pec.79.27.0061

NELSON, C.H.; ESCUTIA, C.; DAMUTH, J.E.; TWICHELL, D.C. Interplay of Mass-Transport and Turbidite-System Deposits in Different Active Tectonic and Passive Continental Margin Settings: External and Local Controlling Factors. Mass-Transport Depos. Deep. Settings 39–66, 2011. https://doi.org/10.2110/sepmsp.096.039

NEMEC, W. Aspects of Sediment Movement on Steep Delta Slopes. In: Colella, A, Prior, D.B. Coarse-Grained Deltas. Spec. Publs int. Ass. Sediment., 10, 29-73, 1990.

NOBLE, T.E.; DIXON, J.M. Structural evolution of fold-thrust structures in analog models deformed in a large geotechnical centrifuge. **Journal of Structural Geology** 33, 62-77, 2011.

ODONNE, F.; CALLOT, P.; DEBROAS, E.J.; SEMPERE, T.; HOAREAU, G.; MAILLARD, A. Soft-sediment deformation from submarine sliding: Favourable conditions and triggering mechanisms in examples from the Eocene Sobrarbe delta (Ainsa, Spanish Pyrenees) and the mid-Cretaceous Ayabacas Formation (Andes of Peru). **Sediment. Geol.** 235, 234–248, 2011. https://doi.org/10.1016/j.sedgeo.2010.09.013

OGATA, K.; MUTTI, E.; PINI, G.A.; TINTERRI, R. Mass transport-related stratal disruption within sedimentary mélanges: Examples from the northern Apennines (Italy) and south-central Pyrenees (Spain). **Tectonophysics** 568–569, 185–199, 2012a. https://doi.org/10.1016/j.tecto.2011.08.021

OGATA, K.; TINTERRI, R.; PINI, G.A.; MUTTI, E. The Specchio Unit (Northern Apennines, Italy): an ancient mass transport complex originated from near coastal areas in an intra-slope setting. In: Yamada, Y., Kawamura, K., Ikehara, K., Ogawa, Y., Urgeles, R., Mosher, D., Chaytor, J., Strasser, M., (eds) Submarine mass movements and their consequences. advances in natural and technological hazards research. Springer, Netherlands, 595–605, 2012b.

OGATA, K.; MOUNTJOY, J.J.; PINI, G.A.; FESTA, A.; TINTERRI, R. Shear zone liquefaction in mass transport deposit emplacement: A multi-scale integration of seismic reflection and outcrop data. **Marine Geology**, 356, 50-64, 2014a. http://dx.doi.org/10.1016/j.margeo.2014.05.001

OGATA, K.; PINI, G.A.; FESTA, A.; POGAC̆NIK, Z.; TUNIS, G. High-Resolution Studies of Mass Transport Deposits: Outcrop Perspective for Understanding Modern Submarine Slope Failure and Associated Natural Hazards. In: Lollino G., Manconi A., Locat J., Huang Y., Canals Artigas M. (eds) Engineering Geology for Society and Territory – Volume 4. Springer, Cham., 2014b. https://doi.org/10.1007/978-3-319-08660-6_40

OGATA, K.; POGAC̆NIK, Z.; PINI, G.A.; TUNIS, G.; FESTA, A.; CAMERLENGHI, A.; REBESCO, M. The carbonate mass transport deposits of the Paleogene Friuli Basin (Italy/Slovenia): Internal anatomy and inferred genetic processes. **Mar. Geol.** 356, 88–110, 2014c. https://doi.org/10.1016/j.margeo.2014.06.014

OGATA, K.; PINI, G.A.; FESTA, A.; POGAČNIK, Ž.; LUCENTE, C.C. Meso-Scale Kinematic Indicators in Exhumed Mass Transport Deposits: Definitions and Implications. In: Lamarche G. et al. (eds) Submarine Mass Movements and their Consequences. Advances in Natural and Technological Hazards Research, vol 41. Springer, Cham., 2016. https://doi.org/10.1007/978-3-319-20979-1_46

PASSCHIER, C.W.; TROUW, R.A. Microtectonics. Springer, Berlin, 2005.

PETERSON, G.L. Implications of two Cretaceous mass transport deposits, Sacramento Valley, California. **Journal of Sedimentary Petrology**, 35: 401–407, 1965.

PINI, G.A.; OGATA, K.; CAMERLENGHI, A.; FESTA, A.; LUCENTE, C.C.; CODEGONE, G. Sedimentary mélanges and fossil mass-transport complexes: a key for better understanding submarine mass movements? In: Yamada, Y., Kawamura, K., Ikehara, K., Ogawa, Y., Urgeles, R., Mosher, D., Chaytor, J., Strasser, M. (Eds.), Submarine Mass Movements and Their Consequences. Advances in Natural and Technological Hazards Research, Springer Netherlands, pp. 585–594, 2012.

PIPER, D.J.W., COCHONAT, P.; MORRISON, M.L. The sequence of events around the epicenter of the 1929 Grand Banks earthquake: initiation of debris flows and turbidity current inferred from sidescan sonar. **Sedimentology**, 46, 79–97, 1999.

POSAMENTIER, H.W.; MARTINSEN, O.J. The character and genesis of submarine mass-transport deposits; insights from outcrop and 3D seismic data, Mass-Transport Deposits in Deepwater Settings, 2011.

PRIOR., D.B.; COLEMAN. J.M. Disintegrating retrogressive landslides on very low-angle subaqueous slopes, Mississippi delta. **Marine Geotechnology**, 3: 37–60, 1978.

PUIGDOMENECH, C.N.; CARVALHO, B.; PAIM, P.S.G.; FACCINI, U.F. Lowstand Turbidites and delta systems of the Itararé Group in the Vidal Ramos region (SC), southern Brazil. **Rev. Bras. Geoc**., 44:529-544, 2014.

QUADROS, L.P. Acritarcos e Tasmanites no Permocarbonífero da Bacia do Paraná. Revista do Instituto Geológico, 23: 39-50, 2002.

RAMSAY, J. G. Folding and Fracturing of Rocks. New York, McGraw Hill, 568p, 1967.

RICCOMINI, C.; ALMEIDA, R.P.; TURRA, B.B.; CHAMANI, M.A.C.; FAIRCHILD, T.R.; HACHIRO, J. Reativação de falha do embasamento causa sismicidade no Permotriássico da Bacia do Paraná. In: Simpósio Nacional de Estudos Tectônicos, 10, Curitiba, 2005. Boletim de Resumos Expandidos..., p. 18-20, 2005.

ROCHA-CAMPOS, A.C. The Tubarão Group in the Brazilian portion of the Paraná Basin. In: Bigarella, J.J., Becker, R.D., Pinto, I.D. (Eds.), Problems in Brazilian Gondwana Geology. UFPR, Curitiba, p. 27-102, 1967.

ROLLER, K., TREPMANN, C.A. Stereo32 1.0.3. Institut für Geologie - Ruhr University Bochum: Bochum, DE, 2003.

ROSA, E.L.M.; VESELY, F.F.; ISBELL, J.; KIPPER, F.; FEDORCHUK, N.; SOUZA, P.A. Constraining the timing, kinematics and cyclicity of Mississippian-early Pennsylvanian glaciations in the Paraná Basin, Brazil. **Sedimentary Geology**, 384, 29-49, 2019.

ROSTIROLLA, S.P.; ASSINE, M.L.; FERNANDES, L.A.; ARTUR, P.C. Reativação de paleolineamentos durante a evolução da Bacia do Paraná – o exemplo do alto estrutural de Quatiguá. **Revista Brasileira de Geociências**, 29: 639-648, 2000.

ROSTIROLLA, S. P.; APPI,C. J.; MANCINI, F.; KRAFT, R. P.; BARTOSZECK, M. K. Fraturas controladoras da migração de fluidos nos arenitos Vila Velha, Grupo Irararé, Bacia do Paraná. **Rev. Bras. Geociências** 31, 349–356, 2002. https://doi.org/10.1590/S0102-36162010000200004

ROSTIROLLA, S.P.; MANCINI, F.; RIGOTI, A. KRAFT, R.P. Structural styles of the intracratonic reactivation of the Perimbó fault zone, Paraná basin, Brazil. **J. South Am. Earth Sci.** 16, 287–300, 2003. https://doi.org/10.1016/S0895-9811(03)00065-8

ROWEN, M.G.; PEEL, F.J.; VENDEVILLE, B.C. Gravity-driven fold-belts on passive margins. In: McClay, K.R. (Ed.), Thrust Tectonics and Hydrocarbon Systems. **AAPG Memoir**, 82, 157-182, 2004.

SALAMUNI, R.; MARQUES FILHO, P.L.; SOBANSKI, A.C. Considerações sobre turbiditos da Formação Itararé (Carbonífero Superior), Rio Negro-PR e Mafra-SC. **Boletim da Sociedade Brasileira de Geologia**, 15, 1-19, 1966.

SANFORD, R.M.; LANGE, F.W. Basin study approach to oil evaluation of Paraná miogeosincline, South Brasil. **Bulletin of American Association of Petroleum Geologists**, 44(8), 1316-1370, 1960.

SANTOS, P.R.; ROCHA-CAMPOS, A.C.; CANUTO, J.R. Patterns of Late Palaeozoic deglaciation in the Paraná Basin, Brazil. **Palaeogeography, Palaeoclimatology, Palaeoecology**, 125,165-184, 1996.

SCHEMIKO, D.C.B. Relação estratigráfica entre deltas, depósitos de transporte em massa e sistemas turbidíticos da Bacia do Paraná, Paleozóico Superior, sul do Brasil. Tese de doutorado. Departamento de Geologia, Universidade Federal do Paraná, 149p, 2018.

SCHNEIDER, R. L.; MUHLMANN, H.; TOMMASI, E.; MEDEIROS, R.A.; DAEMON, R.A.; NOGUEIRA, A.A. Revisão estratigráfica da Bacia do Paraná. In: SBG, 28 Congresso Brasileiro de Geologia, Porto Alegre, 1, 41-65, 1974.

SCHWARZ, H.U. Subaqueous slope failures; experiments and modern occurrences. Contrib. Sedimentol., 11, 116, 1982.

SHARMAN, G.R.; GRAHAM, S.A.; MASALIMOVA, L.U.; SHUMAKER, L.E.; KING, P.R. Spatial patterns of deformation and paleoslope estimation within the marginal and central portions of a basin-floor mass-transport deposit, Taranaki Basin, New Zealand. **Geosphere** 11, 266–306, 2015. https://doi.org/10.1130/GES01126.1

SMITH, J.V. Flow pattern within a Permian submarine slump recorded by oblique folds and deformed fossils, Ulladulla, south-eastern Australia. **Sedimentology**, 47: 357-366, 2000.

SOBIESIAK, M.S.; KNELLER, B.; ALSOP, G.I.; MILANA, J.P. Internal deformation and kinematic indicators within a tripartite mass transport deposit, NW Argentina. **Sedimentary Geology** 344, 364–381, 2016. https://doi.org/10.1016/j.sedgeo.2016.04.006

SOBIESIAK, M.S.; ALSOP, G.I.; KNELLER, B.; MILANA, J.P. Sub-seismic scale folding and thrusting within an exposed mass transport deposit: A case study from NW Argentina. **J. Struct. Geol.** 96, 176–191, 2017. https://doi.org/10.1016/j.jsg.2017.01.006

SOBIESIAK, M.S.; KNELLER, B.; ALSOP, G.I.; MILANA, J.P. Styles of basal interaction beneath mass transport deposits. **Mar. Pet. Geol.** 98, 2018. https://doi.org/10.1016/j.marpetgeo.2018.08.028

SOARES, P.C. Tectônica sinsedimentar cíclica na Bacia do Paraná: controles. Tese para provimento de vaga de Professor Titular, Universidade Federal do Paraná, Curitiba. 131p, 1991.

SOUZA, P.A.; LIMA, M.R.; SAAD, A.R. Palinologia dos carvões paleozóicos do Estado de São Paulo, I – o carvão de Buri. **Revista do Instituto Geológico**, 14, 5-20, 1993.

SOUZA, P.A. Late carboniferous palynostratigraphy of the itarare subgroup, northeastern Paraná Basin, Brazil. **Rev. Palaeobot. Palynol**., 138, 9-29, 2006.

STRACHAN, L. Slump initiated and controlled syndepositional sandstone remobilisation: an example from the Namuriam of County Clare, Ireland. Sedimentology 49, 25–41, 2002.

STRACHAN, L.J. Flow transformations in slumps: A case study from the Waitemata Basin, New Zealand. Sedimentology 55, 1311–1332, 2008. https://doi.org/10.1111/j.1365-3091.2007.00947.x

STRACHAN, L.J.; ALSOP, G.I. Slump folds as estimators of palaeoslope: A case study from the Fisherstreet Slump of County Clare, Ireland. **Basin Research** 18, 451–470, 2006. https://doi.org/10.1111/j.1365-2117.2006.00302.x

STEWART, S.A.; CLARK, J.A. Impact of salt on the structure of the Central North Sea hydrocarbon fairways. In: Fleet, A.J., Boldy, S.A.R. (Eds.), Petroleum Geology of Northwest Europe: Proceedings of the 5th Conference. The Geological Society, London, 179-200, 1999.

SUSS, J.F.; VESELY, F.F.; SANTA CATHARINA, A.; ASSINE, M.L.; PAIM, P.S.G. O grupo itararé (Neocarbonífero-eopermiano) entre porto amazonas (PR) e mafra (SC): Sedimentação gravitacional em contexto marinho deltaico com influência glacial. **Geociencias** 33, 701–719, 2014.

TALLING, P.J.; ASSON, D.G.M.; SUMNER, E.J. Subaqueous sediment density flows : Depositional processes and deposit types. 1937–2003, 2012. https://doi.org/10.1111/j.1365-3091.2012.01353.x

TERZAGHI, K. Stability of steep slopes on hard unweathered rock: Geotechnique, 12, 251–270, 1962.

THORNTON, S.E. Origin of Mass Flow Sedimentary Structures in Hemipelagic Basin Deposits: Santa Barbara Basin, California Borderland. **Geo-Marine Letters**, 6,15-19, 1986. https://doi.org/10.1007/BF02311691

TREAGUS, S.H.; FLETCHER, R.C. Controls of folding on different scales in multilayered rocks. **Journal of Structural Geology** 31, 1340–1349, 2009.

TRIPSANAS, E.K.; PIPER, D.J.W.; JENNER, K.A.; BRYANT, W.R. Submarine mass-transport facies: New perspectives on flow processes from cores on the eastern North American margin. **Sedimentology** 55, 97–136, 2008. https://doi.org/10.1111/j.1365-3091.2007.00894.x

TRZASKOS, B.; VESELY, F.P.; ROSTIROLLA, S.P. Eventos tectônicos recurrentes impressos no arcabouço estratigráfico do Grupo Itararé na região de Vila Velha, Estado do Paraná. **Bol. Parana. Geosci.**, 89–104, 2006.

TWISS, R.J.; MOORES, E.M. Structural Geology. University of California at Davis. 2ª edição, W. H. Freeman and Company, Nova Iorque, 736p, 2007.

VAIL, P.R.; MITCHUM, R.M.J.; TODD, R.G.; WIDMIER, J.M.; THOMPSON, I.S.; SANGREE, J.B.; BUBB, J.N.; HATLELID, W.G. Seismic stratigraphy and global changes of sea level. In: Payton C. (Ed.), Seismic Stratigraphy: Applications to Hydrocarbon Exploration. AAPG, Tulsa, 49-212p, 1977.

VALDEZ BUSO, V.; AQUINO, C.D.; PAIM, P.S.G.; DE SOUZA, P.A.; MORI, A.L.; FALLGATTER, C.; MILANA, J.P.; KNELLER, B. Late Palaeozoic glacial cycles and subcycles in western Gondwana: Correlation of surface and subsurface data of the Paraná Basin, Brazil. Palaeogeography, **Palaeoclimatology, Palaeoecology**, 2017. https://doi.org/10.1016/j.palaeo.2017.09.004

VAN DER KNAPP, W.; EIJPE, R. Some experiments on the genesis of turbidity currents. **Sedimentology**, 11, 115–124, 1968.

VAN DER PLUIJM, B.A.; MARSHAK, S. Earth Structure: An Introduction to Structural Geology and Tectonics, second ed.W.W. Norton & Company Ltd, New York, London, 656 pp, 2004.

VAN RENSBERGEN, P.; MORLEY, C.K. 3D Seismic study of a shale expulsion syncline at the base of the Champion delta , offshore Brunei and its implications for the early structural evolution of large delta systems. 17, 861–872, 2000.

Van Rensbergen, P.; Morley, C.K. The effect of pore fluid overpressure and expulsion on the style and mechanism of shale dispirism, examples from the champion and Baram deltas, offshore Brunei. In: VanRensbergen, P., Hillis, P., Maltman, R.R., Morley, C.K. (Eds.), Subsurface Sediment Mobilization. **Geological Society Special Publication,** p. 395–409, 2003.

VESELY, F.F.; ASSINE, M.L. Sequencias e tratos de sistemas deposicionais do Grupo Itararé, norte do Estado do Paraná. **Revista Brasileira de Geociências**, 34: 219-230, 2004.

VESELY, F.F.; ASSINE, M.L.; ROSTIROLLA, S.P. Deformação penecontemporânea no Grupo Itararé, Bacia do Paraná: estilos estruturais, dinâmica sedimentar e implicações paleogeográficas. In: Simpósio Nacional de Estudos Tectônicos, 10, Curitiba, Anais. Curitiba: SBG núcleo PR. (CD-ROM), 2005.

VESELY, F.F.; ASSINE, M.L. Deglaciation sequences in the Permo-Carboniferous Itararé Group, Paraná Basin, southern Brazil. **Journal of South American Earth**

Sciences 22, 156–168, 2006. https://doi.org/10.1016/j.jsames.2006.09.006

VESELY, F.F.; RODRIGUES, M.C.N.L.; DA ROSA, E.L.M.; AMATO, J.A.; TRZASKOS, B.; ISBELL, J.L.; FEDORCHUK, N.D. Recurrent emplacement of non-glacial diamictite during the late Paleozoic ice age. **Geology**, 46 (7), 615–618, 2018. https://doi.org/10.1130/G45011.1

YAMAMOTO Y., SAWYER D.E. Systematic Spatial Variations in the Fabric and Physical Properties of Mass-Transport Deposits in the Ursa Region, Northern Gulf of Mexico. In: Yamada Y. et al. (eds) Submarine Mass Movements and Their Consequences. Advances in Natural and Technological Hazards Research, vol 31. Springer, Dordrecht, 2012. https://doi.org/10.1007/978-94-007-2162-3_58

WALDRON, J.W.F.; GAGNON, J.F. Recognizing soft-sediment structures in deformed rocks of orogens. **Journal of Structural Geology** 33, 271–279, 2011. https://doi.org/10.1016/j.jsg.2010.06.015

WOODCOCK, N.H. Ludlow Series slumps and turbidites and the form of the Montgomery Trough, Powys, Wales. Proceedings of the Geologists' Association, 87, 169–182, 1976a.

WOODCOCK, N.H. Structural style in slump sheets: Ludlow Series, Powys, Wales. **Journal of the Geological Society**, London, 132, 399–415, 1976b.

WOODCOCK, N.H. Specification of fabric shapes using an eigenvalue method **Geological Society of America Bulletin**, v. 88, p. 1231-1236, 1977.

WOODCOCK, N.H. The use of slump structures as palaeoslope orientation estimators. Sedimentology 26, 83–99, 1979. https://doi.org/10.1111/j.1365-3091.1979.tb00339.x

WOODCOCK N.H.; NAYLOR M.A. Randomness testing in three-dimensional orientation data. **Journal of Structural Geology**, 5 (5), 539-548, 1983.

ZACHARIAS, A.A. 2004. Preenchimento de vales incisos por associações de fácies estuarinas, Formação Rio Bonito, nordeste do Paraná. (MSc Thesis) Universidade Estadual Paulista, Rio Claro, Brazil.

ZACHARIAS, A.A.; ASSINE, M.L. Modelo de preenchimento de vales incisos por associações de fácies estuarinas, Formação Rio Bonito no norte do Estado do Paraná. **Revista Brasileira de Geociências** 35(4), 573-583, 2005.

ZALÁN, P.V.; WOLFF, S.; CONCEIÇÃO, J.C.J.; ASTOLFI, M.A.M.; VIEIRA, I.S. Tectônica e sedimentação da Bacia do Paraná. In: SBG, Simpósio Sulbrasileiro de Geologia, 3, Curitiba, Atlas..., 1: 441-477, 1987.

ZALÁN, P.V.; WOLFF, S.; ASTOLFI, M.A.M.; VIEIRA, I.S.; CONCEIÇÃO, J.C.J.; APPI, V.T.; NETO, E.V.S.; CERQUEIRA, J.R.; MARQUES, A. The Paraná Basin, Brazil. Tulsa: **AAPG Memoir**, 51, 681-708, 1990.

APÊNDICE 1 (APPENDIX 1) – TABELA DE AVALIAÇÃO DE CONJUNTOS DE DADOS DE ESTRUTURAS

Tabela com avaliação dos conjuntos de dados de estruturas de cada localidade estudada (OL). Parâmetros analsados: número de medidas (N); strength parameter C e respectiva orientação preferencial (P.o.); e intervalo de confiança de 95% (c.i. ±; em graus). Para cada parâmetros foi dado um valor de classificação (c.v.), do qual foi obtido um valor médio de classificação (c.v.*). Para cada estrutura de cada localidade foi obtido um valor de classificação (S.D.). A partir de todos os S.D. de cada localidade foi definido um valor de classificação (O.C.), o qual foi utilizado na classificação final. Número de medidas e respectivo c.v.: N ≤ 5 = 1; 5<N≥10 = 2; 10<N≥20 = 3; 20<N≥30 = 4; 30<N≥40 = 5; N > 40 = 6. P.o. e respectivo c.v.: none = 1; weak = 2; moderate = 3; and strong = 4. Valor de classificação para o intervalo de confiança de (95%): c.i. ≤ 10 is 5; 10< c.i. ≥20 is 4; 20< c.i. ≥30 is 3; 30< c.i. ≥40 is 2; and c.i. >10 is 1.

OL	Structures											
	Type	Dataset	N	c.v.	C	P.o.	c.v.	c.i. (95%)	c.v.	c.v.*	S.D.	O.C.
1	Faults	Normal	10	2	3.87	m	3	20.8	3	3	3	3
		Reverse	4	1	n	u	0	41.3	1	1	1	
	Folds	Hinge	15	3	2.57	w	2	13.8	4	3	3	
		Axial plane	13	3	1.97	w	2	19	4	3		
		Facing	13	3	1.48	w	2	25.4	3	3		
		Ridges	8	2	7.45	s	4	4.4	5	4		
	Banded matrix		47	6	2.06	w	2	11.4	4	4	4	
	Injectite	Sills	21	4	2.93	w	2	13.7	4	3	3	
		Dikes I	26	4	1.47	w	2	17.5	4	3		
		Dikes II	15	3	2.87	w	2	17.4	4	3		
2	Folds	Hinge	7	2	1.77	w	2	26.7	3	2	2	3
		Axial plane	7	2	1.1	w	2	n	0	1		
		Facing	7	2	1.35	w	2	34.4	2	2		
	Banded matrix		18	3	1.91	w	2	17.5	4	3	3	
3	Folds	Hinge	46	6	1.8	w	2	12.3	4	4	3	4
		Axial plane	35	5	0.98	w	2	n	0	2		
		Facing	29	4	1.02	w	2	n	0	2		
	Bedding		60	6	1.24	w	2	11.7	4	4	4	

Continuação:

OL	Structures											
	Type	**Dataset**	**N**	**c.v.**	**C**	**P.o.**	**c.v.**	**c.i. (95%)**	**c.v.**	**c.v.***	**S.D.**	**O.C.**
4	Faults	Middle	22	4	2.74	w	2	11.9	4	3	3	3
		Slickenlines	12	3	1.27	w	2	26.6	3	3		
		Base	3	1	n	u	0	41	1	1	1	
	Folds	Hinge (middle)	3	1	n	u	0	22.9	3	1	1	
		Hinge (base)	6	2	7.58	s	4	4.5	5	4	3	
		Axial plane (base)	6	2	7.18	s	4	10.4	4	3		
		Facing (base)	6	2	4.44	m	3	11.1	4	3		
	Bedding	Middle	7	2	3.7	m	3	10.3	4	3	3	
		Base	25	4	2.66	w	2	8.4	5	4	4	
5	Faults	Normal	2	1	n	u	0	6.51	5	2	2	3
		Reverse	3	1	n	u	0	17.5	4	2		
	Folds	Hinge	7	2	2.8	w	2	28.8	3	2	2	
		Axial plane	7	2	1.84	w	2	32.1	2	2		
		Facing	7	2	4.81	m	3	17.3	4	3		
	Bedding		26	4	2.28	w	2	9.7	5	4	4	
6	Faults	Normal	6	2	1.27	w	2	32.1	2	2	1	2
		Reverse	1	1	n	u	0	n	0	0		
	Grooves/ Stretch marks		31	5	1.15	w	2	25	3	3	3	
8	Faults	Undefined	19	3	1.69	w	2	21.5	3	3	3	3
		Normal	23	4	1.58	w	2	20.5	3	3	3	
		Slickenlines	23	4	2.22	w	2	13.4	4	3		
	Folds	Hinge	3	1	n	u	0	22	3	1	1	
		Axial plane	3	1	n	u	0	18.2	4	2		
		Facing	3	1	n	u	0	20.4	3	1		
	Banded matrix		20	3	2.49	w	2	9.6	5	3	3	
	Injectites		50	6	2.77	w	2	6	5	4	4	
9	Faults	Reverse	4	1	n	u	0	13.7	4	2	3	3
		Undefined	8	2	3.84	m	3	10.7	4	3		
		Normal	13	3	3.56	m	3	13.8	4	3		
		Slickenlines	6	2	2.87	w	2	30.1	2	2		
10	Faults	Normal	23	4	3.91	m	3	10.5	4	4	4	3
	Bedding		31	5	2.65	w	2	9	5	4	4	
	Folds	π axis	1	1	n	u	0	n	0	0	0	
	Boudins	Normal faults	11	3	4.24	m	3	7.6	5	4	3	
		Reverse faults	5	1	5.74	m	3	4.6	5	3		
		Axis	8	2	3.18	m	3	13.7	4	3		
	Slickenlines (intrastratal)		10	2	1.36	w	2	22.6	3	2	2	
11	Folds	Hinge	9	2	3.38	m	3	20.4	3	3	3	4
		Axial plane	9	2	4.72	m	3	6.2	5	3		
		Facing	9	2	4.87	m	3	19.7	4	3		
	Bedding		18	3	3.24	m	3	7.8	5	4	4	

Continuação

OL	Structures											
	Type	**Dataset**	**N**	**c.v.**	**C**	**P.o.**	**c.v.**	**c.i. (95%)**	**c.v.**	**c.v.***	**S.D.**	**O.C.**
12	Faults	Reverse	11	3	3.41	m	3	8.8	5	4	3	2
		Undefined	28	4	3.23	m	3	5.7	5	4		
		Normal	2	1	n	u	0	3.2	5	2		
		Slickenlines	3	1	n	u	0	18	4	2		
	Folds	Hinge	2	1	n	u	0	n	0	0	0	
13	Folds	Hinge	19	3	3.12	m	3	16.3	4	3	3	3
		Axial plane	13	3	5.51	m	3	18.4	4	3		
		Facing	13	3	1.28	w	2	21.9	3	3		
	Bedding		25	4	4.25	m	3	10.3	4	4	4	
	Injectites	Sills	2	1	n	u	0	7.4	5	2	2	
		Dikes	3	1	n	u	0	9.3	5	2		
	Faults	reverse	1	1	n	u	0	n	0	0	0	
14	Faults		3	1	n	u	0	4	5	2	2	3
	Clasts oriented	intrabasinal	9	2	2.38	w	2	15.3	4	3	2	
		extrabasinal	25	4	1.72	w	2	22.3	3	3	3	
15	Faults	Reverse	13	3	3.26	m	3	16.5	4	3	3	4
	Folds	Hinge	45	6	3.48	m	3	9.4	5	5	4	
		Axial plane	43	6	1.51	w	2	13.8	4	4		
		Facing	43	6	2.37	w	2	10.3	4	4		
	Bedding		69	6	3.39	m	3	6.5	5	5	5	
16	Bedding		8	2	4.27	m	3	7	5	3	3	2
	Folds	Hinge	1	1	n	u	0	n	0	0	0	
17	Faults	Normal	14	3	1.58	w	2	18.3	4	3	2	3
		Slickenlines	1	1	n	u	0	n	0	0		
	Bedding		19	3	2.9	w	2	8.6	5	3	3	
18	Faults	Normal	9	2	5.18	m	3	6.9	5	3	3	3
	Folds	Hinge	9	2	6.03	s	4	13.5	4	3	3	
		Axial plane	9	2	4.32	m	3	14	4	3		
		Facing	9	2	6.32	s	4	3.9	5	4		
	Bedding		19	3	5.81	m	3	4	5	4	4	

APÊNDICE 2 (APPENDIX 2) – TABELA DE AVALIAÇÃO DA DIREÇÃO DE TRANSPORTE POR ESTRUTURA E DA DIREÇÃO FINAL DE TRANSPORTE

Tabela com avaliação da direção de transporte por tipo de estrutura e da direção final de transporte por localidade (OL). Parâmetros analisados: número de métodos (N.M.) e intervalo de confiança 95% (c.i. ±; em graus). O número de métodos equivale ao próprio valor de classificação e para c.i. foi dado um valor de classificação (c.v.). A partir dos parâmetros da direção de transporte por tipo de estrutura e valor de classificação dos conjuntos de dados de cada estrutura (S.D.) foi obtido um valor de classificação (c.v.*). Para cada estrutura de cada local foi obtido um valor de classificação (c.v.**) a partir de de todos os c.v.* do mesmo tipo de estrutura. A partir de todos os c.v.** de uma localidade foi obtido um valor para o local (O.C.*), que foi usada na classificação final. A partir do c.v. do número de métodos aplicado em cada localidade e c.i. (95%) da direção final de transporte um valor de classificação (O.C.**) por localidade. A classificação final (F.C.) considera a classificação das estruturas (O.C. no Apêndice 1), classificação da direção de transporte por localidade (O.C.*) e classificação da direção final de transporte (O.C.**). O valor de classificação para c.i. (95%) é o mesmo aplicado no Apêndice 1. O valor de classificação para todos os métodos aplicado em cadalocalidade (N.M.) é: c.v. = 1 for 1 método; c.v. = 2 for 2 to 3 métodos; c.v. = 3 para 4 a 6 métodos; c.v. = 4 para 7 a 10 métodos; e c.v. = 5 para mais que 10 métodos. Em casos de duas possíveis direções de transporte dependendo da interpretação de alguma estrutura usadas as letras (a) e (b) para indicar cada possível interpretação.

OL	Structures transport direction									Final transport direction					
	Type	Cluster	N.M. (c.v.)	c.i. (95%)	c.v.	S.D.	c.v.*	c.v.**	O.C.	N.M.	c.v.	c.i. (95%)	c.v.	O.C.	F.C.
1	Faults	Normal	3	24.3	3	3	3	3	3	16	5	15.9 (a); 17.1 (b)	4	5	3
		Reverse	3	35.6	2	1	2	2							
	Folds	Hinge Axial plane Facing Ridges	5	5.2	5	3	4	4							
	Banded matrix		1	11.4	4	4	3	3							
	Injectites	Sills Dikes I Dikes II	4	43.8 (a); 17.6 (b)	1(a); 4(b)	3	3(a); 4(b)	3 (a); 4(b)							

Continuação:

OL	Structures transport direction									Final transport direction					
	Type	Cluster	N.M. (c.v.)	c.i. (95%)	c.v.	S.D.	c.v.*	c.v.**	O.C.	N.M.	c.v.	c.i. (95%)	c.v.	O.C.	F.C.
2	Folds	Hinge Axial plane Facing	3	10	5	2	3	3	3	4	3	8.5	5	4	3
	Banded matrix		1	17.5	4	3	3	3							
3	Folds	Hinge Axial plane Facing	5	7.9	5	3	4	4	4	6	3	9.8	5	4	4
	Bedding		1	11.7	4	4	3	3							
4	Faults	Middle Slickenlines	5	15.9	4	3	4	4	3	14	5	10.2	4	5	3
		Base	3	5.9	5	1	3	3							
	Folds	Hinge (middle)	1	22.9	3	1	2	2							
		Hinge (base) Axial plane (base) Facing (base)	3	3.6	5	3	4	4							
	Bedding	Middle	1	10.3	4	3	3	3							
		Base	1	8.4	5	4	3	3							
5	Faults	Normal Reverse	3	6.6	5	2	4	4	3	7	4	12.9	4	4	3
	Folds	Hinge Axial plane Facing	3	8.8	5	2	3	3							
	Bedding		1	9.7	5	4	3	3							
6	Faults	Normal Reverse	3	5.1	5	1	3	3	3	4	3	4.3	5	4	3
	Grooves/Stretch marks		1	25	3	3	2	2							
8	Faults	Undefined	1	21.5	3	3	2	2	3	10	4	31 (a); 22.4 (b)	2 (a); 3 (b)	3(a); 4(b)	3
		Normal Slickenlines	4	29.3 (a); 25 (b)	3	3	3	3							
	Folds	Hinge Axial plane Facing	3	33.5	2	1	2	2							
	Banded matrix		1	9.6	5	3	3	3							
	Injectites		1	6	5	4	3	3							

Continuação:

OL	Structures transport direction									Final transport direction					
	Type	Cluster	N.M. (c.v.)	c.i. (95%)	c.v.	S.D.	c.v.*	c.v.**	O.C.	N.M.	c.v.	c.i. (95%)	c.v.	O.C.	F.C.
9	Faults	Reversal Undefined Normal Slickenlines	5	18.6	4	3	4	4	4	5	3	18.6	4	4	4
10	Faults	Normal	3	2.2	5	4	4	4	3	10	4	14.9	4	4	3
	Bedding		1	9	5	4	3	3							
	Folds	Hinge	1	n	0	0	0	0							
	Boudins	Normal faults Reverse faults Axis	4	11.3	4	3	4	4							
	Slickenlines		1	22.6	3	2	2	2							
11	Folds	Hinge Axial plane Facing	5	16.8	4	3	4	4	4	6	3	18.3	4	4	4
	Bedding		1	7.8	5	4	3	3							
12	Faults	Reverse Undefined Normal Slickenlines	5	34.7	2	3	3	3	3	6	3	28.1	3	3	3
	Folds	Hinge	1	13.5	4	0	2	2							
13	Folds	Hinge Axial plane Facing	5	11.6	4	3	4	4	3	9	4	14.9	4	4	3
	Bedding		1	10.3	4	4	3	3							
	Injectites	Sills Dikes	2	22.6	3	2	2	2							
	Faults	reverse	1	n	0	0	0	0							
14	Faults		1	4	5	2	3	3	3	3	2	20.8	3	3	3
	Clasts oriented	intrabasinal	1	15.3	4	3	3	3							
		extrabasinal	1	22.3	3	3	2	2							
15	Faults	Reversal	2	5.5	5	3	3	3	4	10	4	10.8	4	4	4
	Folds	Hinge Axial plane Facing	7	7.2	5	4	6	6							
	Bedding		1	6.5	5	5	4	4							
16	Bedding		1	7	5	3	3	3	2	2	2	7.4	5	4	2
	Folds	Hinge	1	n	0	0	0	0							
17	Faults	Normal Slickenlines	4	30.9	2	2	2	2	3	5	3	36.5	2	3	3
	Bedding		1	8.6	5	3	3	3							
18	Faults	Normal	1	6.9	5	3	3	3	3	5	3	10.4	4	4	3
	Folds	Axis Axial plane Facing	3	13.8	4	3	3	3							
	Bedding		1	4	5	4	3	3							

APÊNDICE 3 (APPENDIX 3) - RESULTADOS DA DEFINIÇÃO DE PALEOTALUDE

Tabela com direções de transporte obtido por cada método aplicado a cada estrutura, direção principal de transporte (Final transport direction) obtidos a partir dos métodos aplicados em cada localidade e respectivo interval de confiança (c.i. 95%), direção e sentido de paleofluxo de cada localidade que corresponde ao azimute do paleotalude local e que definido a partir da direção final de transporte e cinemática observada em campo e respectiva classificação final de robustez.

Outcrop locality	Structures	Dataset	Number of data	Method	Transport direction (°)	Final Transport direction (°)	c.i. (95%)	Paleoflow/ Paleoslope azimuth (°)	Final Classification
1	Faults	Normal	10	MFOM (1)	52-232	59-239 (a); 47-227 (b)	15.9 (a); 17.1 (b)	239 (a); 227 (b)	strong robustness
				MFOM (2)	103-283				
				FIM	100-280				
		Reverse	4	MFOM (1)	21-201				
				MFOM (2)	101-281				
				FIM	68-248				
	Folds	Hinge	15	DAM	60-240				
		Axial surface	13	MAPS	51-231				
				AIM	66-246				
		Facing	13	FFD	48-228				
		Ridges	8	Mean orientation	61-241				
	Banded matrix		47	MBSM	176-356				
	Injectite	Sills	21	Mean orientation	172-352				
		Dikes I	26		73-253 (a); 163-343 (b)				
					19-199 (a); 109-289 (b)				
		Dikes II	15		32-212				

Continuação:

Outcrop locality	Structures	Dataset	Number of data	Method	Transport direction (°)	Final Transport direction (°)	c.i. (95%)	Paleoflow/ Paleoslope azimuth (°)	Final Classification
2	Folds	Hinge	7	MAM	33-213	17-197	8.5	197	strong robustness
		Axial surface	7	MAPS	9-189				
		Facing	7	FFD	17-197				
	Banded matrix		18	MBSM	9-189				
3	Folds	Hinge	46	MAM	49-229	52-232	9.8	52	strong robustness
				MAD	55-235				
		Axial surface	35	MAPS	53-233				
				MAD-AP	51-231				
		Facing	29	FFD	27-207				
	Bedding		60	MBSM	74-254				
4	Faults	Middle	22	MFOM (1)	47-227	60-240	10.2	240	strong robustness
				MFOM (2)	99-279				
				FIM	82-262				
		Slickenlines middle	12	SLM (1)	48-228				
				SLM (2)	68-248				
		Base	3	MFOM	48-228				
				MFOM	34-214				
				FIM	39-218				
	Folds	Hinge (middle)	3	DAM	79-259				
		Hinge (base)	6	DAM	41-221				
		Axial surface (base)	6	MAPS	48-228				
		Facing (base)	6	FFD	40-220				
	Bedding	Middle	7	MBSM	67-247				
		Base	25	MBSM	99-279				

Continuação:

Outcrop locality	Structures	Dataset	Number of data	Method	Transport direction (°)	Final Transport direction (°)	c.i. (95%)	Paleoflow/ Paleoslope azimuth (°)	Final Classification
5	Faults	Normal	2	MFOM	101-281	119-299	12.9	299	strong robustness
		Reverse	3	MFOM	117-297				
		Normal + Reverse		FIM	107-287				
	Folds	Hinge	7	MAM	145-325				
		Axial surface	7	MAPS	144-324				
		Facing	7	FFD	126-306				
	Bedding		26	MBSM	91-271				
6	Faults	Normal	6	MFOM	24-204	30-210	4.3	210	moderate robustness
		Reverse	1	Orientation	27-207				
		Normal + Reverse		FIM	36-216				
	Grooves/ Stretch marks		31	Mean orientation	34-214				
8	Faults	I	19	MFOM	149-329	163-343 (a); 151-331 (b)	31 (a); 22.4 (b)	343 (a); 331 (b)	moderate robustness (a); strong robustness (b)
		II	23	MFOM (1)	72-252 (a); 162-342 (b)				
				MFOM (2)	10-190 (a); 100-280 (b)				
				FIM	47-227 (a); 137-317 (b)				
		Slickenlines (II)	23	SM	171-351				
	Folds	Hinge	3	MAM	33-213				
		Axial surface	3	MAPS	29-209				
		Facing	3	FFD	97-277				
	Banded matrix		20	MBSM	123-303				
	Injectites		50	Mean orientation	153-333				

Continuação:

Outcrop locality	Structures	Dataset	Number of data	Method	Transport direction (°)	Final Transport direction (°)	c.i. (95%)	Paleoflow/ Paleoslope azimuth (°)	Final Classification
9	Faults	Reversal	4	MFOM	56-236	44-224	18.6	224	strong robustness
		Undefined	8	MFOM	80-260				
		Normal	13	MFOM	13-193				
		Normal + Reverse		FIM	43-223				
		Slickenlines	6	SLM	27-207				
10	Faults	Normal	23	MFOM (1)	145-325	136-316	14.9	316	moderate robustness
				MFOM (2)	150-330				
				FIM	146-326				
	Bedding		31	MBSM	96-276				
	Folds	Hinge	1	π axis	161-341				
	Boudins	Faults normal	11	MFOM	135-315				
		Faults reverse	5	MFOM	100-280				
		Normal+Reverse		FIM	115-295				
		Axis	8	MAM	125-305				
	Slickenlines (intrastratal)		10	Mean orientation	5-185				
11	Folds	Hinge	9	SAM	178-358	15-195	18.3	15	strong robustness
				MAM	173-353				
		Axial surface	9	MAPS	50-230				
				AIM	6-186				
		Facing	9	FFD	175-355				
	Bedding		18	MBSM	50-230				
12	Faults	Reverse	11	MFOM	31-211	30-210	28.1	30	moderate robustness
		Undefined	28	MFOM	117-297				
		Normal	2	MFOM	1-181				
		Normal+Reverse		FIM	14-194				
		Slickenlines	3	SLM	15-195				
	Folds	Hinge	2	MAM	29-209				

Continuação:

Outcrop locality	Structures	Dataset	Number of data	Method	Transport direction (°)	Final Transport direction (°)	c.i. (95%)	Paleoflow/ Paleoslope azimuth (°)	Final Classification
13	Folds	Hinge	19	MAM	100-280	94-274	14.9	274	moderate robustness
				MAD	90-270				
		Axial surface	13	MAPS	61-241				
				MAD-AP	89-269				
		Facing	13	FFD	103-283				
	Bedding		25	MBSM	53-233				
	Injectites	Sills	2	Mean orientation	91-271				
		Dikes	3		127-307				
	Faults	Reverse	1	Orientation	134-314				
14	Faults		3	MFOM	130-310	107-287	20.8	287	moderate robustness
	Clasts oriented	intrabasinal	9	Mean orientation	111-291				
		extrabasinal	25		81-261				
15	Faults	Reversal	13	MFOM	83-263	94-274	10.8	274	strong robustness
				FIM	92-272				
	Folds	Hinge	45	MAM	98-278				
				MAD	105-285				
		Axial surface	43	MAPS	102-282				
				MAD-AP	108-288				
				AIM	111-291				
		Facing	43	FFD(1)	111-291				
				FFD(2)	77-257				
	Bedding		69	MBSM	45-225				

Continuação:

Outcrop locality	Structures	Dataset	Number of data	Method	Transport direction (°)	Final Transport direction (°)	c.i. (95%)	Paleoflow/ Paleoslope azimuth (°)	Final Classification
16	Bedding		8	MBSM	38-218	44-224	7.4	224	weak robustness
	Folds	Hinge	1	Orientation	50-230				
17	Faults	Normal	14	MFOM (1)	113-293	86-266	36.5	266	moderate robustness
				MFOM (2)	35-215				
				FIM	94-274				
		Slickenlines	1	SLM	44-224				
	Bedding		19	MBSM	145-325				
18	Faults	Normal	9	MFOM	31-211	23-203	10.4	203	moderate robustness
	Folds	Hinge	9	MAM	7-187				
		Axial surface	9	MAPS	7-187				
		Facing	9	FFD	36-216				
	Bedding		19	MBSM	35-215				